University of Strathclyde
Department of Mechanical & Aerospace Engineering

Computational study of gas transport in shale at pore-scale and beyond

Lefki Germanou

A thesis presented in fulfilment of the requirements for the degree of
Doctor of Philoshopy

2019

Declaration of Authenticity and Author's Rights

This thesis is the result of the author's original research. It has been composed by the author and has not been previously submitted for examination which has led to the award of a degree.

Lefki Germanou
October 2019

Abstract

Unconventional gas resources like shale are poised to enter a golden age thanks to the worldwide increased exploitation potential. Yet, the future of these resources is far from assured since it is still subject to many uncertainties, mainly with regard to gas recoverability. The macroscopic flow properties that allow the prediction of production are directly linked to the microscopic flow where underlying rarefaction effects play a major role. This is due to the pore size which is as small as a few nanometers and comparable to the mean free path. Thus, an in-depth understanding of gas transport in ultra-tight porous media is crucial for the accurate determination of flow properties in shale rocks. This thesis is a fundamental research aiming to aid and benefit shale gas exploration and development.

The objective of this work is to provide useful insights for such non-equilibrium porous media flows, where the conventional fluid mechanics theory fails. Even though there are multiple heuristic permeability models in the literature, I find them unsuitable to provide reliable apparent permeability estimates since they often include simplifications of the flow mechanisms and matrix complexity. Notably, I hereby establish/prove the limitations of the accuracy of the Navier-Stokes equations to the first order of Knudsen number. We also thoroughly analyse Klinkenberg's slip factor behaviour for a wide range of gas rarefaction, utilising gas kinetic theory, for both simple and complex porous media.

Moreover, using controllably random porous media, I systematically quantify the impact of numerous structural characteristics, i.e. porosity, tortuosity, specific surface area, heterogeneity and degree of anisotropy, on both intrinsic and apparent permeability. One of the key contributions of this work is a new semi-analytical permeability formulation derived using the produced simulation results. This expression, suitable for both isotropic and anisotropic two-dimensional porous media, accounts for the aforementioned properties as well as for continuum and slip flow. The main advantage of the proposed formulation is the fact that it does not entail any experimental or numerical data as input, unlike other established models.

Shale is intrinsically multiscale, thus the direct simulation of transport in all scales

is not feasible. Upscaling from the pore-scale is indispensable in order to eventually obtain the essential macroscopic properties in the field-scale. For this reason, I examine well-known analytical and numerical upscaling techniques, verifying the sensitivity and accuracy of the latter ones. Studying microscale sample images, we need to consider the appearance of microfractures. The difference of the characteristic length scales between the nanopores and the microfractures requires a hybrid upscaling method such as the Brinkman approach. The suitability of this model is extensively validated on fractured porous media of interest, especially on the grounds that the exact form of the effective viscosity is still a matter of discussion. We perform this validation comparing numerous direct simulation results with the corresponding ones from the Brinkman solution. Different values of the effective viscosity are investigated, along with a variable permeability model applied at the vicinity of the fluid-porous interface. Due to lack of an appropriate universal treatment of the transition zone of random porous media, we consider effective viscosity equal to fluid viscosity.

The accuracy of the Brinkman approach is further examined using several two and three-dimensional random porous media containing fractures, as well as considering rarefied conditions. Although I find that heterogeneity and anisotropy increase the error of the effective permeability derived from the Brinkman approach, generally, the effective permeability extracted from this coarse-scale model compares favourably to its fine-scale counterpart obtained from the Stokes and Boltzmann model equations for porous media flows. Finally, I conclude that neglecting the rarefaction effects leads to a significant underestimation of the effective permeability of fractured ultra-tight porous media.

Acknowledgements

I would like to take this opportunity to express my sincere gratitude to my supervisors, Dr Lei Wu and Prof Yonghao Zhang, for their expert guidance and continuous encouragement throughout my PhD studies. They have always been supportive and have given me the freedom to pursue various projects without objection.

I would like to address a warm thank you to Dr Minh Tuan Ho for always making me feel welcome and for sharing his knowledge. I am more than grateful for the many useful and enlightening discussions, his help, motivation and advice over the course of the past three years.

Thank you to all my colleagues at the James Weir Fluids Lab for providing a friendly work environment. The office has always felt a place where I could be myself and ask for help when needed. To my friends in Glasgow, you really made my life in the city pleasant and memorable and I am thankful to you all.

Thank you Konstantine for being there for me during the good and the bad times, for all of your patience, care and support. Your guidance helped me overcome many difficulties that came along the way. I value your companionship and advice more than you know.

Last but not the least, I would like to thank my family from the bottom of my heart for spiritually supporting me throughout this journey and life in general. My parents and sister have always provided unconditional love and care and I am eternally grateful to them.

Contribution to the literature

1. L. Wu, M. T. Ho, L. Germanou, X.-J. Gu, C. Liu, K. Xu, and Y. Zhang, "On the apparent permeability of porous media in rarefied gas flows," *Journal of Fluid Mechanics*, vol. 822, pp. 398-417, 2017.

2. L. Germanou, M. T. Ho, Y. Zhang, and L. Wu, "Intrinsic and apparent gas permeability of heterogeneous and anisotropic ultra-tight porous media," *Journal of Natural Gas Science and Engineering*, vol. 60, pp. 271–283, 2018.

3. L. Germanou, M. T. Ho, Y. Zhang, and L. Wu, "Shale gas permeability upscaling from the pore-scale," *Transport in Porous Media*, Under Review, 2019.

Contents

List of Figures

List of Tables

Nomenclature

Acronyms

BC	boundary condition
BGK	Bhatnagar–Gross–Krook
CCL	connected component labelling
CFD	computational fluid dynamics
DSMC	direct simulation Monte Carlo
DVM	discrete velocity method
ES-BGK	ellipsoidal-statistical BGK
FIB	focused ion beam
FSM	fast spectral method
FVBC	first-order velocity slip boundary condition
HIM	helium ion microscope
LBM	lattice Boltzmann method
MD	molecular dynamics
NSEs	Navier-Stokes equations
PNM	pore network model
QSGS	quartet structure generation set
REV	representative elementary volume
SEM	scanning electron microscope
SIMPLE	semi-implicit method for pressure linked equations
TMAC	tangential momentum accommodation coefficient

Greek symbols

ϵ	porosity
η	relative error
λ	mean free path, m
μ	dynamic viscosity, $\mathrm{kg\,m^{-1}s^{-1}}$
ρ	density, $\mathrm{kg\,m^{-3}}$
σ	tangential momentum accommodation coefficient
τ	tortuosity
ϱ	perturbed number density
ξ	viscous velocity slip coefficient

Roman symbols

$\mathbf{u}$	bulk velocity, $\mathrm{m\,s^{-1}}$
$\mathbf{v}$	molecular velocity
$\mathcal{C}$	Boltzmann collision operator
$\mathcal{T}$	perturbed temperature
A_f	anisotropy factor
AR	aspect ratio
b	slip factor
b'	equivalent slip factor
c_d	core distribution probability
D	directional growth probability
d	diameter, m
f	velocity distribution function
f_c	correction factor
G_p	dimensionless mass flow rate
H	fracture aperture
h	perturbed velocity distribution function
k	permeability, $\mathrm{m^2}$

Kn	Knudsen number
Kn^*	effective Knudsen number
Kn^f	Knudsen number at the fracture
L	reference length, m
L^*	characteristic flow length, m
m	molecular mass, kg
P	volume fraction
p	pressure, Pa
R	specific gas constant, $\mathrm{m^2 s^{-2} K^{-1}}$
r	radius (often also characteristic flow length), m
Re	Reynolds number
S	specific surface area, $\mathrm{m^{-1}}$
T	temperature, K
t	time, s
V	volume, $\mathrm{m^3}$
V_f	volume of fluid cells, $\mathrm{m^3}$
v_m	most probable molecular speed, $\mathrm{m\,s^{-1}}$
2D	two-dimensional
3D	three-dimensional

Subscripts

∞	intrinsic
0	reference
a	apparent
an	anisotropic
c	cylinder
D	Darcy
diag	diagonal
eff	effective

eq	equilibrium
f	final
is	isotropic
main	main
max	maximum
mean	mean
n	normal
ref	reference
s	slip
tr	transition zone

Superscripts

$2D$	two-dimensional
$3D$	three-dimensional
A	arithmetic mean
C	coarse-scale
F	fine-scale
G	geometric mean
H	harmonic mean

"They did not know it was impossible so they did it"
Mark Twain

Chapter 1

Introduction

This *chapter* serves as an introduction for this thesis. The motivation behind this work related to shale gas is analysed in Section 1.1. Some important information regarding shale gas production estimates and extraction process is given in Section 1.2. Later, in Section 1.3, key characteristics of shale gas flows are mentioned and some well-known permeability estimation models are discussed. The multi-scale nature of shale requires the use of upscaling for the calculation of the effective properties macroscopically, as analysed in Section 1.4. The shale rock contains multiple fractures which facilitate the flow of gas and make the production through this ultra-tight porous medium feasible. The problem of momentum transport between a porous medium and a pure fluid region, such as a fracture, is presented in Section 1.5. Then, in Section 1.6 the objectives of this research are briefly outlined and finally in Section 1.7, an overview of the rest of this thesis is given.

1.1 Motivation

Shale gas has attracted significant global interest due to its successful production in the United States, favoured by the recent development of economic extraction technologies, i.e. hydraulic fracturing. However, the "shale gas revolution" is not equally advanced in other regions of the world, where geological conditions might be more complex and hence, the extraction cost is high. Therefore, to make global exploitation of shale gas reserves feasible and thus meet world's demand in natural gas, accurate monitoring, prediction and optimisation of the production is indispensable. Typically, this is achieved through reservoir-scale fluid flow simulations in the order of kilometres, requiring input parameters, such as porosity and permeability, which are properties

that characterise the rock formation. Porosity is defined as the ratio of volume of pores to the total volume of the rock, while permeability, in this context, is a measure of the ability of a porous medium to allow fluid to flow through it.

Shale is considered a fine-grained sedimentary rock of ultra-low permeability (in the order of nanoDarcies [1, 2, 3, 4]) owing to its nano-pores [5]. Macroscopic behaviour is thus directly linked to the internal micro-structure, which in the case of shale is quite complex and presents heterogeneous features [6]. Under these circumstances, understanding the multi-scale transport of shale gas requires firstly the thorough examination of the reservoir's micro-structure. This is not a trivial task due to the fact that the conventional fluid dynamics theory fails to capture the rarefaction effects involved in ultra-tight porous media gas flow. In shale gas flow, the molecules collide more frequently with the pore surface in comparison with the collisions among themselves, influencing gas transport in the porous media. Further complexities are added to the gas flow simulation due to the presence of organic matter (kerogen) which instigates other flow processes.

My motivation to investigate shale gas flows stems from the insufficient understanding we have on the momentum transport processes and from the fact that, according to my judgement, permeability is often erroneously calculated using oversimplifications of the geometry and/or the flow mechanisms. To this end, a plethora of numerical studies has been performed in this work in order to get useful insights for shale gas flows in the pore-scale and beyond.

1.2 Background

Unconventional gas estimates represent 40% of the total recoverable resources of natural gas; however this percentage is filled with uncertainty [5]. Recent publications, as reviewed in [5], indicate that shale gas is in abundance in North America, which is by far the best studied region. The regions that follow, with significant estimates, are Europe and China where the exploitation is still in its infancy. Estimates predict that the incremental share of unconventional gas production will rise to 21% in 2020 and to 32% in 2035 since more countries are expected to achieve commercial production in time [8].

Hydrocarbon extraction from mudrocks (alternative name for shale) requires hydraulic fracturing technology to be applied to achieve commercial production (see Fig. 1.1). Wells are drilled vertically from the surface until the depth of the deposits is reached. Then, the wellbore is extended horizontally within the shale formations and hydraulic fracturing takes place. Shale gas becomes accessible only after the following

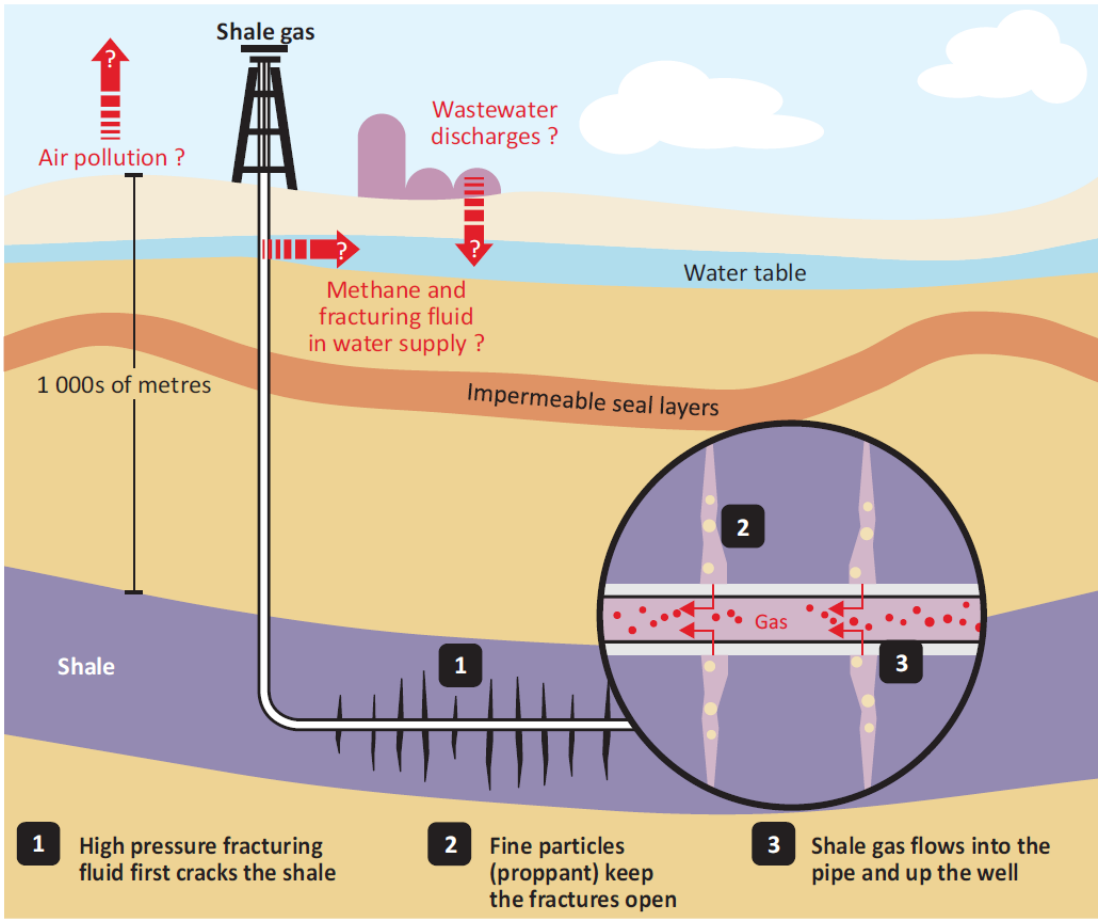

Figure 1.1: Schematic of the shale gas extraction process. Adapted from [7].

elaborate process is performed. The rock matrix is fractured with pressurised fracking fluid and the induced fractures or fissures are kept open by the injection of sand and chemicals which act as proppants. The overall permeability of the rock is then boosted since gas can flow rapidly through the highly permeable fractures. Finally, the well pressure is decreased so that shale gas can flow from the rock to the wellbore driven by the pressure difference [9].

1.3 Shale gas flows and heuristic permeability models

1.3.1 Gas transport in shale

Recent development of imaging techniques provides 2D and 3D high resolution images where the nano-structure of the shale strata is revealed. For instance, Focused Ion Beam (FIB)/Scanning Electron Microscope (SEM) imaging can provide digital images

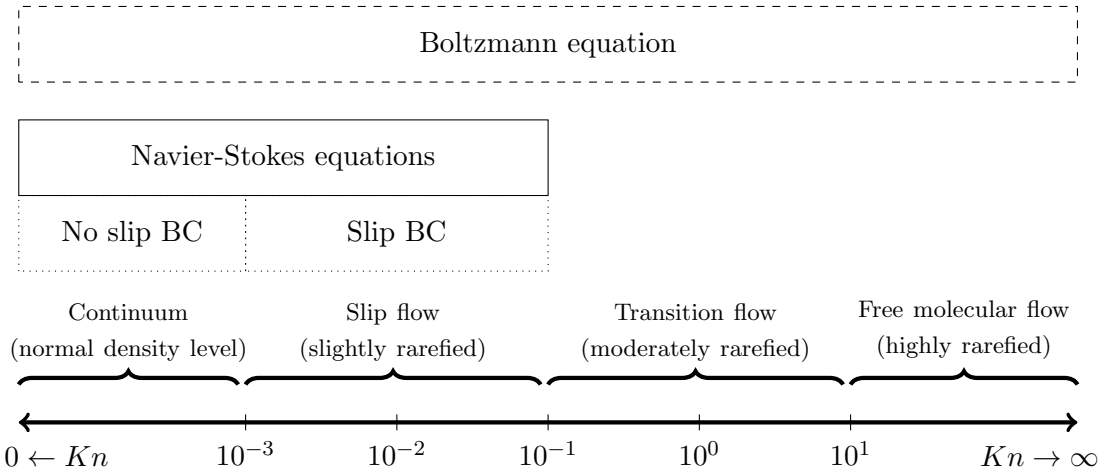

Figure 1.2: Flow regimes with respect to Knudsen number based on experiments on straight pipe flows. BC stands for boundary condition.

with a resolution as high as 6.5nm whereas the state-of-the-art Helium Ion Microscope (HIM) can even approach 0.5nm resolution [13]. Numerical simulation can be directly applied on the above imaging models to uncover the gas transport mechanisms. The reader is referred to Fig. 1 of [13] for the resolutions and sample dimensions of the available imaging methods.

However, this is not a trivial task since the computational fluid dynamics (CFD) based on continuum approach fail in the area of non-equilibrium gas dynamics. The primary reason is that the molecular nature of the gas can no longer be ignored when its mean free path becomes comparable to the characteristic length of the flow. For example, it is proven that the Navier-Stokes equations (NSEs) under-predict the gas flow rate through carbon nanotubes by several orders of magnitude [14]. At the micro/nano-scale, collisions between gas molecules are too infrequent to fully thermodynamically equilibrate gas, causing velocity slip and temperature jump at solid surfaces, and Knudsen layer of non-linear stress/strain-rate behaviour [15, 16].

The Knudsen number, Kn, is a main indicator of the degree of thermodynamic equilibrium of a flow and thus it is the characteristic parameter for gas flow in micro/nano-scale porous media. It is usually defined as the ratio of the mean free path of gas molecules λ (an average distance travelled by molecules between collisions [17]) to the characteristic flow length L:

$$Kn = \frac{\lambda}{L}, \text{ and } \lambda = \frac{\mu(T_0)}{\bar{p}}\sqrt{\frac{\pi R T_0}{2}}, \tag{1.1}$$

where $\mu(T_0)$ is the shear viscosity of the gas at a reference temperature T_0, $\bar{p}$ is the

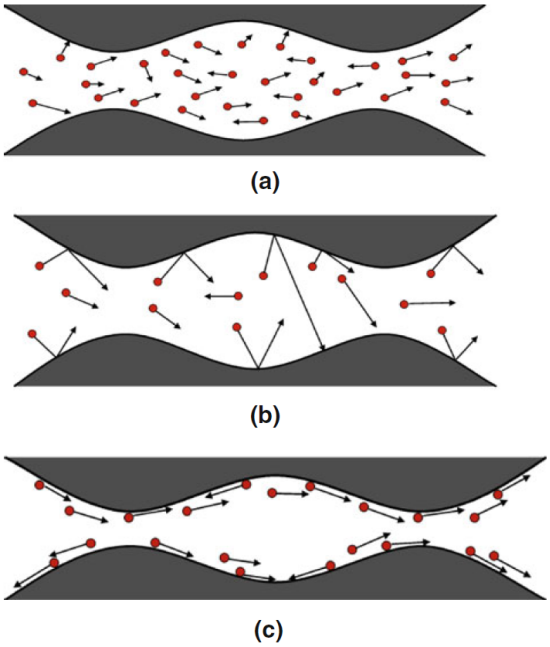

Figure 1.3: Schematic of pore cross-sections illustrating diffusion processes occurring during shale gas flow. The movement of the gas molecules corresponds to (a) viscous flow (b) Knudsen diffusion (c) surface diffusion. The above mechanisms often also coexist under certain circumstances. Adapted from Fig. 1 in [10].

mean gas pressure, and R is the specific gas constant [18, 19, 20, 21].

Based on Kn, gas flows can be classified into four regimes (see Fig. 1.2) [22]:

- continuum (or Darcy) flow regime: for ($Kn \leq 0.001$) the continuum hypothesis is applicable, hence the Navier-Stokes equations are valid; the viscous flow dominates [23]
- slip flow regime: for ($0.001 < Kn \leq 0.1$) the slippage phenomenon appears at the walls and the Navier-Stokes equations are still applicable when coupled with appropriate velocity-slip boundary conditions [12, 24]; gas transport is dominated by both viscous and slip flow
- transition flow regime: for ($0.1 < Kn \leq 10$) the continuum assumption breaks down and gas kinetic equations are used instead [12, 19]; both slip and Knudsen diffusion phenomena are encountered while viscous flow is reduced
- free molecular flow regime: for ($Kn > 10$) there is minimal interaction between the gas molecules; Knudsen diffusion is predominant

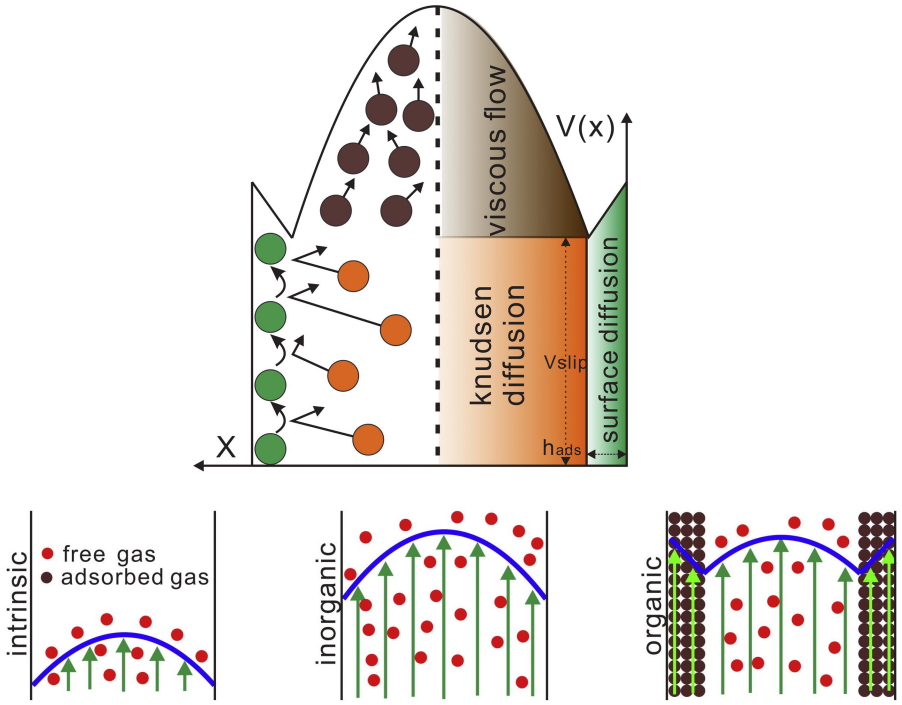

Figure 1.4: (Top) Schematic of the pore velocity profile contributions from different transport mechanisms. (Bottom) Schematics of the velocity profiles considering: (left) only the rock properties, i.e. intrinsic, (middle) rarefaction effects (inorganic pores) and (right) rarefaction effects and surface diffusion (organic pores). I remark that the first two cases are studied in this work. Adapted from Figs. 7 and 7 in [11] and [12] respectively.

It is important to keep in mind that the limits of Kn for each regime may change according to the problem geometry, as emphasised in [24].

For methane and carbon dioxide in an unconventional reservoir, with pressures up to several hundred bars, the gas flow through nano-pores is in the slip and transition regimes [25, 26]. Due to the high pressures, the fluid is closer to its liquid state and rarefaction effects are related to high confinement.

A few flow transport mechanisms, which often coexist, occur during shale gas transport. Explanatory schematics are given in Figs. 1.3 and 1.4, while for velocity profiles produced by molecular dynamics (MD) simulations the reader is referred to [27] (see Fig. 3). For macroscale pores the viscous flow dominates the gas transport where the intermolecular interactions prevail. For smaller pores, non-Darcy effects start to appear. The velocity of the gas molecules near the pore surface cannot be neglected, leading to gas slippage. When the flow characteristic length (pore size) is comparable to or smaller than the mean free path of gas molecules, the intermolecular collisions

are much less frequent than the collisions between gas molecules and the solid walls, leading to Knudsen diffusion. In other words, it is as if the gas molecules move independently from one another. The authors of [28, 29] claim that the contribution of Knudsen diffusion to the total mass flux is significant in mudrock systems.

I herein remark on some additional processes and effects that I do not include in my study. Adsorption/desorption is a transport process common in organic-rich shales, often ignored by several researchers. In pores with small diameters, a large number of gas molecules are absorbed on the organic wall surface creating thus an adsorption layer. When the flow starts (due to pressure difference) then the process of surface diffusion occurs, meaning that absorbed methane migrates along the pore surface driven by the density gradient between the bulk region and the adsorption layer [30]. In [12, 26] the authors claim that the effect of adsorption is mainly for pores with $r < 2$nm, producing additional contributions to the mass flow. On the other hand, the authors of [28] state that surface diffusion is negligible in reservoir conditions. Surface diffusion becomes important when the adsorbed layer size is appreciable, which can be achieved only if the temperature is not significantly greater that the gas boiling point [30]. The researchers claimed that this is not the case for shale reservoirs, thus they ignore adsorption effects. Moreover, [9] reported that in their analysis, using data from Barnett Shale wells, desorption effect was found to be negligible. For further information regarding adsorption and the surface diffusion process the reader is referred to the following works [10, 12, 30, 31]. The effect of adsorption in the mass flux is shown in Fig. 1.4.

Generally, as pointed out by [26, 29, 32], at equilibrium there is the free gas that occupies the pores, the adsorbed gas that covers the organic pore surfaces and the dissolved gas within the organic materials (kerogen). Most of the gas is stored in the organic matter of the shale matrix, which is embedded within the inorganic substance [27]. The processes of drilling a well or even fracturing disturbs the equilibrium, firstly resulting to the flow of the free gas towards the low pressure zone. Later, the methane molecules concentrated near the surface of the organic material desorb, increasing pore pressure. This process changes the concentration equilibrium between the bulk of the kerogen and its surface, initiating gas diffusion towards the surface.

I highlight that in this work, adsorption phenomena are not accounted for, thus I consider all pores to be inorganic (lying between inorganic minerals [33]). Furthermore, linearised assume that the gas is ideal and that is all stored in the pore spaces, ignoring gas diffusion in the permeable organic materials. Finally, linearised consider the single-phase flow to be chemically inert, isothermal and incompressible with $Re < 1$ (Reynolds number is the ratio between the inertial forces and the viscous forces).

Overall, in response to lower well pressure, gas flows in the fractures, with the flow being initially (at the early stages of production) in the continuum regime. Then, after the pressure is further decreased flow enters the slip, transition or even Knudsen flow regimes, depending on the pore size and gas state [27].

1.3.2 Heuristic permeability models

A direct consequence of gas rarefaction is that the measured permeability is larger than the intrinsic (Darcy) permeability, often symbolised as k_∞ or simply k, and rises as the mean gas pressure decreases as found experimentally by Klinkenberg [34]. Due to this, Darcy's law is no longer suitable to describe gas transport in shale. The Darcy equation yields

$$\bar{u}_D = -\frac{k_\infty}{\mu}\frac{\mathrm{d}p}{\mathrm{d}x}, \tag{1.2}$$

where $\bar{u}_D$ is the Darcy velocity (the volume averaged velocity at the bulk of the porous medium) and μ is fluid viscosity. The validity of this equation is extensively proven for low-Re porous media flows, however, it is not capable of describing flow transport in ultra-tight porous media like shale in its initial form. To circumvent this, the so-called apparent gas permeability, k_a, is introduced which is compatible with the Darcy equation. The intrinsic permeability depends on the void space and solid surface characteristics, while the apparent gas permeability additionally takes into account gas pressure, type and more generally the flow conditions [35]. Therefore, k_∞ is obtained for $Kn = 0$. The apparent permeability is introduced by Klinkenberg as follows [34]:

$$k_a = k_\infty \left(1 + \frac{b}{\bar{p}}\right) = k_\infty f_c, \tag{1.3}$$

where b is the slip factor which is usually considered not to be a constant [21]. Generally, researchers also refer to the correction factor of permeability, f_c, which is often mentioned here as permeability enhancement.

The calibration of the slip factor for tight porous media has been the subject of several studies. Numerous first-order correlations can be found in [10]. A list of some well-known permeability models to be analysed, and their main characteristics is given in Table 1.1. In the simple case of an idealised porous medium composed of uniform tubes of radius r the permeability expression takes the following form according to Klinkenberg [34]

$$k_a = k_\infty \left(1 + \frac{4c\lambda}{r}\right) = k_\infty \left(1 + 4cKn\right), \tag{1.4}$$

where the coefficient c is often taken as unity. This expression is derived by coupling

Table 1.1: Comparison of established apparent permeability models for ultra-tight porous media.

Model	Description
Klinkenberg (1941) Eq. (1.4)	empirical slip flow model
Javadpour (2009) Eq. (1.15)	accounts for slip flow (derived based on Maxwell model) and Knudsen diffusion, modelled for straight capillaries
BKC (2010) Eq. (1.7)	accounts for slip flow, simplified second-order slip model with several empirical parameters
Darabi et al. (2012) Eq. (1.17)	accounts for slip flow (derived based on Maxwell model) Knudsen diffusion and surface roughness requires experimental estimation of parameters

Maxwell's first-order slip boundary condition for velocity [36] with the Navier-Stokes equations [18, 37, 38]. The intrinsic permeability for a straight tube is

$$k_\infty = \frac{r^2}{8}. \tag{1.5}$$

Nevertheless, Klinkenberg's linear (first-order) correction of permeability is not sufficient, especially as the effective Knudsen number, i.e. the ratio of the mean free path to the average pore size, Kn^*, increases. The generalised form of a second-order correction in terms of Kn is given by [20] as

$$k_a = k_\infty \left(1 + \frac{A}{\bar{p}} + \frac{B}{\bar{p}^2}\right) \tag{1.6}$$

where A and B are unknown fitting parameters. Trying to capture the non-linear relationship between intrinsic and apparent gas permeability, Beskok & Karniadakis [24] developed the following unified BK model, i.e. an empirical second-order correction in terms of Kn for flow in a single pipe/tube/channel, valid across the whole range of rarefaction.

$$k_a = k_\infty(1 + \alpha(Kn)Kn)\left(1 + \frac{4Kn}{1 - bKn}\right), \tag{1.7}$$

where the constant b denotes a slip coefficient and the dimensionless rarefaction coefficient α is provided by the following expression

$$\alpha(Kn) = \alpha_0 \frac{2}{\pi} \tan^{-1}\left(\alpha_1 Kn^{\alpha_2}\right), \tag{1.8}$$

where $\alpha_1 = 4$ and $\alpha_2 = 0.4$. Also a_0 is given by

$$\alpha_0 \equiv \alpha_{Kn\to\infty} = \frac{64}{3\pi\left(1 - \frac{4}{b}\right)}. \tag{1.9}$$

For slip flow, the reported values are $\alpha = 0$ and $b = -1$ and thus $\alpha_0 = \frac{64}{15\pi}$. The authors validated this model against numerical results produced using the DSMC (direct simulation Monte Carlo) method, linearised Boltzmann solutions, and experimental data. The BK correlation was later simplified by Civan [18] which claims to correct the approach of [38] for tight porous media as

$$k_a = k_\infty(1 + \alpha(Kn^*)Kn^*)\left(1 + \frac{4Kn^*}{1 + Kn^*}\right), \tag{1.10}$$

where the dimensionless rarefaction coefficient α is provided by the following empirical expression

$$\alpha(Kn) = \frac{1.358}{1 + 0.170Kn^{*-0.4348}}. \tag{1.11}$$

This simplified second-order correlation which accounts for slip flow is here referred to as the Beskok–Karniadakis–Civan (BKC) model. The effective Knudsen number, Kn^* is, in fact, an average local Knudsen number of the system defined using the characteristic length of the flow L^*, or most commonly the average pore size r, as

$$Kn^* = \frac{\lambda}{L^*}. \tag{1.12}$$

In this model, the average pore size is determined using

$$L^*_{BKC} = \sqrt{\frac{8\tau k_\infty}{\epsilon}} \tag{1.13}$$

where ϵ is the porosity of the porous medium and τ is the hydraulic tortuosity of the preferential flow paths describing the average elongation of the fluid streamlines as compared to free flow.

Numerous other studies have been devoted to the derivation of analytical formulations to describe the apparent permeability of porous media, most of them either based on the straight tube (or bundle of capillary tubes) simplification [29, 39] or using the NSEs beyond their validity leading to questionable results [40]. Particularly, Javadpour [29] proposed a now well-known model considering two major flow mechanisms, slip flow and Knudsen diffusion, for a single straight nanotube. The derived apparent

permeability reads

$$k_a = \frac{2r\mu}{3RT\rho}\left(\frac{8RT}{\pi}\right)^{0.5} + \frac{r^2}{8}\left(1 + (8\pi RT)^{0.5}\,\frac{\mu}{r\bar{p}}\left(\frac{2-\sigma}{\sigma}\right)\right), \tag{1.14}$$

where σ is the tangential momentum accommodation coefficient (TMAC). TMAC represents the portion of the molecules that are reflected diffusely; $\sigma = 1$ corresponds to fully diffuse reflection, while $\sigma = 0$ corresponds to purely specular reflection [29, 32, 41, 42]. The value of TMAC ($0 \leq \sigma \leq 1$) varies depending on surface morphology, gas properties, temperature and pressure. It is usually determined using experimental measurements [43, 44] or MD simulations [45] for specific systems. Utilising the ideal gas law $\bar{p} = \rho RT$ and Eqs. (1.1) and (1.5) Javadpour's formula can be reformulated as follows

$$k_a = k_\infty\left(1 + \left(\frac{2-\sigma}{\sigma}\right)4Kn + \frac{64}{3\pi}Kn\right). \tag{1.15}$$

Another modelling approach uses the fractal dimension and tortuosity to account for the roughness of pore surfaces and sinuous flow paths respectively, building upon previous simpler models [28, 46]. Specifically, Darabi et al. [28] derived a permeability model that accounts for some of the complexities involved in gas flows through ultra-tight porous media, namely, slip flow, Knudsen diffusion and surface roughness. The model is derived adding a proportionality factor to the first term of Javadpour's expression (1.14) as follows

$$k_a = \frac{\epsilon}{\tau}(\delta')^{D_f-2}\frac{2r\mu}{3RT\rho}\left(\frac{8RT}{\pi}\right)^{0.5} + \frac{r^2}{8}\left(1 + (8\pi RT)^{0.5}\,\frac{\mu}{r_{mean}\bar{p}}\left(\frac{2-\sigma}{\sigma}\right)\right), \tag{1.16}$$

where δ' is the ratio of the molecular radius to average pore radius and D_f is the fractal dimension of the pore surface. Similarly, this expression can be also written as

$$k_a = k_\infty\left(1 + \left(\frac{2-\sigma}{\sigma}\right)4Kn^* + \frac{\epsilon}{\tau}(\delta')^{D_f-2}\frac{64}{3\pi}Kn^*\right). \tag{1.17}$$

The effective characteristic length used for the transformation in terms of Kn^* is derived using Eq. (1.5), i.e.

$$L_t^* = \sqrt{8k_\infty}, \tag{1.18}$$

which is mentioned in [28] to provide the average pore radius, r_{mean} for their model.The above two models of Javadpour (1.15) and Darabi et al. (1.17) are herein reformulated with respect to Knudsen number, in order to highlight the linear correction in terms of Kn, similar to Klinkenberg's formulation (1.4) but with the addition of an extra linear

term (third term), leading to a greater proportionality factor.

Note that the main parameters of the model proposed by Darabi et al. are determined by laboratory measurements, including the well-known pulse-decay experiment [47]. Generally, the above heuristic models estimate some of their parameters, such as slip coefficients, Darcy permeability, tortuosity, and fractal dimension of surface, through experiments or using other existing simplified correlations. Consequently, the literature provides a large amount of apparent gas permeability models which focus on the transport phenomena neglecting the full extend of rock matrix complexity. The several assumptions and empirical parameters they entail, requiring calibration according to the porous media properties, usually make them suitable only for idealised media and slip flows.

On the other hand, it is well-documented by several researchers that pore size and geometry have a notable effect on the proportion of diffusion in total flow rate [29, 31, 48]. Additionally, many models incorporating the simplification of the porous medium as a bundle of straight cylindrical tubes are proven to produce contradictory results compared to experimental observations of ultra-tight porous media. For instance, in [49] the authors used first and second-order slip models (the former being Klinkenberg's (1.4) and the latter being the Beskok & Karniadakis model (1.7)), to fit their experimental measurements of shale permeability. The fitting provided the slip coefficients of both models and TMAC. The use of the models in the slip region is in good agreement with the experimental data, however both models overestimate the permeability enhancement in the transition regime. It should be noted that the Maxwell first-order slip boundary condition is valid for small Knudsen number flows (typically $Kn < 0.1$) while the BK model is validated for channel, pipe and duct flows for the entire flow regime. Thus, the inadequacy of these models to capture apparent permeability in high Kn, is an indication that it is inappropriate to extend the use of simplified models beyond their Kn range of validity and in complex porous media like shale.

In other studies [37, 50], the Kozeny-Carman (KC) relationship [51, 52] is used to calculate the intrinsic permeability of the porous medium, while the BKC correlation (Eqs. (1.10) and (1.11)) is used to calculate apparent permeability of shale assuming that the pores are a bundle of tortuous capillary tubes with uniform pore size. Following the work of [10], the characteristic pore radius of the porous medium used for the calculation of the effective Knudsen number, is approximated with the expression proposed by [53]

$$L^* = \sqrt{\frac{8k_\infty}{\epsilon}}. \tag{1.19}$$

Hence, in many studies, oversimplified permeability models are misused for shale permeability estimation, neglecting important matrix properties that play a significant role in the overall production performance. Furthermore, it is also common for most of the existing permeability models to include several empirical parameters, which make their use impractical and introduce more uncertainties. Since the existing formulations cannot predict accurately shale gas apparent permeability, linearised believe that rarefied flow in complex porous media requires thorough investigation of the pore-scale.

1.4 Multi-scale nature of the shale rock

Shale formations are characterised by heterogeneity across multiple scales (nanometre to kilometre), which makes the accurate determination of their effective properties, in particular permeability, a challenging task. In the presence of this structural heterogeneity permeability depends on scale [54]. It is advisable thus to define different scales in an appropriate hierarchical manner to facilitate permeability estimation.

In such extremely tight porous media with low permeability, it is sensible to start their study from the pore-scale, where the transport phenomena are better understood, and afterwards upscale the obtained macroscopic quantities using a Darcy-like model. Considering domains larger than the nano-scale means eventually including fine and discrete fractures in the simulations, which significantly increase permeability.

Even in the case of laboratory measurements, the determined gas-transport properties represent only the intact rock matrix, therefore, these properties are required to be scaled-up using field tests to provide useful information and describe the whole reservoir [47]. However, since nanoscale experiments are associated with many difficulties, e.g. limited precision, irreversibility of the process, extreme time requirements, the numerical approach is often preferred [13, 55].

1.4.1 Pore-scale modelling

The current high-resolution images provide a pore space which connects across the sample, making the direct numerical simulation feasible. An example of such simulations performed on shale sample, which has porosity $\epsilon = 0.17$ and size $L = 4.6\mu$m can be found in [56]. The utilised 3D pore-structure model, shown in Fig. 1.5, is reconstructed from 200 slices of 2D SEM images which were converted into a binary model (solid and fluid) by [57].

As an alternative to the direct simulation on the shale samples, many researchers utilise the pore-network model (PNM) approach, generally used to model porous media flow. Through this approach, the porous medium is approximated using pore bodies

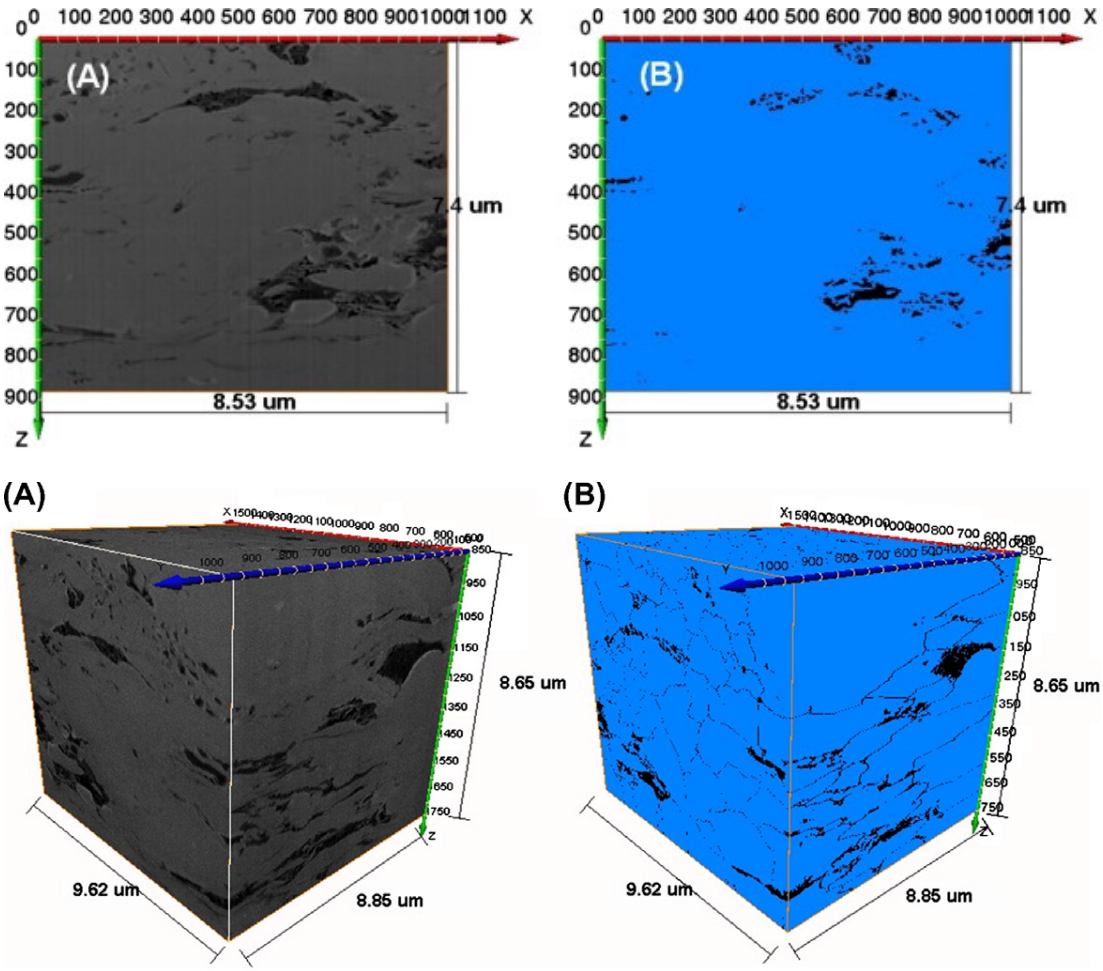

Figure 1.5: (Top) 2D shale model: (a) SEM/FIB image in grayscale (b) the converted binary image where pores are indicated with black and matrix with blue. (Bottom) 3D shale model: (a) pore-structure model in grayscale reconstructed from 200 SEM/FIB images (b) the converted binary model where pores are indicated with black and matrix with blue. Adapted from Figs. 8 and 10 in [57].

(nodes) and pore throats (bonds/connections) with different sizes, which are connected to each other appropriately. Thus, a simplified representation of both the geometry and topology of the permeable material is created. An indicative example can be found in the work of Ma et al. [32] where a pore network is extracted from a shale sample with size $L = 2.4\mu$m, which is reconstructed using numerous high resolution 2D SEM images (see Fig. 1.6).

Pore-network simulations are extensively used in the field, since they are much less computationally demanding compared to the direct methods. However, a main disadvantage inherent to PNM, is the simplification of the real pore space which could

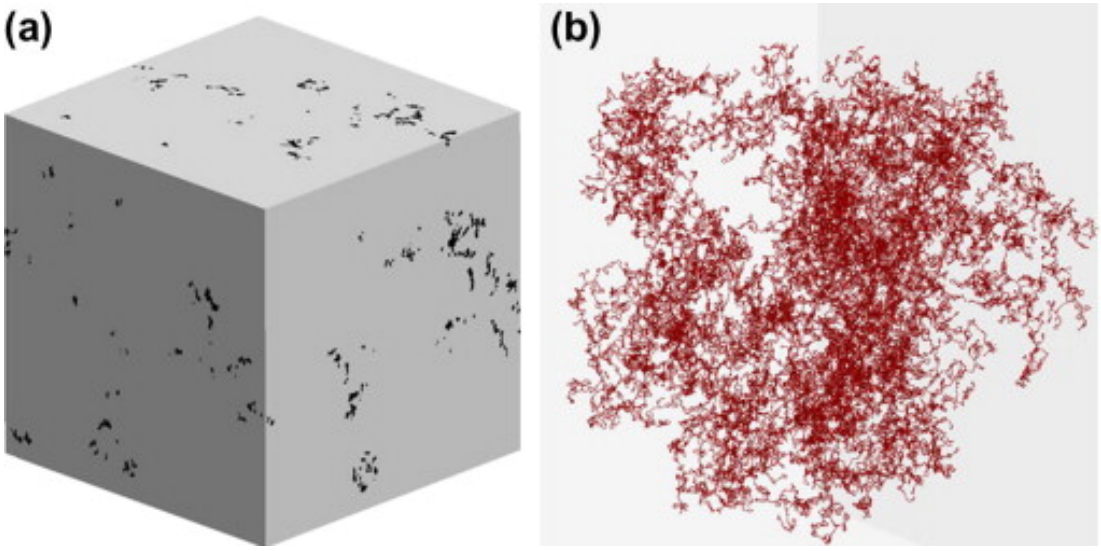

Figure 1.6: (a) The reconstructed 3D shale model, generated using several 2D SEM images and (b) the extracted pore network. Adapted from Fig. 5 in [32].

affect the credibility of the calculated transport properties. The accuracy is highly depending on the pore-network extraction process and on the transport equations that govern the nodes and bonds [32, 58, 59]. Therefore, in my work, since the accuracy of the results is crucial in gaining a better understanding of the transport processes in shale, I chose to proceed with direct methods instead.

The high-resolution sample size (L) is limited to a few microns. Moving to larger samples and lower resolutions ($L > 100\mu m$) the connectivity of the pores is not detectable while microfractures are visible [33]. This is due to the fact that the characteristic length scales of the pores and the fractures differ by orders of magnitude. Therefore, upscaling is the key to communicating data between different scales since direct numerical simulation is no longer possible.

1.4.2 Upscaling from the pore-scale

The multi-scale nature of shale rock and of the imaging techniques imposes the necessity of employing upscaling strategies for the calculation of permeability. An established hybrid model that allows the solution of the flow in a computational domain containing both porous and free flow regions is the so-called Brinkman approach [60]. When only porous regions are considered, upscaling can be performed numerically employing Darcy's law. Note that traditionally in reservoir engineering the fractures are modelled using surface elements, whereas in the selected model the fractures are discretised using control volumes where the flow is governed by the NSEs [58, 61, 62, 63].

Shale pores are usually categorised based on their size into three types [64]:

- micropores (< 2nm),
- mesopores ($2 - 50$nm),
- macropores (> 50nm).

Predominantly, the majority of the pores measured are micro- and mesopores and the average pore size is less than 20nm [13, 28, 33]. Microfracture apertures are mainly between 30μm and 1mm for shale, while sandstones contain microfractures of sizes down to 1μm [65, 66]. This suggests that the ratio of the microfracture aperture H to the mean pore size L^*, referred to as H/L^*, most of the times ranges from 150 to 5×10^5. It is widely known that shale matrix is characterised by low-speed rarefied gas flow, mainly in the slip and transition regimes [25, 26]. Given that the microfractures are at least two orders of magnitude greater than the average pore size, their flow is always governed by the Navier-Stokes equations (with or without slippage). Thus, the use of the Brinkman model for upscaling domains containing both matrix and microfractures (taking into account multiple length scales) is in theory suitable [67]. However, its level of accuracy needs to be verified.

To the best of my knowledge, a detailed study comparing the fine-scale effective permeability of ultra-tight porous media with fractures against permeability estimation derived through the Brinkman model (coarse-scale) has not been performed yet. Most of the works published so far assume a priori that the use of this approach is associated with little or no error. In a recent publication [68], the authors upscaled permeability from the pore-scale using multi-scale imaging data. The Brinkman equations were applied to predict the mesoscale permeability of two samples, which was compared to the corresponding experimental values. The numerical results were considered to be in good agreement with the measurements even though the discrepancy between the two values is deemed high. Other researchers [2, 58] use the Brinkman approach to resolve the flow for shale images that include some voxels with pores that lie below the instrument resolution. The focus of their research is on the impact of this sub-resolution porosity on permeability. The Brinkman framework has also been extensively used in other publications such as [69, 70].

The authors of [37, 50, 71] utilised the so-called "generalised Navier–Stokes equations" proposed by [72], which include non-linear and fluid inertial terms unlike the simpler Brinkman model. However, in effect, due to the low Reynolds flows they study, both the quadratic (Forchheimer) [73] and the convection terms are negligible. In their work, the apparent permeability value required as input for the model is provided by

the BKC expression, while the intrinsic permeability is obtained using the KC relationship. Specifically, a rather interesting study is performed in [37] where the flow in a porous medium with treelike fractures is examined. The permeable organic matter and the less permeable inorganic matter are represented through their respective permeabilities, while the fractures are considered "open". Simulations are carried out for various pressures (thus Knudsen numbers) indicating not only that the fractures are the preferred pathways, but also the qualitative change of the velocity distribution depending on the level of rarefaction. Even though the accuracy of these results is herein doubted due to the use of empirical permeability models, this study illustrates the potential of the Brinkman framework. This potential is also showcased in the study of [74] where the model under consideration is a fracture with obstacles (proppant grains). In that case, the Brinkman and the Stokes equations produced largely similar results.

Overall, in my view the aforementioned publications could not be considered indicative of the effectiveness of the Brinkman equation in permeability upscaling for shale. For this reason, linearised further investigate this issue in detail in the forthcoming chapters.

1.5 Momentum transfer between porous and plain media

The problem of momentum transport along the boundary between a fluid layer and a porous medium has been extensively studied over the past decades. The motivation behind this lies in the variety of applications where this configuration can be found, such as ground water pollution, catalytic and nuclear reactors, oil and gas recovery, filtration processes and thermal insulation among many others.

Beavers & Joseph [75] conducted experiments of a two-dimensional Poiseuille flow (effectively one-dimensional) through a rectangular channel bounded by an impermeable upper wall and a permeable lower wall. Their experimental and analytical work was focused on the boundary condition at the fluid-porous interface. From a microscopic point of view, the Navier-Stokes equations are satisfied in the so-called free region

$$\nabla \cdot \mathbf{u} = 0, \tag{1.20a}$$

$$\rho \left(\mathbf{u} \cdot \nabla \right) \mathbf{u} - \mu \nabla^2 \mathbf{u} = -\nabla p, \tag{1.20b}$$

where $\mathbf{u} = (u_x, u_y, u_z)$ is the flow velocity, ρ is density, μ is the dynamic viscosity and p is pressure. Typically, for gas flows with low Reynolds number the inertial term of the Navier-Stokes equations can be neglected, thus the momentum equation is reduced

giving the Stokes equations

$$\nabla \cdot \mathbf{u} = 0, \tag{1.21a}$$

$$\mu \nabla^2 \mathbf{u} = \nabla p. \tag{1.21b}$$

Additionally, the macroscopic fluid flow through the bulk of the porous region, herein isotropic and homogeneous, is described by Darcy's law (1.2). In that study, the two sets of governing equations are coupled using a semi-empirical slip boundary condition, named after the authors, applied at the interface (dividing surface) between the two distinct regions, which reads

$$\left.\frac{\mathrm{d}\bar{u}}{\mathrm{d}y}\right|_{y=0^-} = \frac{\beta}{\sqrt{k}} \left(\bar{u}|_{y=0} - \bar{u}_D\right), \tag{1.22}$$

where β is the slip coefficient and $\bar{u}$ is the volume averaged velocity. This type of description of the problem, coupling the two sets of equations that govern the homogeneous regions with an appropriate boundary condition, is commonly known as the two-domain approach.

The Beavers & Joseph boundary condition, Eq. (1.22), was derived to account for the fact that, according to the experimental results, the interfacial tangential (or slip) velocity $\bar{u}|_{y=0}$ is significantly greater than the Darcy velocity $\bar{u}_D$. This indicates the presence of a thin transition zone formed at the porous region just below the interface, where a gradual enhancement of the viscous shear is taking place, compared to the bulk of the permeable material. The slip coefficient β is an adjustable parameter that depends on the local structure of the transition zone and the flow properties.

The use of Eq. (1.22) that leads to a discontinuity of the velocity at the interface can be circumvented by the implementation of other formulations such as the widely spread model of Brinkman [60]. In this formulation, the continuity of both velocity and stress is ensured, coupling the momentum equations that govern the free fluid and porous regions (Stokes and Darcy respectively) [76]. This is a one-domain approach since the Brinkman expression describes the entire flow domain. A comparison of the two velocity profiles is shown in Fig. 1.7. This hybrid model can be regarded as an extension to Darcy's law which includes a macroscopic shear term that accounts for the velocity gradient present at the transition zone (also known as inter-region or boundary layer) and the free region. Namely, in the free flow region, the pressure gradient is balanced only by the fluid–fluid interactions, while deep in the porous medium, the pressure gradient is balanced only by the viscous dissipation against the solid matrix. However, in the transition zone both physical interactions coexist. The Brinkman momentum

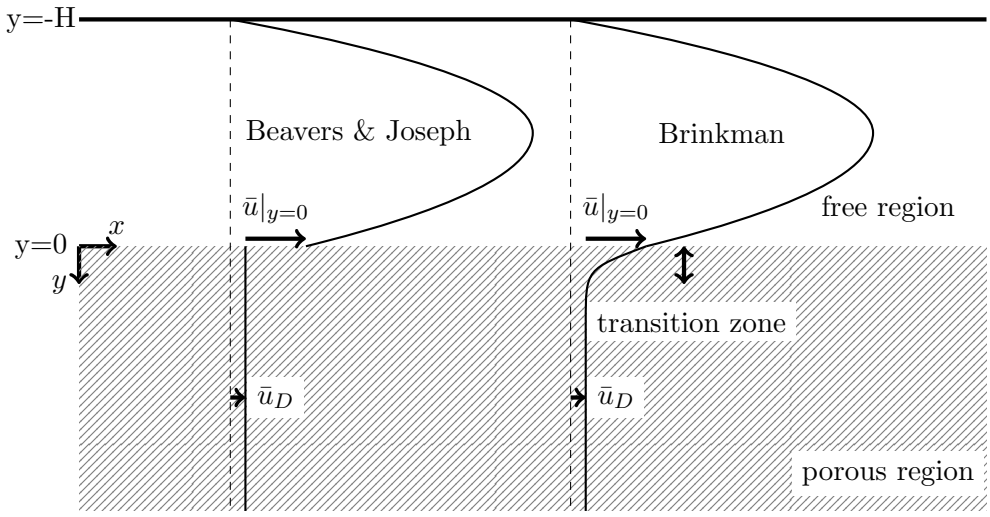

Figure 1.7: Poiseuille flow in a domain consisting of fluid region over a homogeneous and isotropic porous medium. The fluid region is bounded by an impermeable upper wall ($y = -H$) and a permeable lower wall ($y = 0$). The velocity profiles are depicted for the two-domain (left) and one-domain (right) approaches, utilising the Beavers & Joseph [75] and Brinkman [60] proposals respectively. $\bar{u}_D$ is the Darcy velocity inside the porous medium, whereas $\bar{u}|_{y=0}$ is the slip velocity at the interface between the two regions.

equation which holds for the whole domain reads

$$-\nabla p + \mu_{eff}\nabla^2\bar{\mathbf{u}} - \frac{\mu}{\mathbf{k}}\bar{\mathbf{u}} = 0, \tag{1.23}$$

where $\bar{\mathbf{u}} = (\bar{u}_x, \bar{u}_y, \bar{u}_z)$ is the vector of the volume averaged velocity, $\mathbf{k}$ is the permeability tensor and μ_{eff} is the so-called effective viscosity which is presumed constant in Brinkman's original model. The last term of the right-hand side of Eq.(1.23) is a drag term which is meaningful and dominant only if the control volume is a porous medium; otherwise, this term approaches zero ($\mathbf{k} \to \infty$). In the former case, the momentum equation can be approximated by the Darcy law (with the exception of the transition zone) while in the latter, it reduces to the Stokes equation; in that case $\bar{\mathbf{u}} = \mathbf{u}$. It should be emphasised, that if $\mu_{eff} \neq \mu$, the effective viscosity should not be considered as the real viscosity of the fluid in the porous medium. Nevertheless, in the homogeneous fluid region the flow field should be consistent with the Stokes equation, thus the original fluid viscosity, μ, must be applied there. Here linearised must remark that the assumption $\mu_{eff}/\mu = 1$ is retained in this study, unless stated otherwise, owing to lack of a definitive conclusion for this ratio from the research community.

Even though the widely known Brinkman equation has been the focus of many

researchers over the last decades, general agreement has not been reached yet regarding the definition of effective viscosity. Effective viscosity was found, to be either smaller, equal or greater than the fluid viscosity, often following heuristic approaches [77, 78]. Specifically, according to the Stokes simulations performed in [79] and their comparison with the respective Brinkman simulations, it was found that μ_{eff}/μ exceeds unity. In order for the two simulation results to match, effective viscosity should increase as the porosity of the medium decreases. Volume averaging performed by [80] resulted in $\mu_{eff} = \mu/\epsilon$. A more complex form of the effective viscosity is proposed by [81]. The authors of [82] use a periodic porous medium made of in-line or staggered arrangements of cylinders to study the flow effects at the vicinity of the free flow region. In their study, it was concluded that the effective viscosity should vary within the porous medium in order for the Brinkman model to provide satisfactory prediction of the velocity near the interface. Although this is a controversial subject, it seems to be generally accepted that effective viscosity depends on the nature of porous medium and the flow. However, the conditions of applicability of the model are also questioned in the literature [77], thus its validation for the cases of interest is essential.

The Brinkman formulation is used herein to simulate the flow in fractured porous media. The matrix is described through its effective properties (permeability tensor), therefore the explicit representation of its structure is avoided and the flow is governed by Darcy's law. Conversely, the fractures are considered "open" channels (having infinite permeability) and thus are governed by the Stokes equations. As previously mentioned, shale is known to have very low permeability, thus the inertial effects can be safely ignored.

1.6 Project objectives

In my research linearised aim at revealing the details of shale gas flows, focusing on the accurate determination of permeability in the pore-scale, and its efficient upscaling to larger scales. A comprehensive workflow is addressed using time-efficient open-source or in-house software for the required simulations across the whole spectrum of continuum to highly rarefied conditions.

As stated earlier in this *chapter*, it is common that the NSEs are used beyond their validity and that shale matrix complexity is erroneously ignored in multiple widely used permeability models. This work tries to clarify this issue, demonstrating and discussing various pore-scale rarefied flow results, obtained using gas kinetic theory. The impact of several porous media morphological properties on the intrinsic and apparent gas permeability is not yet rigorously studied. Hence, linearised aim to analyse and

correlate the behaviour of effective macroscopic properties with important structural characteristics of random ultra-tight porous media. Furthermore, proposing a new permeability formulation accounting for the structural complexity of shale is one of my main objectives.

Having deepened the understanding of pore-scale shale gas flows and obtained representative values of gas permeability, the need for appropriate upscaling of the effective properties, towards the field scale, arises. Upscaling serves as a bridge between the different scales appearing in a shale reservoir. Specifically, the demand for communication of information between the high-resolution shale images, where the pores are connected, and those of larger samples, where the low resolution leads to lack of pore connectivity, is evident. One of the vital objectives of this endeavour is to investigate effective ways to bridge the different scales appearing in such imaging data. My interest towards upscaling stems from the confidence of this research group regarding the accuracy of our pore-scale and rarefied flow simulating capabilities, as proven in recent publications [21, 56, 83, 84, 85], which lay solid foundations for the accurate approximation of macroscopic properties in shale gas flows.

To sum up, the objectives of this thesis, briefly, are as follows:

- Clarify the extend of validity of the NSEs in rarefied porous media flows;
- Quantify the impact of porous media structural complexity parameters on intrinsic and apparent gas permeability;
- Propose new permeability formulation not entailing empirical parameters;
- Investigate upscaling techniques appropriate to communicate key flow properties across scales;
- Examine permeability upscaling from the pore-scale considering microfractures.

1.7 Thesis outline

Chapter 2 presents the computational methods employed in this thesis, including the porous media geometry generation process followed by the governing equations and the numerical methods. A description of the permeability determination process and other important quantities computed in this work, is also included.

Chapter 3 discusses the limitations of the Navier-Stokes equations in describing rarefaction effects and slip factor behaviour in simplified porous media. Systematic numerical simulations are performed to investigate the accuracy of equations and expressions commonly used in rarefied porous media flows. Some further numerical examples

modifying important parameters lead to a possible explanation of the behaviour of the slip factor in Klinkenberg's famous experiments, which examine apparent permeability of ultra-tight porous media. This research has been published in the *Journal of Fluid Mechanics* under the title *"On the apparent permeability of porous media in rarefied gas flows"* [21].

A detailed parametric study investigating the effect of shale matrix complexity factors on the intrinsic and apparent permeability of ultra-tight porous media is performed in Chapter 4. Furthermore, a new permeability formulation, accounting for the effect of structural parameters and considering the continuum and slip flow regimes is proposed at the end of the *chapter*. The results and observations of this research are published in the *Journal of Natural Gas Science and Engineering* under the title *"Intrinsic and apparent gas permeability of heterogeneous and anisotropic ultra-tight porous media"* [86].

In Chapter 5, various upscaling techniques for shale gas flows are investigated. First, a comparative study between some well-known analytical upscaling methods and the numerical solution of Darcy's law is performed. The latter method is then utilised for the hierarchical upscaling of a random porous media structure with and without the inclusion of a throughout fracture. For the appropriate consideration of fractured porous media, the Brinkman approach is later implemented and investigated, focusing on the accuracy of the transition zone.

The effectiveness and suitability of the Brinkman formulation in the effective permeability calculation of fractured ultra-tight porous media is thoroughly examined in Chapter 6. Direct numerical simulations on two and three-dimensional random porous samples with fractures are performed to assess the accuracy of the Brinkman model. The 3D structures are constructed to mimic the properties of real shale samples. Finally, special focus is given to the performance of the model when rarefaction effects are considered. This work is under consideration for publication in the journal of *Transport in Porous Media*, under the title *"Shale gas permeability upscaling from the pore-scale"*.

This thesis ends with Chapter 7 where the key findings of my research are presented and relevant future work is suggested.

Chapter 2

Computational methods

This *chapter* discusses the computational methods employed in this thesis. First, in Section 2.1, the algorithm used for the generation of the porous media geometries is analysed. Furthermore, in Section 2.2, the governing equations of the flows studied and the numerical methods utilised for their solution are presented. In Section 2.3, the process followed for the calculation of the full permeability tensor of the 2D and 3D porous media studied is explained. Finally, in Section 2.4, important properties of the flows and porous media under consideration are introduced.

2.1 Geometry generation

The random $2D$ and $3D$ porous media structures used in this study are generated adopting the Quartet Structure Generation Set (QSGS) method [87]. This process reconstructs the binary matrix using three controlling parameters: the volume fraction P, the core distribution probability c_d, and the directional growth probability D_i, all within $[0, 1]$. The volume fraction is more commonly expressed as porosity ϵ, where $\epsilon = 1 - P$. The core distribution probability indicates the density of the cores from which the solid particles are formed: when the porosity is fixed, the smaller the value of c_d, the fewer the solid islands. Finally, the directional growth probability indicates the way a core cell expands and forms a solid particle in order to reach the desired volume fraction. The cell expands along the i-direction according to the value of D_i. Adjusting the ratio of D_i in all directions appropriately, controls the degree of anisotropy. The algorithm is described as follows.

1. Randomly distribute the cores in the grid based on a core distribution probability c_d, whose value is far smaller that the desired volume fraction P. Each cell is

assigned a random number based on a uniform distribution function within $[0, 1]$; the cells whose random number is no greater than c_d are selected as cores.

2. Enlarge the growing phase according to the given directional growth probability D_i. The neighbouring cells of the existing solid elements are assigned new random numbers. The neighbouring cell in i-direction will belong to the solid phase if its random number is no greater than D_i. For $2D$ structures $1 \leq i \leq 8$ (see Fig. 2.1) while for $3D$ $1 \leq i \leq 26$. The main directional growth probabilities, D_{main}, are the ones in alignment with the major axis, i.e. four and six in the two- and three-dimensional cases respectively. For simplicity, we abbreviate them as $D_1 = D_2 = D_x,\ D_3 = D_4 = D_y,\ D_9 = D_{10} = D_z$.

3. The previous step is repeated until the volume fraction reaches the desired value P.

Heterogeneity cannot be directly controlled using the initial form of the algorithm, however, [88] recently proposed a two-scale method to accomplish it which yields

1. Generate a refined structure with distinct values of core distribution probability c_d^F, directional growth probabilities D_i^F and volume fraction P^F.

2. Create a coarse structure using a new core distribution probability $c_d^C < c_d^F$ to construct the cores, and then expand them using D_i^C.

3. The coarse structure grows until the combined result of the two structures reaches the desired volume fraction P.

It is noted that heterogeneity is an increasing function of the ratio c_d^F/c_d^C. Some schematics of 2D porous media generated by the QSGS method, without explicitly imposing heterogeneity, with a $N_x \times N_y = 1000 \times 1000$ grid are shown in Fig. 2.2. In each figure, one parameter varies and the rest two are kept fixed.

Due to the random fluctuations occurring during the generation procedure, the geometries produced utilising the same set of controlling parameters do not have identical morphological features. Consequently, the calculated permeability for these geometries is not the same, but it fluctuates around a mean value. The accuracy of the generation process can be enhanced increasing the grid size or the number of particles, however the computational cost increases as well. For this reason, for the 2D geometries I select a large grid, however, for the 3D cases where the computational cost is already high, I use a small grid to balance the simulation time.

I highlight that the resulting geometries using the QSGS method often include occluded pores inside the solid impermeable particles which are not connected to the

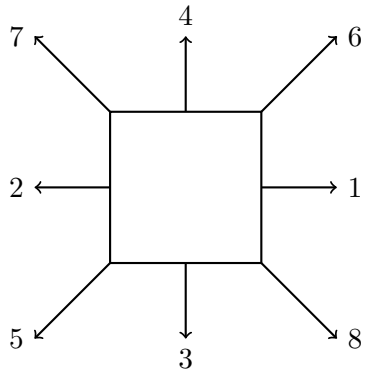

Figure 2.1: The eight (i) growth directions for 2D random porous media generation using the QSGS method.

main void space. In order to eliminate these unrealistic fluid cells a pre-processing treatment of the binary matrix was applied using the software MATLAB [89]. This treatment allows the connected pixels (in 2D) or voxels (in 3D) of binary images to be found and manipulated, following the principles of the Connected-Component Labelling (CCL) algorithm [90].

As a result, the final structure has a porosity smaller than the nominal one depending on the amount of the occluded pores. Most of the times, to compensate for these differences in the produced geometries and thus the resulting permeability values, for every set of parameters (configuration) multiple porous structures are generated and simulated. Both the mean values and the deviation of the computed quantities are taken into account.

It is worthy to stress that for the generation of the 2D QSGS structures, as in the publications of [6, 37, 50], solid is selected to be the growing phase while for the 3D structures fluid is the growing phase. This choice is based on the numerous examples of real shale sample images such as the ones in [6, 33, 88]. Even though any value of porosity can be assigned for geometry generation, the resulting structures where fluid is allowed to flow have considerably high porosities in 2D cases. This is due to the overlapping particles creating dead-end pores and obstructing the flow. For smaller particle size, this phenomenon is more pronounced. On the other hand, in 3D cases where we control pore generation, connectivity is better, permitting considerably smaller porosities closer to those of real shale samples.

Finally, I note that in the remaining part of this thesis the resolution of the produced QSGS binary matrix is mentioned in pixels for 2D images and in voxels for 3D volume-images. Hereinafter, the terms *grid* and *mesh* both refer to the corresponding computational mesh used in the numerical simulations.

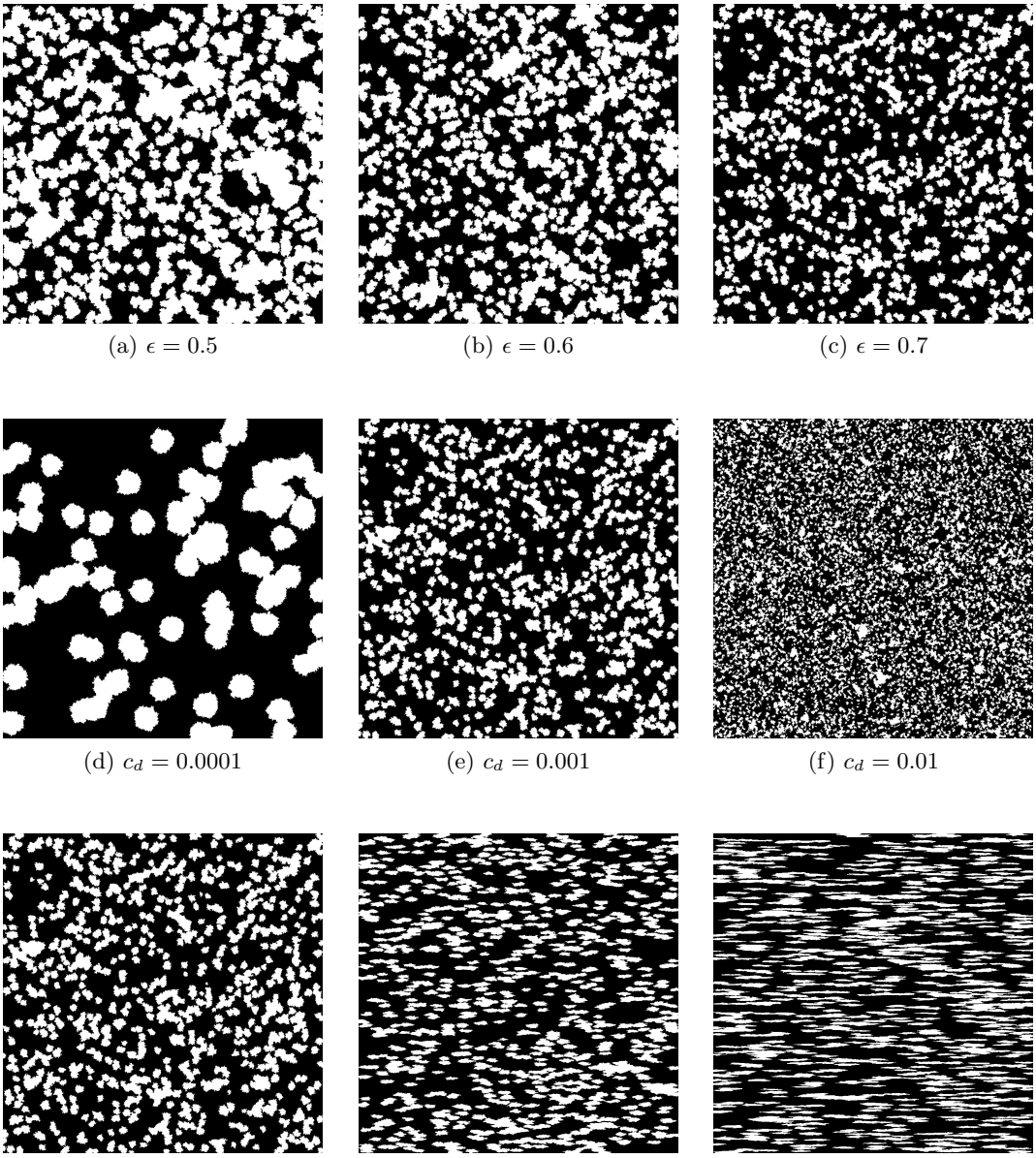

(a) $\epsilon = 0.5$ (b) $\epsilon = 0.6$ (c) $\epsilon = 0.7$

(d) $c_d = 0.0001$ (e) $c_d = 0.001$ (f) $c_d = 0.01$

(g) $D_x : D_y = 1$ (h) $D_x : D_y = 100$ (i) $D_x : D_y = 1000$

Figure 2.2: Typical geometries generated by the QSGS algorithm. White represents the solid particles while black represents the fluid region. First row: the core distribution probability is $c_d = 0.001$, the ratio of the directional growth probability is $D_x : D_y = 1$, while porosity ϵ varies. Second row: $\epsilon = 0.7$ and $D_x : D_y = 1$. Third row: $\epsilon = 0.7$ and $c_d = 0.001$.

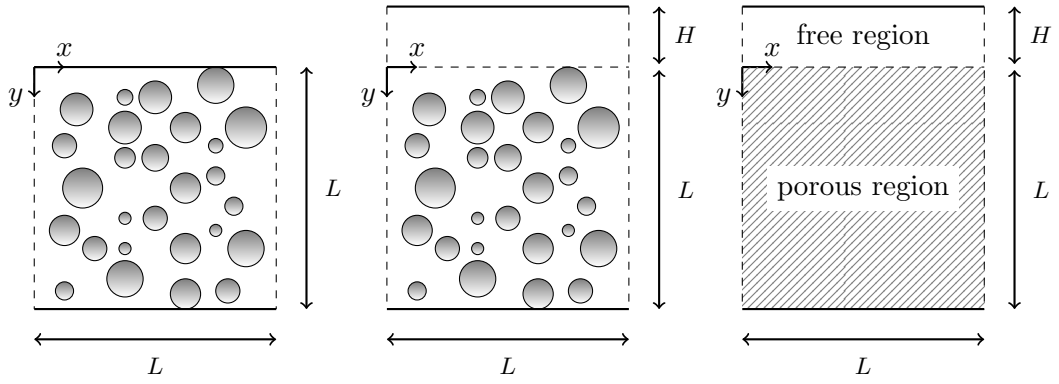

(a) Permeability determination (b) Fine-scale model (c) Coarse-scale model

Figure 2.3: Schematic representation of the computational domains involved in this study. First, the permeability tensor $\mathbf{k}$ of the porous medium is calculated in (a). Then, the fine-scale model (b) is simulated leading to the k_{eff}^{F}. It consists of the porous medium (porous region) of size L and a straight channel (free region) of thickness H as shown. The porous structure and the channel share a common interface, indicated here with a dashed line at $y = 0$. Finally, the coarse-scale model (c), where the porous medium is represented implicitly using $\mathbf{k}$, is simulated using the Brinkman equation leading to k_{eff}^{C}. Each region is usually meshed using individual blocks as explained in detail in Table 2.1.

2.2 Governing equations and numerical methods

The numerical simulations performed in this work can be distinguished in three main classes: (i) the Stokes or Boltzmann model equations are solved on the exact topology of the porous matrix in order to extract the intrinsic and/or apparent permeability tensor respectively, (ii) the Stokes or Boltzmann model equations are solved on the exact topology of the porous matrix and fracture in order to obtain the effective permeability of the fine-scale model ${k_{eff}}^{F}$, (iii) the Darcy or Brinkman equations are solved on the coarse-scale model where the porous medium is represented through its effective properties in order to acquire the effective permeability approximation ${k_{eff}}^{C}$. The two-dimensional computational domains of the above simulation categories are shown in Fig. 2.3.

2.2.1 Stokes, Brinkman and Darcy equations

The low Kn pore-scale flows of the QSGS structures and their respective macroscopic Darcy-like representations for the whole range of gas rarefaction are evaluated using the finite volume method implemented in the open-source toolbox `OpenFOAM` [91]. This software is an efficient parallel, three-dimensional code that is also capable of handling

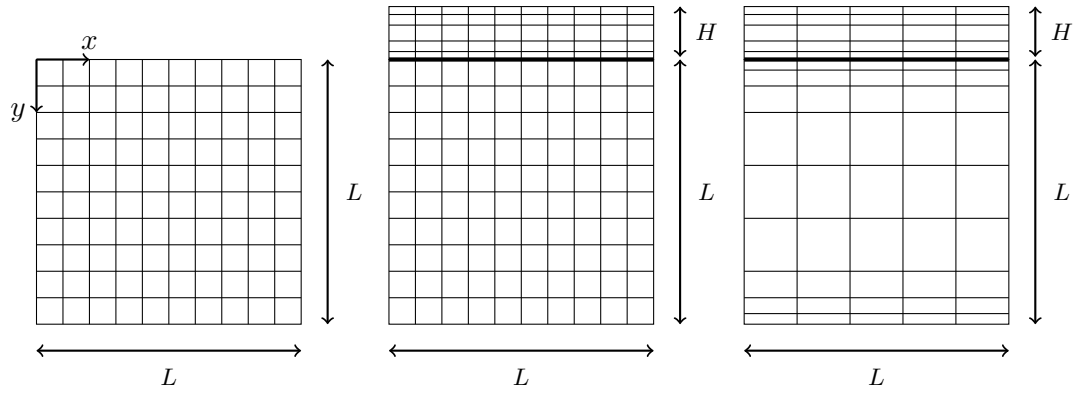

(a) Permeability determination (b) Fine-scale model (c) Coarse-scale model

Figure 2.4: Qualitative schematics of the background spatial mesh employed for the mesh generation of two-dimensional cases using *snappyHexMesh*. The simulation domains are explained in Fig. 2.3 and indicative mesh resolutions are given in Table 2.1.

2D and axisymmetric simulations on any mesh composed of arbitrary polyhedral cells that have an arbitrary number of polygonal faces. The Stokes (1.21) and Brinkman (1.23) equations are solved in the framework of the Semi-Implicit Method for Pressure Linked Equations (SIMPLE) algorithm [92]. All discretisation schemes are second order and the required precision on the pressure and velocity fields is of the order of 10^{-6}.

Specifically, the Navier-Stokes equations coupled with the no-slip boundary condition for the pore walls are solved using the *simpleFoam* solver. The first-order slip boundary condition for velocity (already implemented in `OpenFOAM` by [41, 93]) is herein implemented in a variation of the above solver. For the solution of the Brinkman equation, *porousSimpleFoam* is employed [58].

The numerical solution of the Darcy equation is achieved using a solver derived from the Laplace solver in `OpenFOAM`, i.e. *laplacianFoam*, having as input the permeability field (scalar or tensor) of the coarse-scale grid. The diffusion equation of the pressure field (pressure equation) which is obtained combining Darcy's law (1.2) with the continuity equation (1.21)

$$\nabla \cdot \frac{\mathbf{k}}{\mu} \nabla p = 0. \tag{2.1}$$

Once the pressure field is computed, the velocity field is deduced using Darcy's law. Then, the effective permeability representing the whole domain is obtained. For simplicity or due to availability, most often the scalar or the diagonal of the permeability tensor is used as input. In this work, for non isotropic porous media, the full tensor is employed to increase the accuracy of the results. The main modifications of the *laplacianFoam* solver that led to the Darcy solver, herein called *darcyFoam*, can be found

Table 2.1: Mesh resolution for 2D and 3D cases studied for an indicative fracture of $H = 0.05L$ placed on top of the porous domain, along the y direction. Columns $3, 4$ and 5 correspond to the mesh size of the domains illustrated in Fig. 2.3(a), (b) and (c) respectively. For the 2D case, the QSGS porous medium consists of 1000×1000 pixels while for the 3D case it consists of $100 \times 100 \times 100$ voxels.

		Stokes		Brinkman
		Fig. 2.3(a)	Fig. 2.3(b)	Fig. 2.3(c)
2D	porous block	1000×1000	1000×1000	200×200
	channel block	-	1000×20	200×20
3D	porous block	$200 \times 200 \times 200$	$200 \times 200 \times 200$	$50 \times 50 \times 50$
	channel block	-	$200 \times 20 \times 200$	$50 \times 20 \times 50$

in Appendix A.

Computational mesh

The numerical solution of the Stokes equations requires the binary matrix resulting from the QSGS method to be transformed into a computational mesh, of at least the same resolution (or multiples), consisting of the pore space only. The native `OpenFOAM` mesher, *snappyHexMesh*, is utilised to produce a hexahedral mesh for each geometry. Even though other meshing strategies, e.g. for unstructured grids, are available using this meshing tool, structured hexahedral meshes are a natural choice when simulating rock images (artificial or from real samples) since the available datasets are often in binary format [83]. For the 3D cases, the mesh resolution is doubled in order to increase accuracy. It should be highlighted that the resolution of the computational mesh representing the porous medium refers to the background mesh utilised as a basis for the meshing process of the fluid regions.

The majority of the cases studied in this work follow the configuration shown in Fig. 2.3. When the channel is added on top of the domain then the mesh is manipulated using two blocks . The mesh corresponding to the channel can be coarser in the direction parallel to its thickness by applying multi-grading on the respective axis, achieving thus mesh refinement towards the interface between the free and porous region, and the top boundary.

On the other hand, the numerical solution of the Darcy or Brinkman equation does not necessarily require the same mesh resolution. To reduce the computational cost while maintaining accuracy, a coarser hexahedral mesh is constructed for the whole domain, where the mesh is graded linearly to achieve mesh refinement in the areas of

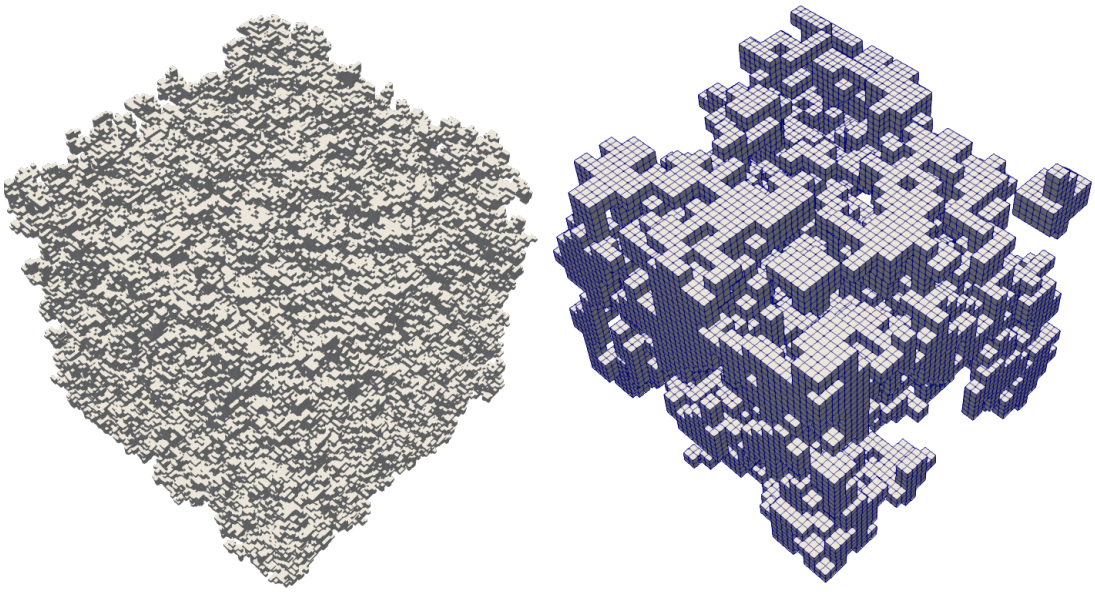

(a) (b)

Figure 2.5: Visualisation of the pore-space mesh produced from a 3D QSGS binary image. (a) The full sample of 100^3 voxels (200^3 cells) and (b) a sub-volume of 25^3 voxels (50^3 cells) are shown.

interest, i.e. towards the top and bottom boundaries and most importantly, in the vicinity of the interface between the free and the porous regions. This is again achieved using two blocks corresponding to the porous and the free region respectively (one block is only needed when the Darcy equation is solved). Generally, refinements around the fractures are necessary to properly solve the steep gradients in the region. The mesh information for both the 2D and 3D cases where a straight channel of thickness $H = 0.05L$ is added along the y axis, on top of the porous domain, is displayed in Table 2.1. Qualitative schematics of the mesh resolution and grading for each of the 2D simulation categories depicted in Fig. 2.3, are shown in Fig. 2.4. The 3D mesh produced from a sample QSGS geometry is depicted in Fig. 2.5.

2.2.2 Gas kinetic theory

Since the variation of apparent permeability is linked to rarefaction effects, gas kinetic theory is adopted to describe rarefied flow in ultra-tight porous media. The Boltzmann equation, the cornerstone of rarefied gas dynamics describes the state of the system utilising the velocity distribution function $f(\mathbf{x}, \mathbf{v}, t)$, which is a pivotal notion of kinetic

theory, as follows

$$\frac{\partial f}{\partial t} + \mathbf{v} \cdot \frac{\partial f}{\partial \mathbf{x}} = \mathcal{C}(f), \tag{2.2}$$

where $\mathbf{v} = (v_x, v_y, v_z)$ is the three-dimensional molecular velocity normalised by the most probable molecular speed $v_m = \sqrt{2RT_0}$ and $\mathbf{x} = (x, y, z)$ is the spatial coordinate normalised by the length $L = AB$ of the computational domain, shown in Fig. 2.6. Time t is normalised by L/v_m and finally f is normalised by $\bar{p}/v_m^3 mRT_0$ with m being the molecular mass.

The full Boltzmann solvers can be classified into the stochastic/probabilistic methods and the deterministic ones. In the former category, a popular method is the DSMC [17], while in the latter, commonly used methods are the discrete velocity method (DVM) [56, 83, 94, 95, 96, 97] and the fast spectral method (FSM) [98]. The particle-based DSMC has been widely used to simulate high-speed rarefied gas flows in space applications however, it is computationally prohibitive for low-speed flows in porous media [99, 100]. There are some studies employing DSMC for porous media flows, however, they focus on high Knudsen numbers [100]. We note that in lieu of the above mesoscopic methods, a microscopic method such as molecular dynamics (MD) can also accurately describe the intermolecular interactions, nevertheless, it is not employed due to its huge computational cost [12].

The Boltzmann collision operator $\mathcal{C}$ represents the intermolecular collisions and is a complicated integral. The operator increases the computational cost and memory requirements of the numerical solution of this non-linear integro-differential equation making its use impractical for many realistic applications. Therefore, the collision integral is often simplified by a relaxation-time approach [97], e.g. Bhatnagar–Gross–Krook (BGK) [101], ellipsoidal-statistical BGK (ES-BGK) [102] or Shakhov model [103]. The above models have been extensively used for a wide range of applications, across the whole spectrum of rarefaction and their accuracy has been assessed [83].

Among the available numerical strategies for the solution of the Boltzmann model equations, the versatile lattice Boltzmann method (LBM) [104] is well accepted by the scientific community, highly developed and successfully applied for simulating porous media flows. This is mainly thanks to the ease of the boundary condition implementation on the complex pore structures [105]. Nonetheless, conventional LBM fails to capture phenomena related to gas rarefaction, even in simple geometries, due to limited number of discrete velocities [106, 107, 108, 109]. Instead, it is demonstrated that high-order LBMs are required when the flow is no longer at the continuum regime in order to obtain accurate solutions [105]. The so-called high-order LBMs are, in fact, a special form of the discrete velocity method (DVM) [95, 97]. DVM has successfully predicted all flow regimes in capillaries with several cross-sectional shapes [110, 111, 112, 113].

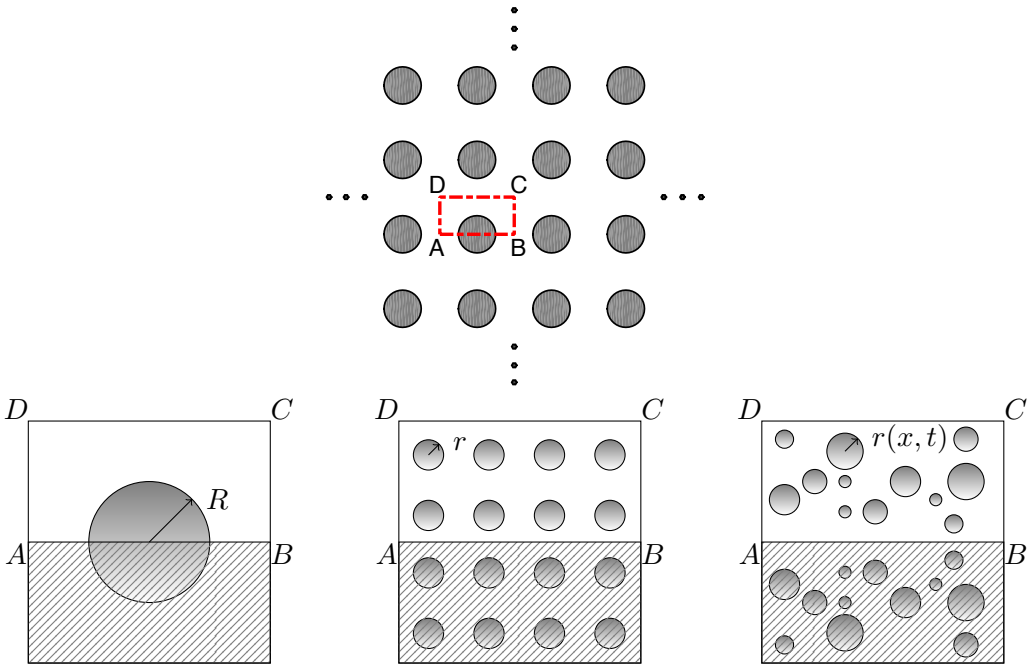

Figure 2.6: Schematic representation of a two-dimensional porous medium. A porous medium consisting of a periodic array of discs can be generated using the concept of the unit rectangular cell $ABCD$; applying periodic boundary condition at sides AD and BC and symmetrical boundary condition along sides AB and CD, respectively. The rectangle $ABCD$ is the computational domain where the length AB is L and AD is $L/2$. Other porous media can be generated by adding more solid particles in this rectangle and maintaining the same porosity. After normalisation, the coordinates of the four corners A, B, C, and D are $(-0.5, 0), (0.5, 0), (0.5, 0.5)$, and $(-0.5, 0.5)$, respectively.

Kinetic model

In the numerical simulations of low-speed rarefied gas flows, it is well documented that the linearised BGK equation is often used as a simplified kinetic model equation [85, 97, 113], Herein BGK is solved by DVM, which approximates the continuous molecular velocity space $\mathbf{v}$ with discrete velocities. The linearised BGK model equation, which can be viewed as the relaxation-time approximation of the Boltzmann equation [101], reads

$$\mathbf{v} \cdot \frac{\partial h}{\partial \mathbf{x}} = \frac{\sqrt{\pi}}{2Kn} \left[\varrho + 2\mathbf{u} \cdot \mathbf{v} + \mathcal{T} \left(|\mathbf{v}|^2 - \frac{3}{2} \right) - h \right], \tag{2.3}$$

where $h(\mathbf{x}, \mathbf{v})$ is the (dimensionless) distribution function deviated from the Maxwellian equilibrium distribution function f_{eq}. The distribution function is linearised as $f =$

$f_{eq}(1+h)$ where f_{eq} is defined as

$$f_{eq} = \frac{\exp(-|\mathbf{v}|^2)}{\pi^{3/2}}. \tag{2.4}$$

Macroscopic quantities appearing in the right-hand side of Eq. (2.3) are the perturbed number density of gas molecules ϱ, velocity $\mathbf{u}$ and temperature $\mathcal{T}$ which are calculated as the moments of the perturbed distribution function h over the velocity space, as follows

$$\varrho = \int f_{eq} h \mathrm{d}\mathbf{v}, \qquad \mathbf{u} = \int \mathbf{v} f_{eq} h \mathrm{d}\mathbf{v}, \qquad \mathcal{T} = \frac{2}{3}\int |\mathbf{v}|^2 f_{eq} \mathrm{d}\mathbf{v} - \varrho \tag{2.5}$$

Note that Eq. (2.3) is valid when the porous medium is so long that the pressure gradient is small, namely, $|Ldp/pdx| \ll 1$ with p being the local gas pressure and x the flow direction.

The kinetic equation Eq. (2.3) has to be supplied with appropriate boundary conditions. Suppose the pressure gradient is applied along the x (horizontal) direction, on the inlet and outlet of the computational domain $ABCD$ in Fig. 2.6 and periodic condition for the flow velocity is used [112]:

$$\begin{aligned} h\left(-0.5, y, v_x, v_y, v_z\right) &= 1 + h\left(0.5, y, v_x, v_y, v_z\right) \text{ when } v_x > 0, \\ h\left(0.5, y, v_x, v_y, v_z\right) &= -1 + h\left(-0.5, y, v_x, v_y, v_z\right) \text{ when } v_x < 0. \end{aligned} \tag{2.6}$$

At lines AB and CD the specular reflection boundary condition is used to account for spatial symmetry:

$$\begin{aligned} h\left(x, 0, v_x, v_y, v_z\right) &= h\left(x, 0, v_x, -v_y, v_z\right) \text{ when } v_y > 0, \\ h\left(x, 0.5, v_x, v_y, v_z\right) &= h\left(x, 0.5, v_x, -v_y, v_z\right) \text{ when } v_y < 0. \end{aligned} \tag{2.7}$$

Finally, at the solid surface, the diffuse-specular boundary condition is used [36]:

$$h(\mathbf{v}\,|\mathbf{v}\cdot\mathbf{n} > 0) = \sigma\varrho_s(\mathbf{n}) + (1-\sigma)h(\mathbf{v} - 2\mathbf{n}(\mathbf{v}\cdot\mathbf{n})), \tag{2.8}$$

where $\mathbf{n}$ is the normal unit vector of the solid surface and ϱ_s is the perturbed gas number density on the solid surface which is computed from the non-penetration condition, i.e. zero-mass flux through the solid surface, as

$$\varrho_s(\mathbf{n}) = -\frac{\int_{\mathbf{v}\cdot\mathbf{n}<0} \mathbf{v}\cdot\mathbf{n}\exp(-|\mathbf{v}|^2)h\mathrm{d}\mathbf{v}}{\int_{\mathbf{v}\cdot\mathbf{n}>0} \mathbf{v}\cdot\mathbf{n}\exp(-|\mathbf{v}|^2)\mathrm{d}\mathbf{v}}. \tag{2.9}$$

The apparent gas permeability, which is normalised by L^2, is calculated by

$$k_a = 2\sqrt{\frac{1}{\pi}} Kn G_P, \tag{2.10}$$

where $G_p = 2\int_0^{1/2} u_x(y)\mathrm{d}y$ is the dimensionless mass flow rate. Based on its calculation method, k_a refers to the diagonal permeability element in the streamwise direction. In a similar fashion, the other elements of the tensor can be obtained.

Numerical Procedures

A hexahedral mesh of double resolution (compared to the one required for the NSEs solution) is utilised to enhance accuracy, particularly when Kn is small. It is straightforward to construct uniform grids from digital images, since the void and matrix pixels (or voxels) are interpreted as fluid and solid points respectively. Apart from the spatial discretisation, the molecular velocity space $\mathbf{v}$ is also discretised into N_v-discrete velocities. Consequently, the BGK model equation (2.3) (where the only unknown is h) is replaced by a system of N_v-independent equations which require numerical solution. Since the non-equilibrium effects are related to the high-order moments of the velocity distribution function, a higher-order quadrature must be used to capture the rarefaction effect accurately. In general, the larger the Kn number, the larger the variations and discontinuities of the velocity distribution function h. Thus, the number of discrete velocities, N_v, should rise accordingly [83, 84, 114]. Using DVM, in this study v_x and v_y in the BGK equation are approximated by the 8×8 Gauss–Hermite quadrature when $Kn < 0.01$ and the Newton-Cotes quadrature with 22×22 non-uniform discrete velocity points for higher Knudsen numbers [21]. The v_z variable can be safely ignored in 2D linearised flows.

In this work, the solution of the BGK model equation (2.3) by the discrete velocity method is realised using an in-house high-performance solver with multi-level parallelization [83]. This gas kinetic solver, developed in Fortran, efficiently utilises the computational resources, allowing the direct simulation of rarefied gas flows in porous media based on digital rock images. The finite difference method is used to approximate the convection terms on the uniform grids produced from these sample images. The discretisation is realised using a second-order upwind scheme, while the set of equations is solved using an iterative scheme. The value of apparent permeability is calculated every n iteration steps and the gas kinetic solver is terminated when the

following convergence criterion

$$\frac{k_a(i) - k_a(i-n)}{k_a(i)} < 10^{-10}, \tag{2.11}$$

is reached, where i is the iteration step. For the cases considered in this thesis, in order to reach convergence usually a few thousand iterations are required. Additionally, apparent permeability evaluation is a time consuming step of the process, thus, herein based on my experience I choose $n = 1000$. For further details regarding the utilised solver and numerical procedure, the reader can refer to [83].

2.2.3 Boundary conditions

In what follows, the boundary conditions used in the various numerical simulations of this thesis, are presented. Where the numerical results of two or more methods are compared, same boundary conditions are applied to ensure consistency.

In continuum flows (no-slip at the solid surfaces) where the NSEs are solved, the direct numerical simulations are performed having the following different flow configurations:

1. Periodic boundary conditions are imposed at the inlet/outlet, symmetry (no-flux condition) at the lateral walls and no-slip at the solid surfaces [21]. The fluid is forced to move in the desired direction by adding a pressure gradient source term in the momentum equation while assuring $Re < 1$. This setup, due to the periodicity imposed, is a priori anticipated to result in a good approximation of the real permeability since it imitates the encapsulation of the considered pore-scale structure within a larger porous medium [115].

2. The alternative setup of fixed pressure at the inlet and outlet to drive the flow is also tested, while the rest remain as above. The pressure difference is maintained low to assure that $Re < 1$.

3. Fixed pressure is applied at the inlet/outlet without periodicity imposed. Symmetry is applied on the lateral faces as above.

4. Finally, the setup which mimics the classical experiment for the measurement of permeability, the permeameter method [116], is tested, i.e. fixed pressure is imposed at the inlet/outlet while the lateral sides are treated as stationary walls. This and the previous simulation setup 3 are considered to provide correct diagonal and off-diagonal permeability terms without excessive computational requirements or special mesh treatment [117], hence they are often preferred in

the present study. This configuration is particularly useful when the aim is a direct comparison of the numerical and experimental data.

Note that my results for the random porous media considered indicate that the resulting permeabilities from all the above configurations are almost identical, presenting a small deviation in the order of 1%. Furthermore, for configurations 1 and 2 the original geometry is extended by a few fluid layers at the inlet and outlet so that the periodic boundary conditions are applicable [58].

When local Kn increases, as previously mentioned in Section 1.3, the intermolecular collision events become insufficient near the walls and slip boundary conditions should then be imposed instead of zero Neumann for velocity. Traditionally, the first order velocity slip boundary condition (FVBC) [36] is coupled with the Stokes equations for gas flows in the slip regime. The employed Maxwell's boundary condition reads

$$u_s = A_1 \lambda \frac{\partial u_x}{\partial y} + \frac{3}{4} \frac{\mu}{\rho T} \frac{\partial T}{\partial x}, \tag{2.12}$$

where x represents the coordinate tangential to the wall and u_s is the slip velocity component aligned with x. The slip coefficient A_1 is considered to be $(2-\sigma)/\sigma$ in the original formulation of Maxwell and is often omitted in the literature since many researchers consider the case of TMAC equal to one (hence $A_1 = 1$). For curved walls, the full form of the expression should be used instead [118]:

$$u_s = A_1 \lambda \left(\frac{\partial u_x}{\partial y} + \frac{\partial u_y}{\partial x} \right) + \frac{3}{4} \frac{\mu}{\rho T} \frac{\partial T}{\partial x}. \tag{2.13}$$

Note that the flows studied in this work are isothermal, thus the last term of the slip boundary condition was safely ignored. For isothermal flows and planar solid walls the second-order velocity slip boundary condition reads [20, 22, 49, 119]

$$u_s = A_1 \lambda \frac{\partial u_x}{\partial y} - A_2 \lambda^2 \frac{\partial^2 u_x}{\partial y^2}, \tag{2.14}$$

where A_1 and A_2 are the slip coefficients. Typical values of these coefficients are proposed by different researchers such as [119, 120, 121]. I adopt the viscous slip coefficient values of the aforementioned publications to my work, (such as $A_1 = 1.15$ for $\sigma = 1$) as to be analysed in the forthcoming *chapters*.

For all the numerical simulations solved by the DVM method the boundary conditions were analogous to configuration 2 as stated in detail in Section 2.2.2. On the solid walls the diffuse-specular boundary condition, Eq. (2.8), is applied as explained in detail in Section 2.2.2. For short, when TMAC is set to unity, we refer to this boundary

condition as the *diffuse boundary condition*.

Moreover, for the Brinkman simulations performed in this thesis the flow configurations 2 or 4 are employed. Even though at the original experiments of Beavers & Joseph [75] the homogeneous and isotropic permeable block was considered to be semi-infinite, herein, at the finite bottom of the porous medium, zero Neumann or zero Dirichlet boundary conditions are applied respectively.

Finally, for the numerical solution of the Darcy equation, the permeameter configuration 4 is herein employed. Since only the pressure and permeability boundary conditions can be determined, while the velocity field results from the simulation, a no-slip boundary condition cannot be explicitly applied at the walls. To circumvent this, the concept of "immersed" boundary conditions can be utilised. Forcing the permeability on the lateral sides to have a sufficiently small value, the velocity there is reduced to orders of magnitude lower than the velocity in the rest of the domain, giving practically the same result as the no-slip boundary condition [67].

2.3 Permeability tensor determination

The permeability tensor is a second order tensor with nine components in the three-dimensional space. The calculation of the full permeability tensor $\mathbf{k}$ of a three-dimensional porous medium requires three flow simulations, imposing pressure gradients in the x, y and z directions respectively. Each simulation for each spatial direction gives one column of the tensor. For example, using Darcy's law (1.2) and imposing ∇p_x the first column of the permeability tensor is obtained by

$$k_{ix} = -\frac{\bar{u}_i \mu}{\nabla p_x} \text{ for } i = x, y, z, \tag{2.15}$$

where $\bar{u}_i$ is the i-th component of the Darcy velocity $\bar{\mathbf{u}}$ which reads

$$\bar{\mathbf{u}} = \frac{1}{V} \int_{V_f} \mathbf{u} \mathrm{d}V, \tag{2.16}$$

with V_f being the volume occupied by the fluid and V the total volume. We note that when the porous medium is two-dimensional, the order of the system is reduced to 2×2. I should further remark that the nature of the permeability tensor depends on the characteristics of the porous medium and the flow configuration (boundary conditions) [117]. For example in the permeameter case, even though the fluxes across the lateral sides are imposed to be zero, the averaged velocity field has non-zero transversal components leading to a non-diagonal permeability tensor. Generally, the computed

tensor is not necessarily symmetrical for pressure-imposed configurations while when periodicity is imposed the derived tensor is symmetrical.

In isotropic porous media the diagonal elements of the permeability tensor are equal ($k_{xx} = k_{yy} = k_{zz} = k$) while the off-diagonal elements are zero (k_{ij} for $i \neq j$). In the case of anisotropic porous media the diagonal elements of the permeability tensor differ.

In this study, the random porous media tested, even when instructed to be statistically isotropic, result in small deviations between k_{xx}, k_{yy} and k_{zz}. The discrepancy between these elements increases with increasing the degree of anisotropy. Due to the boundary conditions applied in the lateral faces, either wall or symmetry, the fluxes across them are equal to zero. However, the averaged velocity field $\bar{\mathbf{u}}$ has non-zero transversal components, leading to a non-diagonal permeability tensor. Additionally, $\mathbf{k}$ is non-symmetric, which is attributed to the non-uniform distribution of the pores. It should be stressed that usually the off-diagonal components of the tensor are at least one order smaller than their diagonal counterparts [115, 117]. For practical reasons, the permeabilities (k, k_a and k_{eff}) mentioned in the forthcoming *sections* and *chapters* are normalised by L^2 and refer to the diagonal permeability element of the streamwise direction, unless otherwise stated.

2.4 Computed quantities

To evaluate the influence of several morphological aspects on the permeability of microporous media, some relevant quantities are taken into consideration. First, streamlines in porous media are usually not parallel to each other and most importantly far from being straight. To quantify this effect a dimensionless parameter called hydraulic tortuosity of preferential flow paths τ is introduced. Tortuosity is defined as the ratio of the average length of microscopic flow paths to the length of the medium in the direction of macroscopic flux L [122, 123]. It is computed herein as a volume integral based on the simplified method [122] for low-Reynolds number flows:

$$\tau = \frac{\bar{u}}{\bar{u}_i}, \tag{2.17}$$

in which i denotes the direction parallel to the macroscopic flow.

Second, gas permeability is significantly affected by the surface area. Thus, the specific surface area [124], S, which is defined as the ratio of the total interstitial surface area to the total volume of the fluid phase (ratio of the perimeter to the total area in 2D), is also computed. Generally, the boost of both tortuosity and specific surface area obstructs the flow, resulting in lower permeability.

Third, shale formations are anisotropic due to the orientation of mineral foliations

and laminated bedding planes. This leads to the description of their macroscopic physical properties, e.g. tortuosity and permeability as tensors rather than scalars. For this reason, both statistically isotropic [124] and anisotropic geometries are produced to evaluate the directional dependency of their properties; for the former geometries tortuosity is herein regarded as scalar while for the latter, as a vector. As far as permeability is concerned, in some occasions, only the diagonal elements are mentioned instead of the full tensor since off-diagonal permeability elements are often reported to have relatively low magnitude [115, 125]. This is confirmed in this work.

The parameter D_i is responsible for the degree of anisotropy in the geometries generated using the QSGS method. In order to obtain isotropic 2D structures, uniform main, D_{main} (D_{1-4}), and diagonal, D_{diag} (D_{5-8}), growth probabilities must be set, with $D_{main} : D_{diag} = 4$. By changing the ratio between the main probabilities, hereinafter referred to as the aspect ratio, AR, anisotropy can be adjusted accordingly. The above also extend to 3D structures.

The anisotropy factor for the intrinsic permeability is reported [115] to have a large range of possible values in various sandstones and thus it is also studied in the present work. The anisotropy factor, A_f, is defined as

$$A_f = \frac{k_{min}}{k_{max}} \text{ for 2D}, \quad A_f = \frac{k_{min}}{\sqrt{k_{int}k_{max}}} \text{ for 3D}, \tag{2.18}$$

where k_{min}, k_{int} and k_{max} correspond to the minimal, intermediate and maximal value of the diagonal permeability tensor respectively (k_{int} being valid only for 3D cases). Values close to unity indicate a statistically isotropic medium, while values close to zero refer to high anisotropy. The diagonal permeability tensor can be derived computing the eigenvalues of the full permeability tensor $\mathbf{k}$ [74].

The size of the pores in the simulated structures can be significantly smaller than the size of the computational domain in the direction of the flow (L). Therefore, the effective characteristic flow length to be used in the calculation of the effective Knudsen number in Eq. (1.12) should not be (L), but an effective pore size (L^*) determined by the expression [40, 53, 56] as follows

$$L^* = L\sqrt{\frac{12k_\infty}{\epsilon}} \text{ for 2D}, \quad L^* = L\sqrt{\frac{8k_\infty}{\epsilon}} \text{ for 3D}. \tag{2.19}$$

The above expressions are chosen in this work, instead of others mentioned in Section 1.3.2 (see Eqs. (1.13) and (1.18)). Note that the dimensional quantities present in this thesis, are in SI units, which are not mentioned for simplicity. I also remind that unless otherwise stated, permeability is hereinafter given in its dimensionless form.

Chapter 3

Slip factor behaviour in simplified porous media

The Navier-Stokes equations with the first-order velocity-slip boundary condition are only accurate to the first order of Kn. However, many researchers erroneously use permeability models derived based on this assumption, to obtain shale gas permeability for the whole rarefaction regime. This *chapter* discusses the limitations of the Navier-Stokes equations coupled with the first-order velocity slip boundary condition to describe rarefied flow in simplified porous media. In Section 3.1, numerical simulations are performed to analyse the variation of apparent permeability with Knudsen number and to assess the validity and applicability of the slip-corrected permeability. In Section 3.2, the influence of gas-surface interaction on apparent permeability and the slip factor is also studied. Possible factors that lead to the observation of Klinkenberg related to the slip factor are identified. The *chapter* concludes with some final comments and remarks.

3.1 Limitations of the Navier-Stokes equations in simplified porous media

The so-called slip-corrected permeability can be obtained either by expanding analytical solutions to the first-order of Kn, either by fitting the numerical solution at small Kn numbers and keeping this linear dependence of k_a with Kn. In some cases, the slip-corrected permeability agrees well with the numerical results of porous media flows, however the simulations performed in this work prove that this is a coincidence and that it can lead to misleading predictions as well.

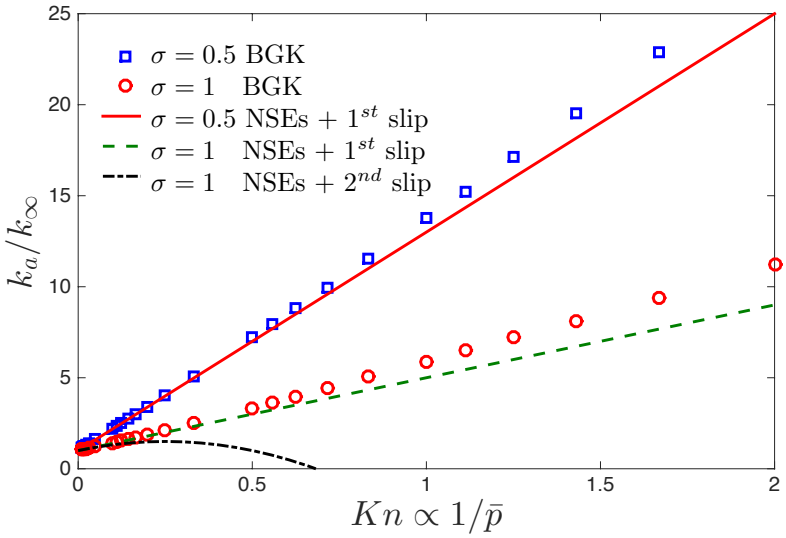

Figure 3.1: The apparent gas permeability versus the Knudsen number for a gas flow in a straight cylindrical tube, obtained from the numerical simulation of the BGK equation, where σ is the tangential momentum accommodation coefficient in the kinetic boundary condition for the gas-surface interaction (see Eq. (2.8)). Analytical solutions of the NSEs with first-order (2.12) and second-order (2.14) velocity slip boundary conditions are also shown, where the viscous velocity slip coefficients are obtained from [120] and [121].

Klinkenberg found that the slip factor b decreases as Kn increases [34]. As previously mentioned in Section 1.3, it is common in the literature to circumvent the complexity and high cost involved in the numerical simulations of porous media by treating them as a single cylindrical tube or as a bundle of identical ones. However, this simplification cannot yield the observation made through Klinkenberg's experiment.

The numerical solutions of the BGK model equation as well as the analytical expressions derived from the NSEs coupled with velocity-slip boundary conditions for gas flows in a straight cylindrical tube are shown in Fig. 3.1. The BGK results indicate that the slip factor b increases with Kn while the NSEs give a constant b. The NSEs with the second order slip boundary condition (2.14) produce the same trend as in the famous experiment [34] for very small Kn, nevertheless, as Kn increases the apparent permeability drops, soon reaching negative values which is not physical. In addition to this, the maximum of this curve is reached for permeability enhanced only by 1.5 times which is in sharp contrast to the numerical experiment where $k_a/k_\infty \approx 30$.

Using the NSEs coupled with the FVBC, apparent permeability for rarefied flow through a periodic array of discs has been derived analytically by [126]. Considering

that the porosity is large k_a is given by

$$k_a = \frac{1}{8\pi\left(1+2A_1Kn\sqrt{\frac{\pi}{P}}\right)}\left[-\ln P-\frac{3}{2}+2P-\frac{P^2}{2}+ \right. \\ \left. +2A_1Kn\sqrt{\frac{\pi}{P}}(-\ln P-\frac{1}{2}+\frac{P^2}{2})\right], \tag{3.1}$$

where $P = 1-\epsilon$ stands for the solid fraction, $\epsilon = 1-\pi r^2/L^2$ and A_1 is the velocity slip coefficient. When Maxwell's diffuse boundary condition (2.8) is used [119], we have $A_1 = 1.016\sqrt{4/\pi} = 1.15$. The viscous velocity slip coefficient for other values of TMAC can be found in [120] and [121].

The above analytical formula for apparent gas permeability is a non-linear function of Kn [126]. Nevertheless, since the formula is based on the NSEs coupled with FVBC, its applicability is limited to the first-order of Kn. Therefore, expanding the formula into a Taylor series around $Kn = 0$ and retaining up to the first-order terms, the accuracy is maintained for the slip regime. This simplified expression, which is called the slip corrected apparent permeability, reads

$$k_a = \frac{1}{8\pi}\left[-\ln P-\frac{3}{2}+2P-\frac{P^2}{2}+2A_1Kn\sqrt{\frac{\pi}{P}}(1-2P+P^2)\right]. \tag{3.2}$$

The accuracy of the analytical formulation (3.2) is assessed by comparing it with the numerical solution of the BGK equations and DSMC results obtained from [127] for a periodic porous medium; a circular cylinder with $\epsilon = 0.8$. The boundary conditions imposed for the following numerical simulations are periodic at the inlet/outlet and symmetry at the lateral sides of the computational domain (unit computational cell, as seen on Fig. 2.6). On the solid walls, the diffuse specular boundary condition is imposed for the gas kinetic theory simulations. When the NSEs are solved, the no-slip or the first-order slip boundary condition is applied.

Note that in the DSMC simulation, the Knudsen number and k_a are normalised by the radius and radius square of the disc, so the data should be renormalised. Also, the mean free path defined in Eq. (1.1) is $15\pi/2(7-2\omega)(5-2\omega)$ times larger than that used in DSMC based on the variable hard sphere model, where $\omega = 0.81$ for argon [98]; so the Knudsen number should be rescaled.

For the linearised BGK equation (2.3), two reduced distribution functions were introduced to cast the three-dimensional molecular velocity space into a two-dimensional one, and the obtained two equations are solved numerically by the discrete velocity method [112]. In the discrete velocity method, a Cartesian grid with 801×401 equally-spaced points is used and the solid surface is approximated by a "stair-case" mesh.

The molecular velocity space in the BGK equation is also discretised: v_x and v_y are approximated by the 8×8 Gauss-Hermite quadrature when Kn is small ($Kn < 0.01$ in this case), and the Newton-Cotes quadrature with 22×22 non-uniform discrete velocity points when Kn is large [128].

The aforementioned results are depicted in Fig. 3.2. Although I use the linearised BGK model, my numerical results are quite close to those from the DSMC simulation [127]. For $Kn \lesssim 0.15$, k_a is a linear function of Kn. The analytical permeability, Eq. (3.1), increases linearly with Kn only when $Kn \lesssim 0.02$, and then quickly reaches to a maximum value when $Kn \gtrsim 0.2$. This comparison clearly demonstrates that, the NSEs with FVBC are only accurate to the first-order of Kn. The slip-corrected apparent permeability is also plotted according to the Taylor expansion, Eq. (3.2). Albeit this expression is expected to be valid at small Kn, it is in good agreement with the BGK numerical results when $Kn \lesssim 0.35$. The error of this slip-corrected formulation is acceptable even in the transition regime, where the permeability is underestimated by only 15% for $Kn = 1$. It should be highlighted that this is but a coincidence, as to be proved in the analysis below.

The assertion regarding the limitation of the accuracy of the NSEs with FVBC to the first-order of Kn applies also to more complicated porous media such as the one shown in Fig. 3.3. This porous medium has porosity 0.6 and consists of non-overlapping circular discs of different radius. The linearised BGK equation in solved, using the DVM method, with a Cartesian mesh of 3000×1500 cells to discretise the spatial domain. For the numerical solution of the NSEs with FVBC an unstructured grid is used. Specifically, a body-fitted computational grid is generated using *snappyHexMesh*, resulting in a mesh of about 600,000 cells of which the majority are hexahedra and the rest few close to the walls are prisms.

In Fig. 3.3 it can be observed that k_a obtained from the solution of the NSEs with FVBC increases linearly when $Kn \lesssim 0.002$ (or $Kn^* \lesssim 0.146$) and then reaches a plateau. The inset figure points out that this solution is accurate when k_a is a linear function of Kn through the comparison with the BGK results. The maximum k_a where the NSEs with FVBC are valid is only about 1.5 times larger than k_∞. Surprisingly, like in the simple porous medium of Fig. 3.2 the slip-corrected permeability estimates k_a to be slightly smaller than the BGK solution even when the flow is greatly rarefied. Particularly, for $Kn = 1$, ($Kn^* = 73Kn$), when the permeability is enhanced already by hundreds of times, the error of the "filtered" solution of the NSEs with FVBC (keeping only the zeroth and first-order terms of Kn) is roughly 15%.

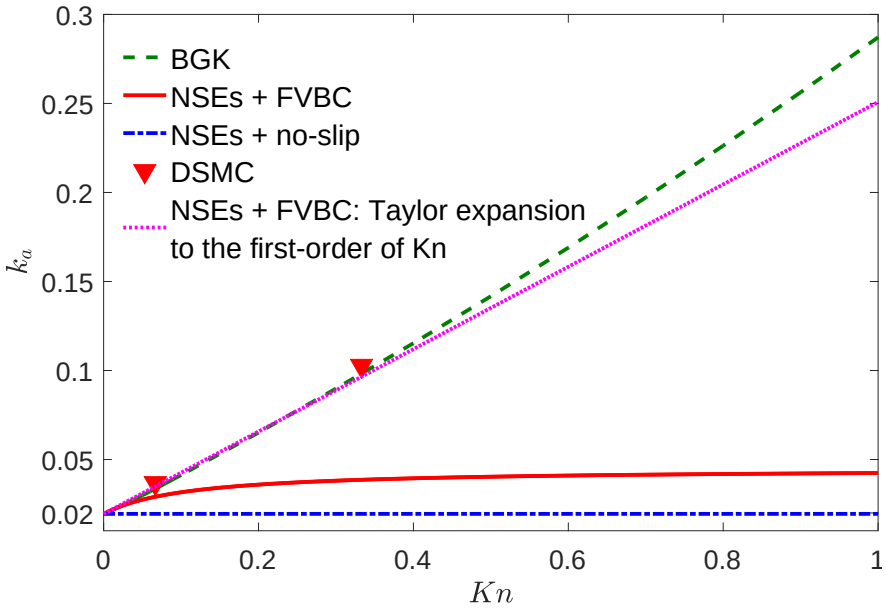

Figure 3.2: Simulation results for flow around a square array of cylinders with porosity $\epsilon = 0.8$. The apparent permeability as a function of the Knudsen number, when the diffuse boundary condition is used, i.e. $\sigma = 1$ in (2.8). The dashed line are numerical results of the linearised BGK solved by the discrete velocity method. The dash-dotted and solid lines are analytical solutions of NSEs (3.1), with the no-slip and first-order velocity-slip boundary conditions, respectively, while the dotted line is the slip-corrected permeability obtained by expanding the analytical solution (3.1) to the first-order of Kn, see (3.2). The DSMC results are obtained from the recent simulation by [127].

3.1.1 Computational time

It will be helpful to mention the computational time for the two examples in Section 3.1. For the discrete velocity method, numerical simulations are performed on Dell workstation (Precision Tower 7910) with dual processors Intel Xeon CPU E5-2630 v3 2.40GHz where 8 threads are used. For simplicity, the 8×8 Gauss-Hermite quadrature is used here for all the Knudsen numbers shown in Table 3.1. For the non-uniform velocity grids, the iteration numbers are roughly the same as the Gauss-Hermite quadrature, but the computational time is about 10 times higher due to the large number of discrete velocity points.

Generally speaking, for the implicit scheme used to solve the gas kinetic equations, the iteration steps increase when the Knudsen number decreases. From Table 3.1 we find that this is true except for the complex geometry where the iteration steps at $Kn = 0.1$ are smaller than that of $Kn = 1$. This is because the sequence of the numerical simulations start from $Kn = 1$; when the solution is converged, it is used as the initial guess in the calculation of $Kn = 0.1$, and so on. Thus, due to this it is

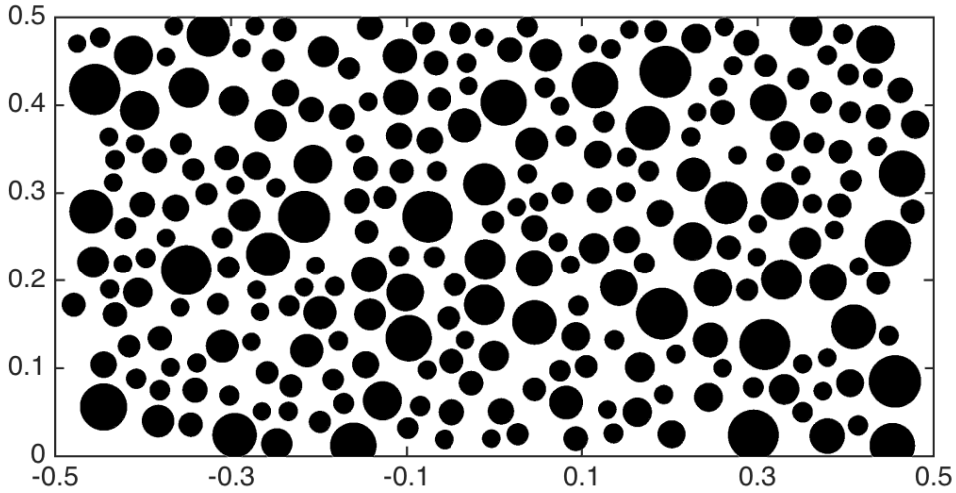

(a)

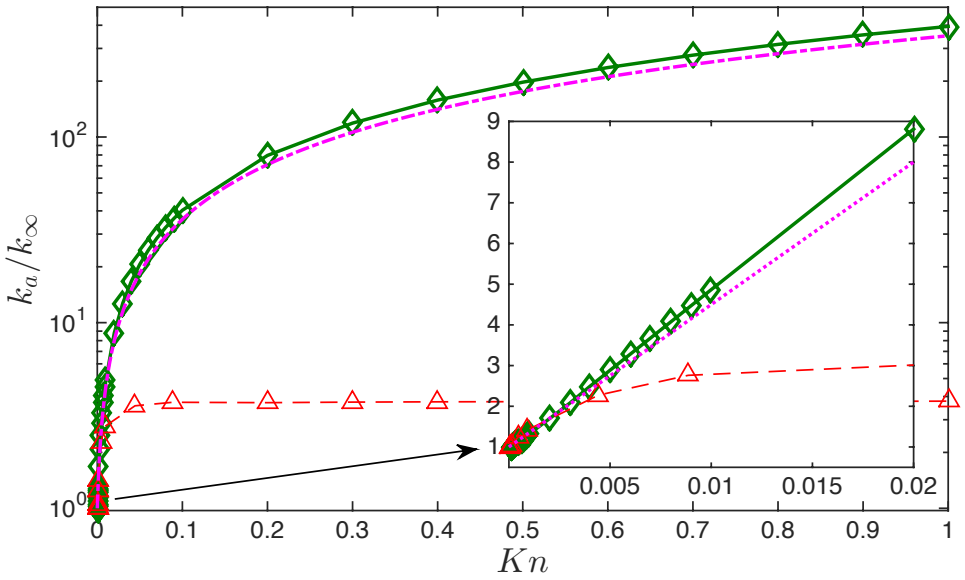

(b)

Figure 3.3: (a) The geometry in a unit computational cell, when the porosity is $\epsilon = 0.6$. Solids of random size and position are shown in black. The periodic porous medium is generated by placing the whole computational domain inside the unit rectangular cell ABCD in Fig. 2.6. (b) The ratio of apparent to intrinsic permeability $k_\infty = 9.37 \times 10^{-6}$ as a function of Knudsen number. The solid and dashed lines are numerical results of the linearised BGK equation and NSEs with FVBC, respectively. The dotted lines are the slip-corrected permeability, obtained from the numerical solution of the NSEs with FVBC, but only keep up to the zeroth- and first-order contributions of Kn. Note that the effective Knudsen number Kn^* (see Eq. (1.12)) is 73 times of Kn.

Table 3.1: Iteration steps and elapsed time for the numerical solution of the linearised BGK equation using the implicit discrete velocity method. The time is measured by wall clock time. The spatial grid size of the circular cylinder is 801×401 points, while for the complex porous medium it is 3000×1500.

Circular cylinder in Fig. 3.2				Complex geometry in Fig. 3.3			
Kn	Kn^*	Iterations	Time (s)	Kn	Kn^*	Iterations	Time (s)
10^0	1.85	2000	68	10^0	7.3×10^1	4000	2076
10^{-1}	0.185	2000	68	10^{-1}	7.3×10^0	3000	1558
10^{-2}	0.0185	7000	238	10^{-2}	7.3×10^{-1}	5000	2584
10^{-3}	0.00185	366000	12381	10^{-3}	7.3×10^{-2}	9000	4943

possible that smaller Kn needs more iteration steps, especially in complicated porous media. Note that for the circular cylinder case at $Kn = 0.001$, the number of iteration steps is large; this is because the flow is in the continuum regime (see Kn^*) where the collision dominates so that the exchange of information due to streaming is extremely slow, and consequently, convergence is slow. In practical calculations, however, we do not have to calculate k_a at such a small Kn, because it is only about 2% larger than intrinsic permeability; we only have to calculate intrinsic permeability using Navier-Stokes solvers, such as the one available in `OpenFOAM`, and the multiple relaxation time lattice Boltzmann method for simulating flows in complex porous media [129].

On the other hand, the `OpenFOAM` solver is running on a Dell workstation with a processor Intel Core CPU i7-6700 3.4GHz that has 8 threads in total. It takes less than half an hour using only one thread to obtain the converged solution for the complex porous medium case in Fig. 3.3, at each Knudsen number. Convergence is considered to be reached when the residuals go below 10^{-6}.

3.2 Possible explanation of Klinkenberg's experiment

For the cases studied in the previous *section*, Klinkenberg's finding that b decreases with Kn is not observed. Conversely, the numerical simulations performed on a straight tube and on simple porous media indicate the opposite trend. In this *section* the impact of non-unitary TMAC on the slip factor is investigated.

From the analytical Taylor expression (3.2), by replacing the non-unitary TMAC (say, $\sigma = 0.5$), then $A_1 \approx 3.23$ [121], making the slip factor about three times larger than in the case of $\sigma = 1$ for small Kn. If at large Knudsen numbers the apparent permeability of $\sigma = 0.5$ is only slightly larger than that of $\sigma = 1$ (this is not the case for

rarefied gas flows between two parallel plates or through a straight cylindrical tube), a decrease of the slip factor when Kn increases may be observed in the numerical simulation of the linearised BGK equation in porous media.

To study the influence of the non-unitary TMAC on the apparent permeability, the rarefied gas flow passing through a square array of square cylinders is investigated. Square instead of circular cylinders, previously used in Fig. 3.2, are chosen so that the specular reflection in the boundary condition (2.8) can be accurately implemented.

Since I use non-dimensional variables, I rewrite Klinkenberg's famous equation (1.3) in the following form

$$\frac{k_a}{k_\infty} = 1 + \frac{b}{\bar{p}} \equiv 1 + b' Kn^*, \tag{3.3}$$

and investigate the variation of the "equivalent slip factor" b', with respect to the Knudsen number and TMAC. Note that b' is proportional to the slip factor b and the proportionality constant is independent of the Knudsen number (reciprocal of mean gas pressure) and TMAC.

The numerical solutions of the linearised BGK equation, solved by the DVM method, are shown in Fig. 3.4, along with the slip-corrected permeability for comparison. The porous media considered have porosity $\epsilon = 0.4$ and $\epsilon = 0.8$ and the TMAC values tested are $\sigma = 1, 0.5$ and 0.1. From Fig. 3.4(c,d) we see that in line with my previous results, for $\sigma = 1$, the slip-corrected permeability agrees well with the numerical results of the linearised BGK equation for both porosities. Interestingly, when $Kn^* \to 0$, the slip factor b' is about 6 and 6.1 when the porosity is $\epsilon = 0.4$ and 0.8, respectively. In parallel, for Poiseuille between two parallel plates, the slip-corrected permeability is exactly

$$\frac{k_a}{k_\infty} = 1 + 6A_1 Kn^*, \tag{3.4}$$

where $A_1 = 1.15$ for the diffuse boundary condition. This means that the slip factor is $b' = 6.9$, which is close to the two values I obtained for the square cylinders, when the gas-surface interaction is diffuse.

However, when the TMAC is small, the accuracy of the slip-corrected permeability is significantly reduced. Since at $\sigma = 0.5$ and 0.1, A_1 is respectively 3.23 and 19.3, the slip factor b' from the NSEs with FVBC is about 17 and 100, respectively. From Fig. 3.4(c,d) we see that the slip-corrected permeability is only accurate when $Kn^* < 0.1$. At relative large Knudsen numbers (i.e. $Kn^* > 0.5$), the accuracy of the slip-corrected permeability is greatly reduced. For instance, for the largest Kn^* shown, when the porosity is 0.8, the slip-corrected permeability overpredicts k_a by 160% and 670%, when $\sigma = 0.5$ and 0.1, respectively; when the porosity is 0.4, the slip-corrected permeability overpredicts k_a by 360% when $\sigma = 0.1$. These two examples clearly show that, when the TMAC

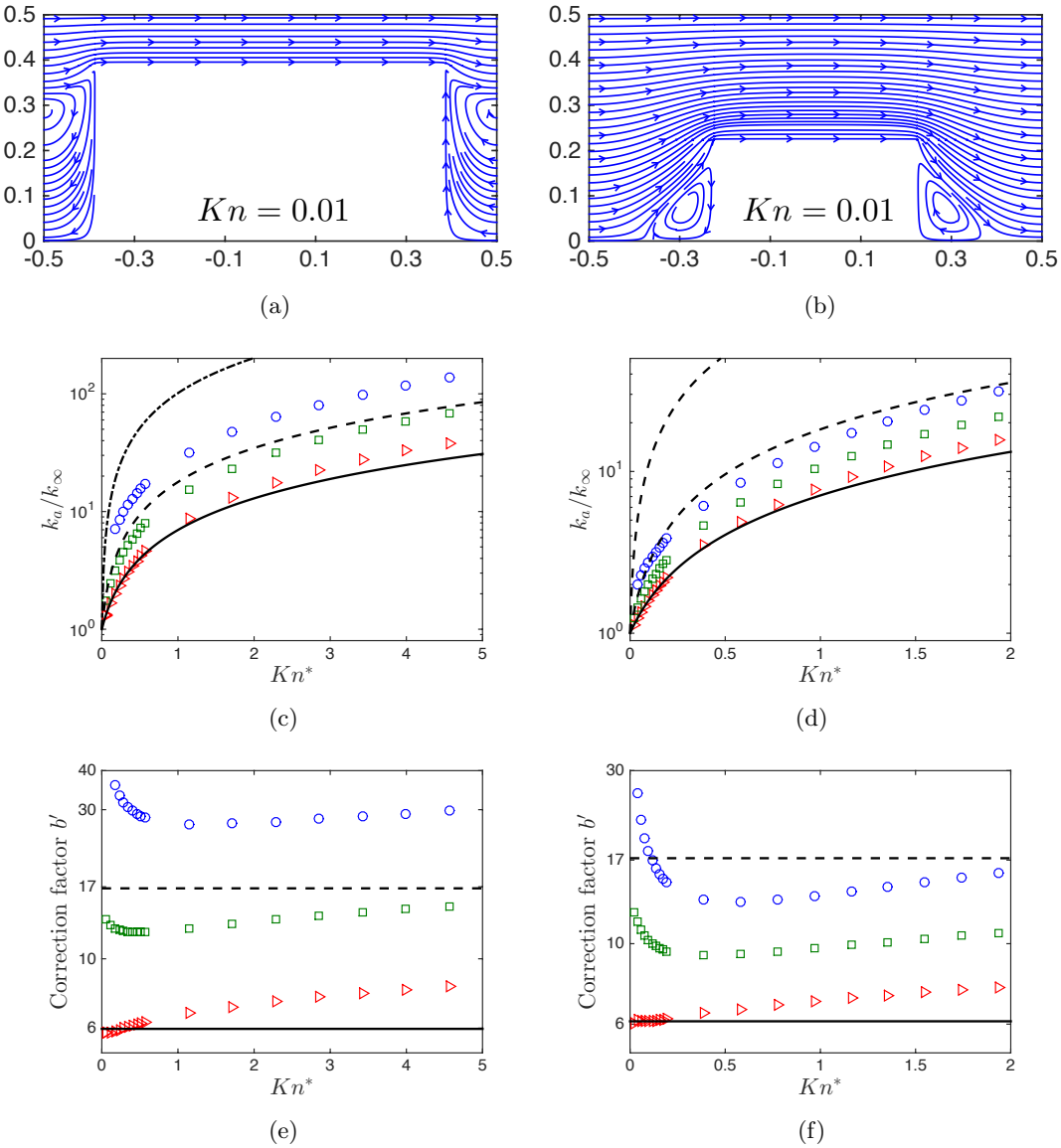

Figure 3.4: (First row) Streamlines in unit computational cells. (Second row) The ratio of the apparent to the intrinsic permeability and (Third row) the slip factor, as a function of Kn^*. Note that the vertical axis in (e) and (f) is in the logarithmic scale. Triangles, squares, and circles are numerical results of the linearised BGK equation (solved by the discrete velocity method), with the TMAC $\sigma = 1.0$, 0.5, and 0.1, respectively. The black lines are the numerical solutions from the NSEs with FVBC, where only up to the first-order terms of Kn are retained. The solid, dashed and dashed-dotted lines correspond to $\sigma = 1.0$, 0.5, and 0.1, respectively. In the left column, the porosity is $\epsilon = 0.4$, $k_\infty = 0.001$, and $Kn^* = 5.69Kn$, while in the right column, $\epsilon = 0.8$, $k_\infty = 0.018$, and $Kn^* = 1.94Kn$.

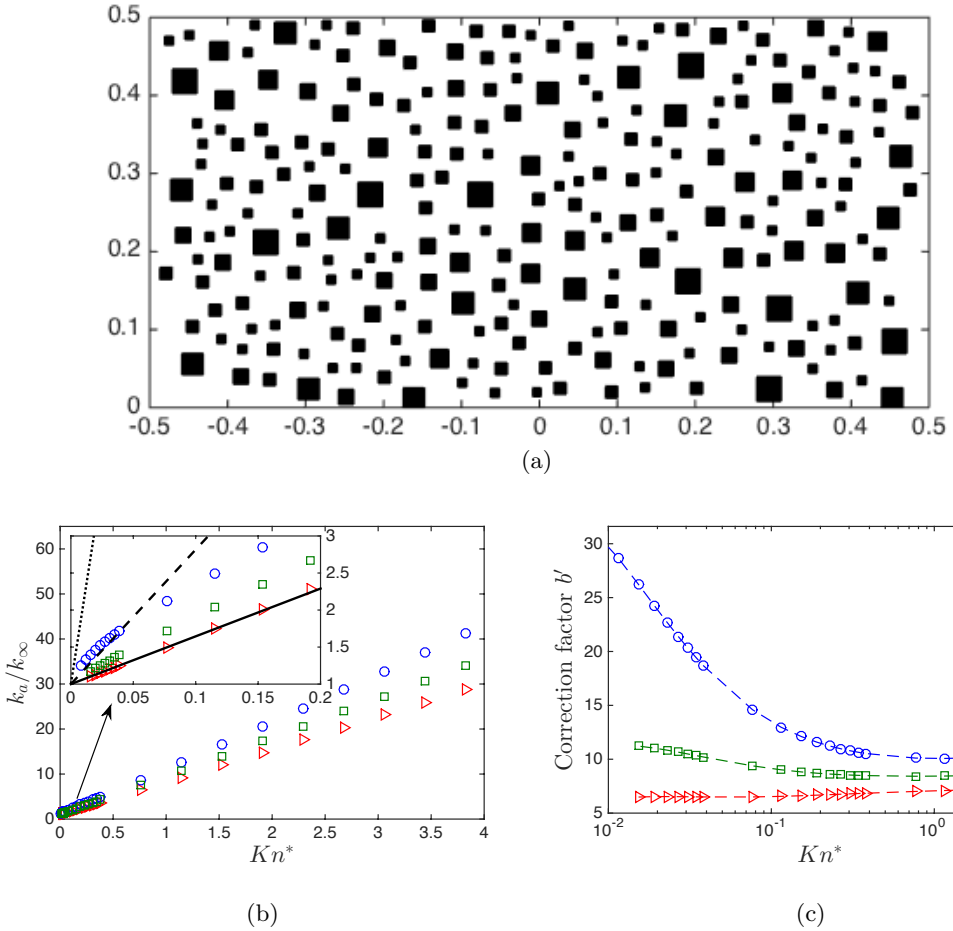

Figure 3.5: (a) The geometry in a unit computational cell, when the porosity is $\epsilon = 0.84$. Solids of random size and position are shown in black. The periodic porous medium is generated by placing the whole computational domain inside the unit rectangular cell ABCD in Fig. 2.6. 2000×1000 cells are used to discretise the spatial domain. (b) The ratio of k_a to the intrinsic permeability $k_\infty = 4.77 \times 10^{-5}$ and (c) The slip factor b', as a function of Kn^*. Triangles, squares, and circles are numerical results of the linearised BGK equation, with the TMAC $\sigma = 1.0$, 0.5, and 0.1, respectively. In the inset in (b), the solid, dashed, dotted lines are the slip-corrected permeability for $\sigma = 1.0$, 0.5, and 0.1, respectively, where the slopes (slip factor b') are 6.45, 18.2, and 108.5, respectively. Note that $Kn^* = 38.3Kn$.

deviates largely from one, the NSEs with FVBC should not be used to predict the apparent permeability in porous media flows beyond the slip regime.

Focusing on the influence of the non-unitary TMAC on the slip factor, when Kn is fixed, k_a increases when TMAC decreases as expected (see Fig. 3.4(c,d)). However, at different Kn the amount of increase is different, so the variation of b' with respect to Kn is quite different among the three TMACs considered. When $\sigma = 1$, it is seen that the slip factor b' increases with Kn, which clearly contradicts Klinkenberg's experimental results. However, when $\sigma = 0.5$ and 0.1, it is found that, when Kn increases, b' first decreases and then increases. The reason that the slip factor increases with the Knudsen number can be easily understood. It is well-known that, when $Kn \to \infty$, the dimensionless mass flow rate G_p in (2.10) increases with Kn logarithmically for Poiseuille flow between two parallel plates [130] and approaches a constant for Poiseuille flow through the cylindrical tube. Similar behaviours for G_p are observed for all the cases considered in this study. According to Eq. (3.3), the equivalent slip factor b' at $Kn^* \to \infty$ can be calculated as follows:

$$b' = \frac{k_a/k_\infty - 1}{Kn^*} = \frac{2KnG_p/\sqrt{\pi}k_\infty}{Kn^*} - \frac{1}{Kn^*} \equiv C - \frac{1}{Kn^*}, \tag{3.5}$$

where C is proportional to G_p. Depending on the structure of the porous medium, C is either a constant or increases with Kn when $Kn \to \infty$. Therefore, the slip factor approaches a constant or increases with Kn. Also, since G_p always increases when TMAC decreases, at large Kn, the slip factor increases when TMAC decreases, see Fig. 3.4(e,f).

These findings also apply to less simple porous media such as the one depicted in Fig. 3.5(a). A similar trend in the variation of the slip factor with respect to the Knudsen number is observed for non-unitary TMACs, see Fig. 3.5(c). Also, from the inset of Fig. 3.5(b) we see that even the slip-corrected permeability, obtained from the NSEs with FVBC, is only accurate when $k_a/k_\infty \lesssim 1.5$ when $\sigma = 0.5$ and 0.1.

So far, two key factors that could lead to the observation that the slip factor b in (1.3) decreases when Kn increases have been identified. The first factor is that the TMAC should be less than 1, and the second one is that flow streamlines should be tortuous. The two factors should be combined together to explain Klinkenberg's observations for the simplified porous media that preceded. However, this assertion should be investigated for complex porous media.

3.3 Conclusions

The above theoretical and numerical analysis proves that the Navier-Stokes equations with the first-order velocity-slip boundary condition can only predict apparent gas permeability of porous media to the first-order accuracy of the Knudsen number. Although the slip-corrected expression, which only retains the linear dependence of permeability and Knudsen number, gives a good approximation of apparent permeability for the diffuse gas-surface boundary condition in a wide range of gas rarefaction, its accuracy is significantly reduced when the tangential momentum accommodation coefficient σ, in the diffuse-specular boundary condition, deviates from one. Even the acceptable agreement of the expression for $\sigma = 1$ could be a coincidence and should be investigated for complex porous media which resemble the porous media of interest.

Therefore, the slip-corrected expression is of no practical use. This issue must be properly taken into account since the Navier-Stokes equations are widely misused in rarefied gas flows to predict apparent gas permeability. This work also implies that all currently widely used empirical solutions, such as (1.10) derived from the straight cylindrical tube with the diffuse boundary condition, should be reformulated to incorporate tortuosity and/or diffuse-specular scattering, to predict unconventional gas production by feeding apparent gas permeability into upscaling models.

Chapter 4

Pore-scale shale permeability

It is known that porosity, specific surface area, tortuosity and anisotropy are some of the matrix properties that play a significant role in the overall production performance. This *chapter* aims to investigate the impact of the aforementioned parameters on both intrinsic and apparent permeability and propose new appropriate permeability formulations which take them into account. On top of this, the behaviour of the slip factor is carefully analysed to examine whether the conclusions of the previous *chapter* hold for the complex porous media under consideration. In Section 4.1, the simulation results are discussed, analysing the role of porosity, specific surface area, tortuosity and anisotropy on intrinsic permeability. Additionally, a new formulation for intrinsic permeability, based on an existing analytical formula along with the simulation results of this work, is presented. Later, in Section 4.2, the simulation results for apparent permeability are presented and the impact of structural parameters, reflected on the enhancement ratio and the slip factor, is discussed in detail. Moreover, the proposed formulation is extended to account for slip flow, thus providing apparent permeability. Finally, this *chapter* closes with some conclusions.

4.1 Intrinsic permeability of ultra-tight porous media

4.1.1 Intrinsic permeability results

Many micro-porous media structures (400 to be exact) are generated to investigate the impact of the variation of morphological features on intrinsic permeability. The 2D QSGS structures in this *chapter* consist of $N_x \times N_y = 1000 \times 1000$ pixels. In all the produced geometries the final porosity is slightly smaller than the nominal. Ten geometries are produced for every set of parameters (to reduce the error caused

by the random growth process) and simulations are performed for flow in both the horizontal (x) and vertical (y) directions to account for the possible anisotropy. The boundary conditions imposed on the sides of the computational domain are periodic at the inlet/outlet, symmetry at the lateral walls and no-slip at the solid walls. Due to the periodicity imposed, the computational mesh is extended by a few fluid layers as required, resulting to a 1010×1000 grid. The fluid is forced to move in the desired direction by adding a pressure gradient source term in the momentum equation while assuring $Re < 1$. The alternative setup of fixed pressure in the inlet and outlet to drive the flow is also tested and the calculated permeabilities have a small deviation in the order of 1%. Therefore, in this context, the method of imposing the pressure gradient seems to have a weak impact on the evaluation of the permeability tensor.

In some of the following graphs, for each configuration, the mean value of the computed quantity is shown, while in others all the values are displayed in scatter plots for better visualisation of their deviation. The permeability (both intrinsic and apparent) appearing in the graphs and the equations below is given in its non-dimensional form, by dividing its value with the square of the length of the computational domain in the streamwise direction (L^2).

To begin with, Fig. 4.1 shows the effect of porosity change on physical properties. The results are based on flow simulations on porous media with nominal porosities varying from 0.5 to 0.9 and fixed core distribution probability $c_d = 0.001$ and $AR = 1$ (sample structures are shown in the first row of Fig. 2.2). It should be noted that for this set of parameters, porosity $\epsilon = 0.45$ is the percolation threshold, i.e. the lowest porosity where the fluid is allowed to flow. For lower porosities permeability vanishes. It can be observed that the final porosity is smaller than the nominal up to almost 6% with decreasing porosity. Furthermore, when the value of the core distribution probability is fixed, specific surface area and tortuosity decrease with porosity, leading to higher permeability. Tortuosity and permeability in both flow directions seem to have close, almost overlapping mean values notably for high porosities. This is reasonable, since the geometries are generated to be statistically isotropic and at high porosities nearly each obstacle constitutes a separate island. However, near the percolation threshold isotropy is disrupted due to the many overlapping particles which change their aspect ratio. It can be also observed that the slope of permeability for low porosities is different compared to higher ones.

The scatter plots in Fig. 4.1 reveal the heteroscedasticity of the data, meaning that the variation of τ or k_∞ differs depending on the value of porosity. Nevertheless, a general trend can be observed; small values of porosity yield a large scatter in tortuosity τ and thus permeability k_∞, while the opposite happens for large porosities. An

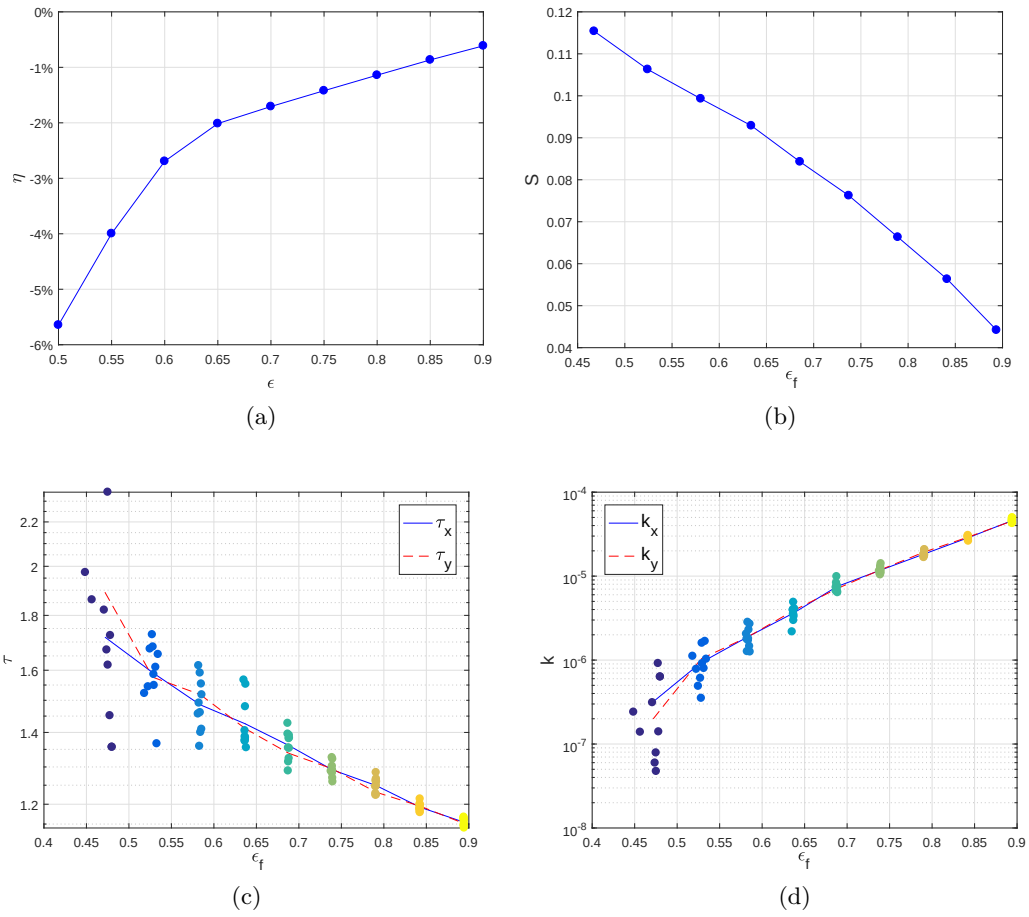

Figure 4.1: Numerical results for geometries with core distribution probability $c_d = 0.001$ and aspect ratio $AR = 1$. Variation of the relative error η of final porosity ϵ_f with nominal porosity ϵ and variation of the specific surface area S with ϵ_f in the first row. Variation of tortuosity τ and permeability k_∞ in the second row; the data points refer to k_x and τ_x, respectively and the points with the same colour correspond to the ten QSGS geometries constructed using the same set of parameters. The trend of the properties in the x direction is indicated with a solid line, while in the y direction a dashed line is used.

explanation for the large scatter could be that for porosities close to the percolation threshold, particles overlap in random ways for each geometry and this creates different tortuous flow paths. Consequently, tortuosity can vary significantly even for the same value of porosity, leading to great discrepancies in permeability.

In addition to porosity, the impact of the core distribution probability c_d variation (sample structures are shown in the second row of Fig. 2.2) while the other two parameters are fixed ($\epsilon = 0.7$ and $AR = 1$) is also studied. The results are presented in Fig. 4.2.

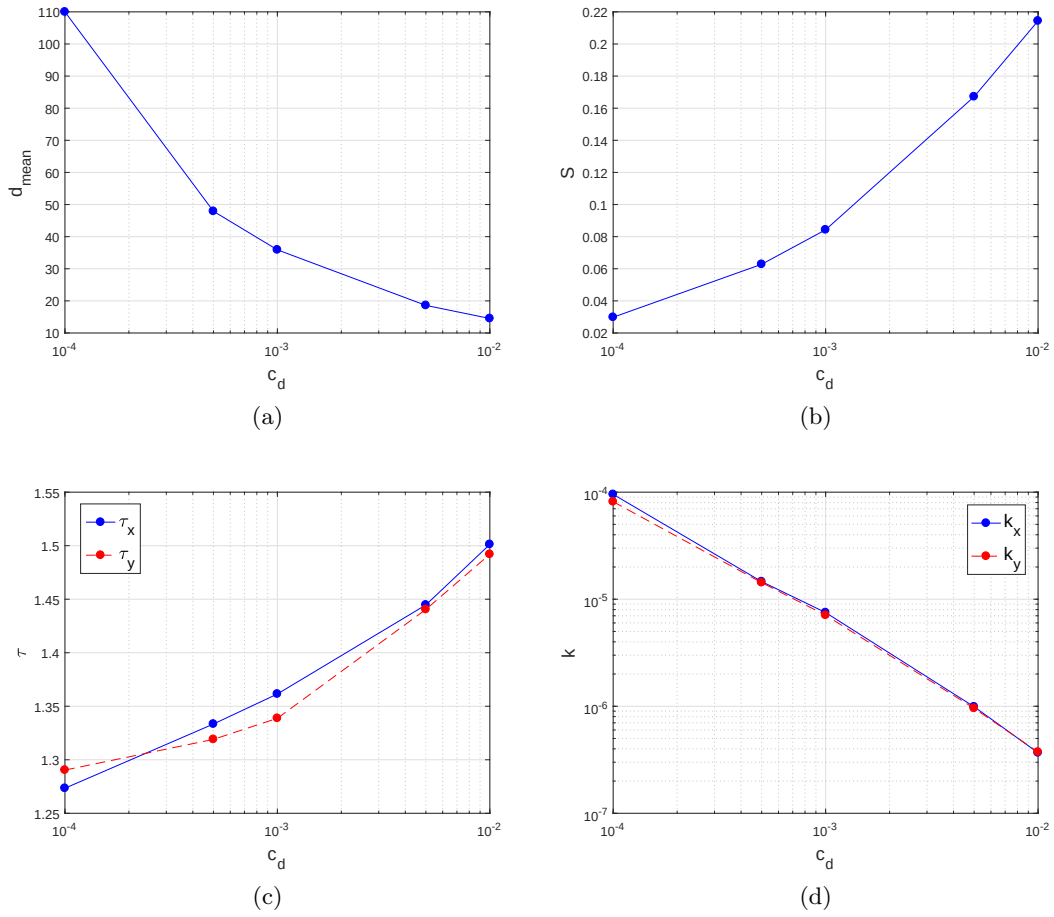

Figure 4.2: Numerical results for geometries with porosity $\epsilon = 0.7$ and aspect ratio $AR = 1$. Variation of the mean diameter d_{mean} and specific surface area S with the core distribution probability c_d in the first row. Variation of tortuosity τ and permeability k_∞ with c_d in the second row. The trend of the properties in the x direction is indicated with a solid line, while in the y direction a dashed line is used.

Increasing c_d the number of particles rises, their size is reduced and therefore these geometries tend to become homogeneous. This fact is reflected on both tortuosity and permeability curves, whose components happen to almost coincide in both directions. Through these graphs, it is apparent that the drop of grain size (roughly described by the mean diameter d_{mean}) leads to significant permeability decline, mostly due to the increment of the specific surface area, since porosity is the same and tortuosity changes only a little in this case.

Finally, the third factor taken into consideration is the degree of anisotropy (sample structures are shown in the third row of Fig. 2.2). The generated micro-porous media

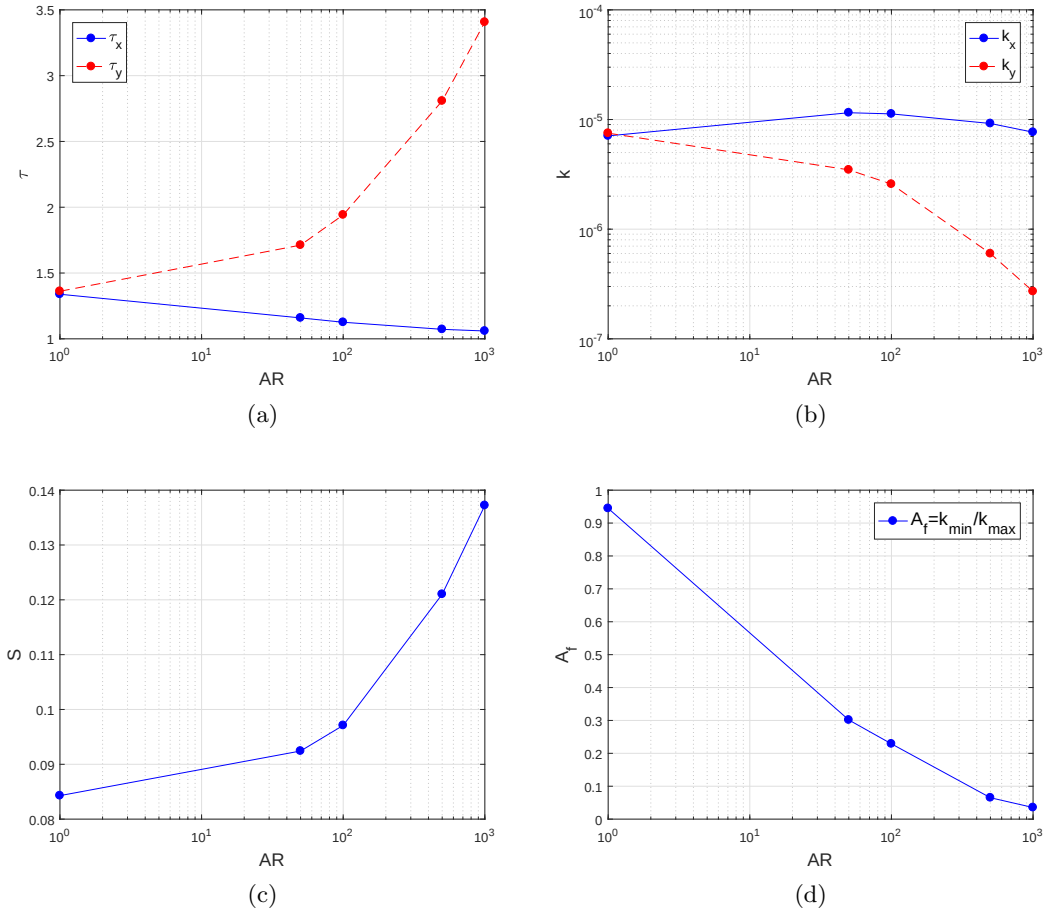

Figure 4.3: Numerical results for geometries with porosity $\epsilon = 0.7$ and core distribution probability $c_d = 0.001$. Variation of tortuosity τ and permeability k_∞ with aspect ratio AR in the first row. Variation of specific surface area S and anisotropy factor A_f with AR in the second row. The trend of the properties in x direction is indicated with a solid line, while in y, a dashed line is used.

are produced by maintaining $\epsilon = 0.7$ and $c_d = 0.001$. Flow simulations are performed both in x direction, where the directional growth probability is larger, and in y direction. Based on the graphs shown in Fig. 4.3 the enlargement of the specific surface area and more importantly of tortuosity leads to a serious decline of permeability k_y. This is due to the obstacles having a large height to width ratio, exerting more resistance to the flow and obstructing many flow paths.

In the x direction where the particles are more stretched, by decreasing the height to width ratio, (increasing AR) flow paths tend to become less sinuous, nearly horizontal, and as a consequence, tortuosity approaches unity. However, as increasing S reduces

permeability, from Fig. 4.3b it is found that k_x does not grow monotonically as expected, but roughly remains in the same order of magnitude. This is due to the competition between the favourable τ and the unfavourable S. Initially, the beneficial impact of tortuosity dominates, however as the particles become more stretched and S increases radically, again they exert more resistance to the flow blocking passages and leading to a small drop of permeability. The peak of k_x curve for these simulated anisotropic QSGS structures is observed to be at $AR = 50$. Finally, the anisotropy factor A_f varies from 0.95 for the statistically isotropic geometry (less anisotropic porous medium) to 0.03 for the most anisotropic samples for the AR region considered.

4.1.2 Intrinsic permeability formulation

In this *section* I consider how to fit intrinsic permeability of the 2D geometries generated by the QSGS algorithm, utilising analytical expressions. Dimensional analysis suggests that Darcy permeability is a function of the porosity ϵ, tortuosity τ, and specific surface area S. One of the most well-known permeability correlations, initially developed by Kozeny [52] and later revisited by Carman [51], is the following semi-empirical formula

$$k_\infty = \frac{\epsilon^3}{c\tau^2(1-\epsilon)^2 S^2}, \tag{4.1}$$

where c is the Kozeny-Carman (KC) coefficient or otherwise stated as shape factor. The above formulation was derived under the assumption that the porous medium is consisted of a bundle of capillaries of fixed cross-sectional shape. The KC expression is widely used for various 2D and 3D porous media [37, 131].

A vast number of researchers, inspired by the work of Kozeny, have established correlations of permeability for different types of porous media. However, these expressions require numerical or experimental data to derive the values of the fitting parameters. The essential derivation of a permeability-porosity relationship of mudrocks is a challenging task due to the complexity of the morphological features of these ultra-tight porous media [37]. In this study, this problem is addressed by fitting tortuosity and permeability using the aforementioned independent variables (controlling parameters) i.e. porosity ϵ, core distribution probability c_d, and aspect ratio AR.

Isotropic geometries

In order to derive an accurate model for intrinsic permeability of isotropic geometries ($AR = 1$), several QSGS structures are generated; specifically for $c_d = 0.001, 0.005, 0.01$ and porosities ranging from the vicinity of the percolation threshold, to $\epsilon = 0.9$. At

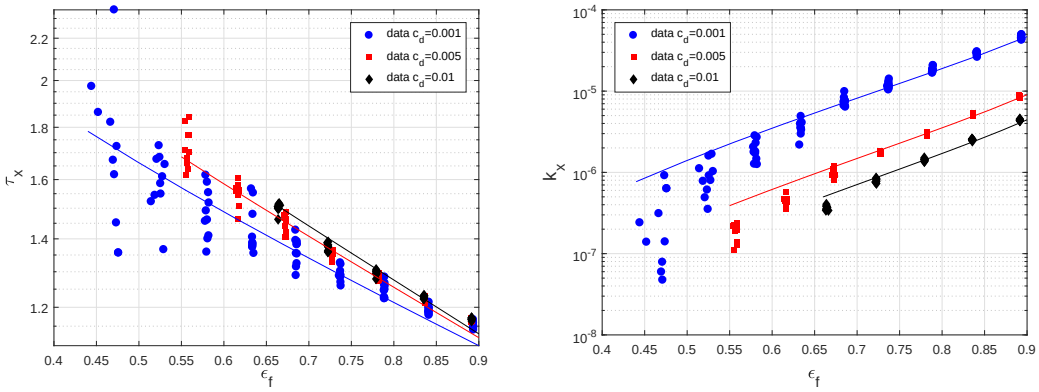

(a) (b)

Figure 4.4: Visualisation of intrinsic permeability formulation results for isotropic geometries. Fitting tortuosity with equation (4.2) and the permeability with equation (4.4).

this point, it should be noted that increasing c_d and consequently the number of solid islands, leads to the percolation threshold being at a higher porosity. Simultaneously, since the solid islands are smaller and thus less likely to overlap, the permeability k_∞ and tortuosity τ are less heteroscedastic. This assertion is aligned with the conclusion of [87] that the scope of the fluctuations highly depends on the sample size (number of particles).

The first step to derive a formulation similar to KC is the generalisation of tortuosity as a function of the independent parameters that determine the structure, i.e. ϵ and c_d. Based on numerical simulations on 2D porous matrices of freely overlapping square particles, where several established expressions for tortuosity were tested, the tortuosity correlation providing the best fit was $\tau = 1 - a_1 \ln(\epsilon)$, where a_1 is a fitting parameter [123, 132]. This expression is thus used in the present study as a starting point for the correlation of $\tau = f(\epsilon, c_d)$. The relevant tortuosity data and appropriate fitting (as seen in Fig. 4.4a) result in a formulation of the following form

$$\tau = 1 - a_1 {c_d}^{a_2} \ln(\epsilon), \tag{4.2}$$

where $a_1 = 2$ and $a_2 = 0.11$.

Considering the two-dimensional porous medium as a periodic array of circular discs with radius r, as in the first schematic diagram of Fig. 2.6, the analytical formula for

permeability, which is accurate for high porosities, reads [126]

$$k_{\infty,c} = \frac{1}{8\pi}\left[-\ln P - \frac{3}{2} + 2P - \frac{P^2}{2}\right], \tag{4.3}$$

where $P = 1 - \epsilon$ stands for the solid fraction and $\epsilon = 1 - \pi r^2/L^2$.

More complex porous media can be generated by replacing the cylinder with numerous solid particles as shown in the last two schematics of Fig. 2.6 [21]. While keeping the same porosity, the analytical formula could be used, although certain modifications would be imperative. To begin with, in order to use the analytical model which is based on a regularly ordered medium of high porosity to evaluate the tested structures of randomly placed and often overlapping particles, the effect of the tortuous flow paths should be considered utilising the factor τ^{-2}. This factor influences the slope of the permeability curve. Apart from this, the number of solid islands, which affects the permeability as discussed previously, should also be taken into account. This reasoning yields the following fitting formula

$$k_{\infty,random,is} = \frac{k_{\infty,c}}{a_3 g \tau^2}, \tag{4.4}$$

where the factor $g = N_x N_y c_d$ refers to the nominal number of solid islands and a_3 is an adjustable parameter. I remind here that $N_x \times N_y$ is the resolution of the QSGS binary matrix. The physical meaning of a_3 reflects the impact of the particles' shape.

Suitable fitting yields $a_3 = 0.7$ and the related curves are shown in Fig. 4.4b. The fitting of the tortuosity is less accurate for high porosities. On the other hand, as expected, the fitting of the permeability is satisfactory for high porosities but the permeability is overestimated close to the percolation threshold, notably for geometries with small c_d which are more heterogeneous.

Anisotropic geometries

It is of central importance to extend and revise the permeability expression to include anisotropic structures, since the shale matrix can be highly anisotropic. To this end, further anisotropic geometries are generated for several porosities ranging from the vicinity of the percolation threshold, to $\epsilon = 0.9$, while the core distribution probability is fixed at $c_d = 0.001$ and the aspect ratio $AR = 100$ or 1000. In Fig. 4.5 their simulation results are compared with those of the corresponding (for the same c_d) isotropic geometries and appropriate fitting is applied. It is obvious that the effect of the elongation of the solid islands is more pronounced for lower porosities, where tortuosity is highly increased and permeability is severely attenuated.

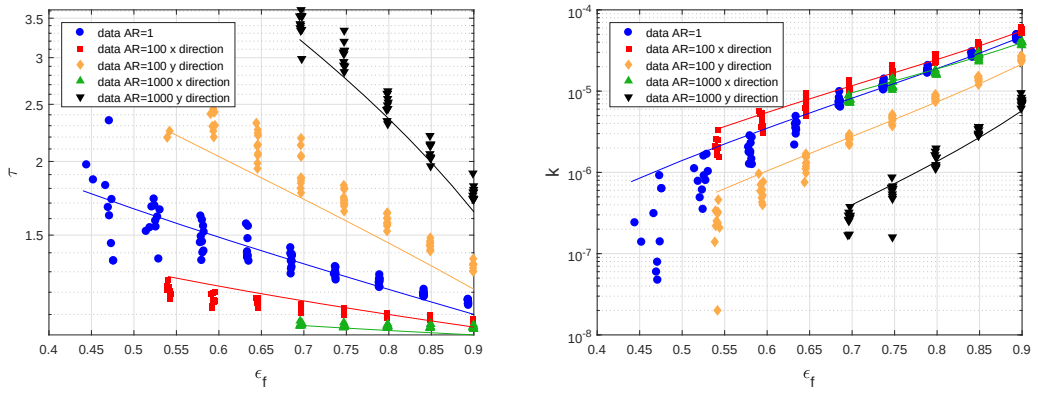

(a) (b)

Figure 4.5: Visualisation of intrinsic permeability formulation results for both isotropic and anisotropic geometries with core distribution probability $c_d = 0.001$. Fitting of tortuosity with equation (4.5) and permeability with equation (4.6).

Tortuosity is fitted with the same equation as in the isotropic cases but adding the contribution of AR as follows

$$\tau = 1 - a_1 {c_d}^{a_2} AR^{a_5} \ln(\epsilon), \tag{4.5}$$

where $a_2 = 0.11$ as previously fitted. In the direction of the elongation of the islands (x) the flow is facilitated, tortuosity approaches unity and $a_1 = 8.8$ while $a_5 = -0.48$. In the perpendicular direction (y), we obtain $a_1 = 0.5$ and $a_5 = 0.48$.

The correct approximation of tortuosity allows the estimation of permeability utilising the same expression as in isotropic geometries, with the exception that the adjustable parameter a_3 changes significantly. This modification is necessary since the analytical expression in Eq. (4.3) is derived for cylindrical discs, while in the anisotropic structures solid islands are far from being so. The degree of anisotropy AR is also taken into account and the resulting formula reads

$$k_{\infty,random,an} = \frac{k_{\infty,c}}{a_3 g AR^{a_4} \tau^2}. \tag{4.6}$$

In anisotropic structures, the particles' shape is more ellipsoidal and hence, the particles are less likely to overlap. Thus fitting yields $a_3 = 0.3$. The exponent a_4 is adjusted according to the direction of the flow. For the computation of permeability in the x direction $a_4 = 0.17$ while in the y direction, $a_4 = 0.31$. The fitted formulation is shown in Fig. 4.5, where we can observe that even though the fitting of tortuosity is not ideal, the permeability formulation yields a good approximation of the actual permeability,

especially for high porosities, as expected.

To conclude, Eq. (4.6) models intrinsic permeability for both isotropic ($AR = 1$) and anisotropic QSGS structures, requiring the calculation of tortuosity using Eq. (4.5). The above equations depend only on the independent variables ϵ, c_d and AR and their coefficients are fixed according to the above cases. As a result, this permeability formulation includes five fitting parameters, which unlike others in the literature are the same regardless of particle shape and size. Table 4.1 summarises the aforementioned coefficients for each case. Consequently, the proposed intrinsic permeability estimation for random two-dimensional porous media generated by the QSGS method is straightforward since it does not entail any numerical simulations.

Table 4.1: Fitting coefficients for intrinsic permeability formulation Eq. (4.6).

Structure	Flow direction	a_1	a_2	a_3	a_4	a_5
Isotropic	any	2	0.11	0.7	-	-
Anisotropic	x	8.8		0.3	0.17	-0.48
	y	0.5			0.31	0.48

4.2 Apparent permeability of ultra-tight porous media

4.2.1 Apparent permeability results

The various morphological features of the aforementioned two-dimensional complex porous media, unambiguously affect apparent gas permeability. Numerical results of the linearised BGK solved by the DVM reveal the relationships between the controlling parameters of the QSGS structures and apparent permeability. Due to the high computational cost [83], numerical results of only four porous structures are compared across a wide range of Kn numbers. Nevertheless, these simulations are adequate to demonstrate the impact of the variation of each parameter on the apparent permeability, compared to a reference case. Simulations are performed for part of the slip and transition flow regimes which are of main interest as far as shale production is concerned. The same boundary conditions as in Section 4.1.1 are imposed, except for the solid walls where the diffuse boundary condition is used, i.e. Eq. (2.8) for $\sigma = 1$.

In Fig. 4.6 the data points represent the raw data and not mean values, since only one geometry is simulated for every set of QSGS parameters. The slip-corrected permeability, obtained by fitting the numerical solution of the NSEs imposing the first-order velocity-slip boundary condition (2.12) at small Knudsen numbers to the first-

order of Kn, is also shown for comparison [21]. For low Kn numbers, the NSEs with FVBC are solved instead of the BGK equations to reduce the computational cost. The DVM method requires further refinement of the spatial grids in the early slip regime and thus, the NSEs are preferred.

Specifically, the reference Case 1 is a porous medium with $\epsilon = 0.7$, $c_d = 0.001$ and $AR = 1$ (see structure in Fig. 2.2c). The other three structures are generated by changing one of these parameters at a time. Firstly, for Case 2, the core distribution probability c_d is augmented ($c_d = 10c_{d_{ref}}$), then for Case 3 the porosity is decreased ($\epsilon = 0.7p_{ref}$), and finally a highly anisotropic structure ($AR = 1000AR_{ref}$) is generated for Case 4 (see structures in Figs. 2.2a, 2.2f and 2.2i respectively). Cases 4 and 5 share the same structure, however, for the former, pressure gradient is applied along the y direction (where $\tau \gg 1$), while for the latter, it is applied on the x direction (where $\tau \cong 1$).

As previously mentioned in Section 2.4, it is preferable to use the effective characteristic flow length, i.e. the average pore size, for the calculation of the effective Knudsen number. Thus utilising Eq. (2.19) the Kn^* used in the forthcoming analysis is calculated from Eq. (1.12). Furthermore, the equivalent slip factor (see Eq. (3.3)) is herein used.

The velocity distribution contour plots of the reference Case 1 in Fig. 4.7 give useful insight of the rarefaction effects. A first observation for large Kn^* numbers is that the flow is more uniformly distributed along more paths. Moreover, the dimensionless velocity in large pores is attenuated. At the same time, in many of the smaller pores, the dimensionless velocity is significantly enhanced due to the large velocity slip at the solid surfaces and Knudsen diffusion. Therefore, the difference of flow resistances for pores of different sizes tends to be eliminated and thus the flow becomes more uniform.

The graph in Fig. 4.6a indicates that, generally speaking, apparent permeability follows a similar trend as the intrinsic one, i.e. increase of c_d, decrease of porosity and increase of height to width ratio of the particles all lead to a drop of permeability. At the same time, $k_{\infty_1} > k_{\infty_5} > k_{\infty_2} > k_{\infty_3} > k_{\infty_4}$ and likewise $k_{a_1} > k_{a_5} > k_{a_2} > k_{a_3} > k_{a_4}$. However, for Cases 1 and 5, although $k_{\infty_1} > k_{\infty_5}$, $k_{a_1} > k_{a_5}$ is valid for low Kn^* numbers ($Kn \leq 0.1$), then the inequality changes.

On the other hand, Fig. 4.6b demonstrates a different tendency of the permeability enhancement (k_a/k_∞) in the regimes shown. In particular, for Case 2 the opposite trend is observed between permeability enhancement and apparent permeability, i.e. $k_{a_2}/k_{\infty_2} > k_{a_1}/k_{\infty_1}$ even though $k_{a_1} > k_{a_2}$. However, for Cases 3 and 4 the same trend is observed, i.e. $k_{a_1}/k_{\infty_1} > k_{a_3}/k_{\infty_3} > k_{a_4}/k_{\infty_4}$ while $k_{a_1} > k_{a_3} > k_{a_4}$. Finally, $k_{a_5}/k_{\infty_5} > k_{a_2}/k_{\infty_2} > k_{a_1}/k_{\infty_1}$ in the whole range of Kn numbers shown.

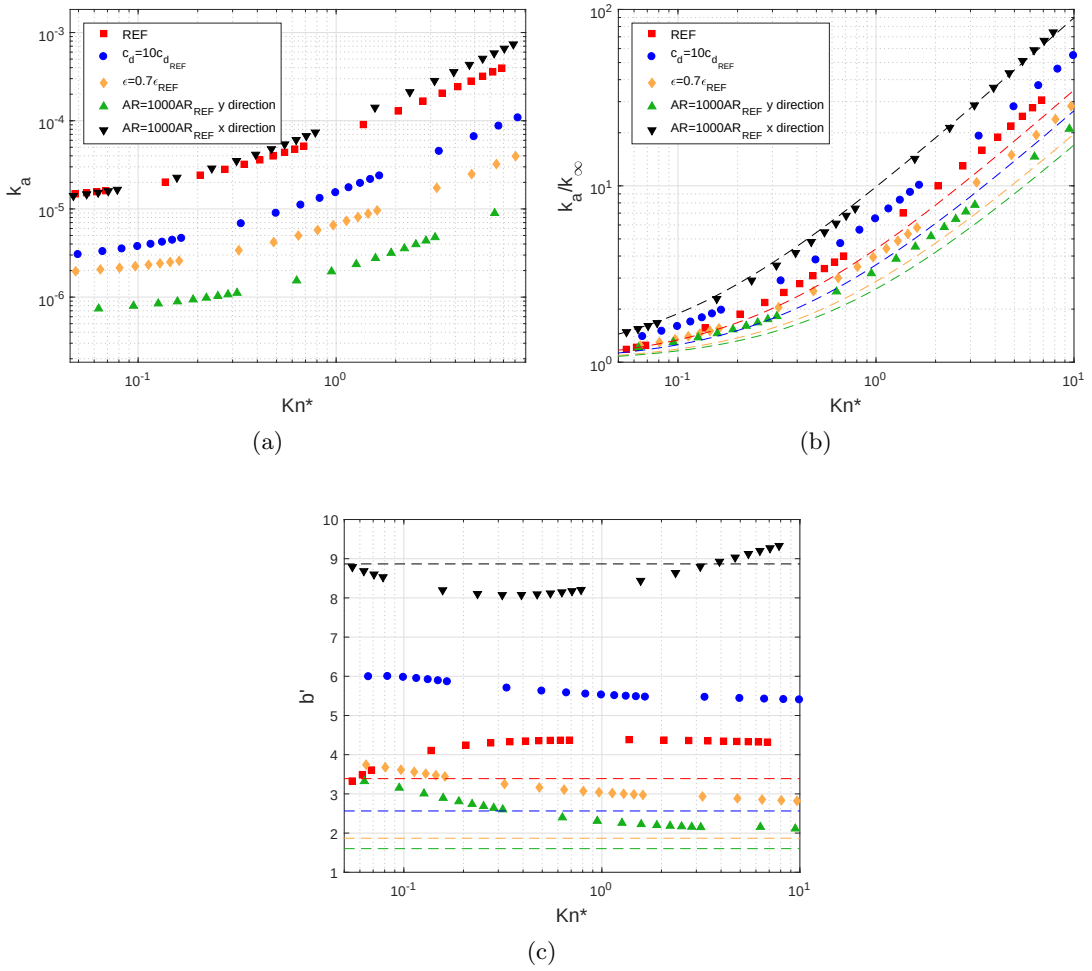

Figure 4.6: Numerical results of the DVM for (a) the apparent gas permeability, (b) the ratio of the apparent permeability to the intrinsic, and (c) the slip factor, as a function of the effective Knudsen number Kn^*. Case 1, taken as reference shown in red squares, corresponds to a structure with porosity $\epsilon = 0.7$, core distribution probability $c_d = 0.001$, and aspect ratio $AR = 1$. For Case 2 shown in blue circles, $c_d = 10c_{d_{ref}}$, while for Case 3, in yellow diamonds, $\epsilon = 0.7\epsilon_{ref}$. Finally, Cases 4 (in green upward-pointing triangle) and 5 (in black downward-pointing triangle) are the same structure having $AR = 1000AR_{ref}$ where the flow is in the y and x direction respectively. The dashed lines indicated with the same color as the corresponding cases are the slip-corrected permeability, derived from the numerical solution of the NSEs coupled with the FVBC. Note that the effective Kn number Kn^* is $69, 166, 162, 316, 78$ times of Kn for the Cases $1, 2, 3, 4, 5$, respectively.

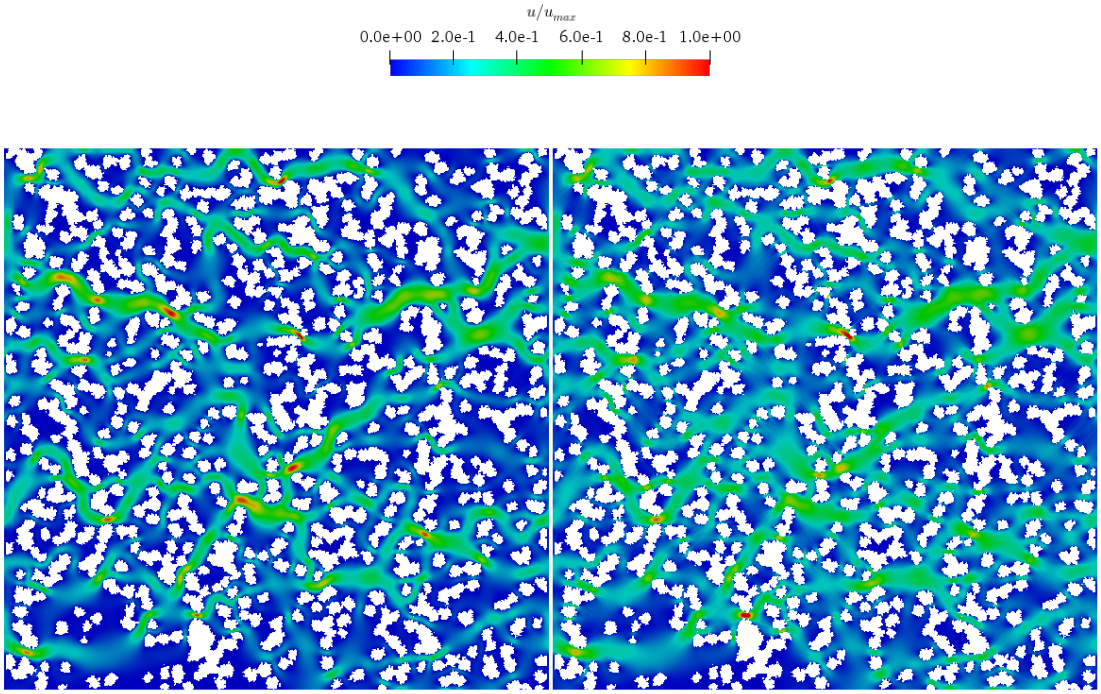

(a) $Kn^* = 0.007$ (b) $Kn^* = 0.7$

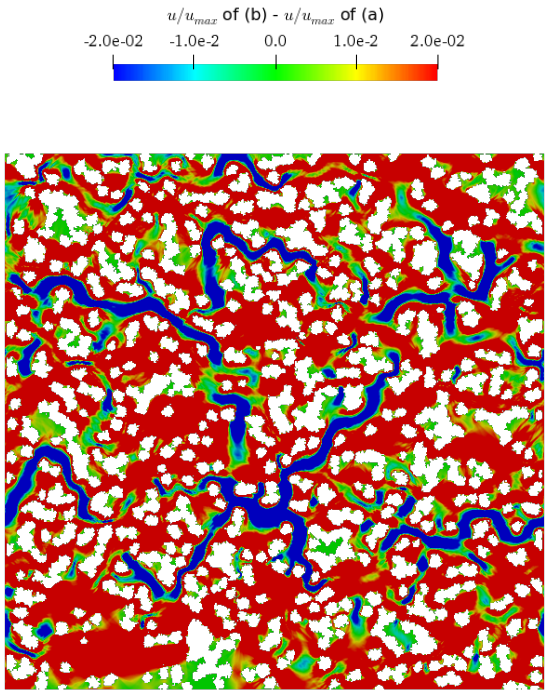

(c)

Figure 4.7: (a,b) Contour plots of the velocity magnitude normalised by its maximum value for Case 1. The flow on the right plot has a Kn^* number 100 times larger than the flow on the left. For larger Kn^* number, the flow in the biggest pores is attenuated while it is enhanced in the smaller ones. It can be observed, hence, that the increment of rarefaction leads to a more homogeneous distribution of velocity. In other words, the effect of the high resistance of small pores tends to be eliminated resulting in a more uniform flow behaviour. This can be confirmed in (c) where we realise that most of the flow contribution comes from the smaller pores due to high rarefaction, whereas the large pores contribute much less.

The slip-corrected permeability generally underestimates apparent permeability, with the exception of the low-tortuosity geometry (Case 5). Consequently it should only be considered as accurate for very low Kn^* numbers (in the early slip regime). In addition to that, the effect of permeability enhancement being higher when increasing c_d (i.e. the number of particles) for high Kn^* numbers is not captured under the continuum assumption.

Therefore, increasing the core distribution probability c_d leads to a boost of apparent permeability with a rate higher than of the rest three Cases $(1, 3, 4)$. This means that the smaller the particles' size for the same porosity (thus smaller pores), the more apparent permeability is favoured. Moreover, introduction of anisotropy, where the flow is in the direction of the particles' elongation and tortuosity is low, leads to greater permeability enhancement than all the other cases for all Kn^* numbers. This means that anisotropy not only favours apparent permeability compared to isotropic structures with the same nominal number of particles, but also compared to isotropic structures with smaller particles (Cases $1, 2$) respectively.

On the contrary, drop of porosity and introduction of anisotropy where the flow is in the direction perpendicular to the particles' elongation, generally reduce the slope of k_a. As far as porosity is concerned, based on the analytical solution Eq. (3.1) of [126], which is valid for high porosity porous media in the slip regime, k_a/k_∞ is expected to be higher for reduced porosities. The numerical results of DVM are in agreement with this tendency for $Kn^* \leq 0.07$. However, the numerical results of the NSEs coupled with FVBC do not confirm this. Additionally, for higher Kn^* DVM results drop of porosity has a negative effect on permeability enhancement. Therefore, this trend indicated by the analytical formula is generally not verified by the numerical simulations on the various QSGS geometries.

The variation of the equivalent slip factor b' with respect to Kn^*, as presented in Fig. 4.6(c), is quite different among the cases considered. The slip factor of geometries with high tortuosity, i.e. Cases $1-4$, tends to attenuate when Kn^* is high, while for Case 5 where tortuosity approaches unity b' initially drops, reaches a minimum and then rises in the free molecular flow regime. Again, slip-corrected permeability underestimates the slip factor for the tortuous cases, while it gives a good approximation for the least tortuous Case 5. It should be noted that the error of b' is more pronounced for low Kn^*, due to its derivation (see Eq. (3.5)), so possible shortcomings can affect severely the result of this specific variable in the slip regime.

In agreement with the relevant comments of the previous *chapter* in Section 3.2, again we observe that as $Kn \to \infty$ the slip factor either increases or reaches a plateau. However, for the complex porous media simulated in this *chapter*, the general behaviour

of b' varies significantly depending on the porous media properties. Even though the diffuse gas-surface boundary condition is applied for all these simulations, the slip-corrected expression which seemed to provide a good permeability approximation for the simplified porous media, here is close to the apparent permeability BGK results of only the low tortuosity Case 5. In addition to this, Klinkenberg's observation, that the slip factor decreases with Kn, is present in the simulation results of the porous media corresponding to Cases 2-5. Specifically, for Cases 2-4 b' is a decreasing function of Kn while Case 1 demonstrates a behaviour of the slip factor that resembles the one of the simple porous media of Section 3.2 for non-unitary TMAC. Consequently, Klinkenberg's findings can be observed in complex porous media without necessarily having diffuse-specular scattering. Nevertheless, it is concluded here that the agreement of the slip-corrected formulation with the simulation results is a coincidence and cannot be generalised even for unitary TMAC.

Finally, the classification of flow regimes, mentioned in Section 1.3 (see also Fig. 1.2), is based on pipe flow experiments and thus may vary for more complex geometries as emphasised by Beskok and Karniadakis [24]. For this reason, as expected, the behaviour related to each flow regime is observed at different Kn^* for each porous medium. Specifically, the range of Kn^* with linear dependence between Kn^* and k_a indicates that slip behaviour can be observed roughly for $Kn^* \leq 0.06$, $Kn^* \leq 0.02$, $Kn^* \leq 0.02$, $Kn^* \leq 0.03$, $Kn^* \leq 0.06$ for the Cases $1, 2, 3, 4, 5$ respectively.

4.2.2 Computational time

For the numerical computations performed in this *chapter*, the same workstations mentioned in Section 3.1.1 are used. The computational resources are, however, increased as follows. For the solution of the Boltzmann model equations 24 threads of the first workstation are utilised, whereas for the solution of the NSEs 4 threads are used on the second workstation.

The number of iterations and the simulation time for each of the cases mentioned in Section 4.2.1, for some of the Knudsen numbers tested, are reported in Table 4.2. Most of the observations of Section 3.1.1 for the rarefied flow simulations apply also here. To start with, the number of iterations required for the high-performance gas kinetic solver to converge are inversely proportional to the Knudsen number. The first and highest Kn simulated are exempted for the reasons explained before. I remind here that the molecular velocities are approximated by the 8×8 Gauss–Hermite quadrature when $Kn < 0.01$ and the Newton-Cotes quadrature with 22×22 non-uniform discrete velocity points for higher Kn. Therefore, the increased velocity space leads to an increase of the time required for each iteration to be performed. For example, for Case

1, an iteration takes approximately 3s when $Kn = 0.1$, while when $Kn = 0.01$ an iteration is performed in less than 0.5s. It is extremely difficult to correlate the number of required iterations or time depending on the porous medium properties due to the various factors influencing those parameters, such as Kn^*, porous medium complexity, number of fluid points, tortuosity etc.

For the continuum regime calculations, the computational mesh used is coarser, having half resolution. The convergence is achieved significantly faster, even though this is not a fair comparison considering the difference in resolution and computational resources utilised. Another observation is that, generally, the iterations and time required for the solution of both the NSEs and the Boltzmann model equations appear to be similarly affected by the change in porous media properties (Case 1 compared to Case 2 are exceptions).

4.2.3 Apparent permeability formulation

Similar to intrinsic permeability, apparent permeability could also be expressed as a function of the independent variables. Additionally, it is a function of Kn. It is well-documented that k_a is a linear function of Kn in the slip regime for the diffuse gas-solid interaction [21]. Considering a periodic array of circular discs, as in Section 4.1.2, the analytical formula (3.1) for the apparent gas permeability is a non-linear function of Kn [126]. Nevertheless, since the formula is based on the NSEs coupled with FVBC, its applicability is limited to the first-order of Kn. Therefore, by expanding the formula into a Taylor series around $Kn = 0$ and retaining up to the first-order terms, the accuracy is maintained for the slip regime [21]. This simplified expression, same as Eq. (3.2), is repeated here for the sake of completeness and reads

$$k_{a,c,slip} = k_{\infty,c} + 2A_1 Kn \frac{1}{8\pi}\sqrt{\frac{\pi}{P}}(1 - 2P + P^2), \tag{4.7}$$

where $A_1 = 1.15$ when the diffuse boundary condition is used, as in this study.

Dividing the above analytical formula by the factor $a_3 g AR^{a_4}\tau^2$, the first term turns into the general form of the intrinsic permeability $k_{\infty,random,an}$ (4.6). The term proportional to Kn needs to be adjusted accordingly, to incorporate the behaviour of the various QSGS structures in rarefied conditions, as explained in Section 4.2.1. For this reason, the factor $a_6 {c_d}^{a_7} AR^{a_8}$ is added. This yields

$$k_{a,random,an,slip} = k_{\infty,random,an} + 2A_1 Kn \frac{1}{8\pi}\sqrt{\frac{\pi}{P}}(1 - 2P + P^2)\frac{{a_6}' {c_d}^{a_7'} AR^{{a_8}'}}{a_3 g AR^{a_4}\tau^2}, \tag{4.8}$$

Table 4.2: Iteration steps and elapsed time for the numerical solution of the linearised BGK equation using the implicit discrete velocity method when $Kn > 0$ and for the numerical solution of the NSEs when $Kn = 0$. The time is measured by wall clock time. The porous media correspond to Cases 1-5 mentioned in Section 4.2.1. The mesh resolution is 1010×1000 for $Kn = 0$ and then double for $Kn > 0$. Note that the computational resources used for the BGK simulations are different than for the remaining runs.

Case 1: $\epsilon = 0.7$, $c_d = 0.001$, $AR = 1$

Kn	Kn^*	Iterations	Time (s)
10^0	69	6000	18.6×10^3
10^{-1}	6.9	3000	9.20×10^3
10^{-2}	0.69	9000	3.91×10^3
10^{-3}	0.069	11000	5.25×10^3
10^{-4}	0.0069	76000	37.0×10^3
0	0	6843	3.97×10^3

Case 2: $\epsilon = 0.7$, $c_d = 0.01$, $AR = 1$

Kn	Kn^*	Iterations	Time (s)
10^0	166	11000	31.1×10^3
10^{-1}	16.6	6000	21.9×10^3
10^{-2}	1.66	15000	6.60×10^3
10^{-3}	0.166	18000	7.71×10^3
10^{-4}	0.0166	53000	58.4×10^3
0	0	1089	0.73×10^3

Case 3: $\epsilon = 0.5$, $c_d = 0.001$, $AR = 1$

Kn	Kn^*	Iterations	Time (s)
10^0	162	49000	124×10^3
10^{-1}	16.2	24000	61.4×10^3
10^{-2}	1.62	81000	34.0×10^3
10^{-3}	0.162	101000	50.8×10^3
10^{-4}	0.0162	147000	73×10^3
0	0	5121	1.77×10^3

Case 4: $\epsilon = 0.7$, $c_d = 0.001$, $AR = 1000$

Kn	Kn^*	Iterations	Time (s)
10^0	316	47000	160×10^3
10^{-1}	31.6	16000	50.8×10^3
10^{-2}	3.16	84000	37.5×10^3
10^{-3}	0.316	88000	46.6×10^3
10^{-4}	0.0316	128000	57.2×10^3
0	0	373	0.24×10^3

Case 5: $\epsilon = 0.7$, $c_d = 0.001$, $AR = 1000$, $\tau \approxeq 1$

Kn	Kn^*	Iterations	Time (s)
10^0	78	31000	102×10^3
10^{-1}	7.8	19000	62.7×10^3
10^{-2}	0.78	44000	20.6×10^3
10^{-3}	0.078	82000	45×10^3
10^{-4}	0.0078	154000	86×10^3
0	0	321	0.20×10^3

$$\frac{k_{a,random,an,slip}}{k_{\infty,random,an}} = 1 + 2A_1 Kn^* \frac{1}{8\pi}\sqrt{\frac{\pi}{P}}(1 - 2P + P^2)\frac{a_6 {c_d}^{a_7} AR^{a_8}}{k_{\infty,c}}, \tag{4.9}$$

where $AR = 1$ for isotropic geometries. The fitting is performed considering that the above semi-analytical expression is expected to be most accurate for high porosities. The numerical data utilised are derived from the NSEs coupled with the FVBC. The fitted curves are identical to the ones resulting from the corresponding numerical results (dashed lines) in Fig. 4.6b except for the Case 3 which was not considered due to its low porosity.

It should be noted that intrinsic permeability given by the semi-analytical model is a sufficient approximation of the intrinsic permeability of the simulated structures, mainly due to the large amount of geometries tested. The fitting for the apparent permeability is thus performed based on this approximation, but not accurate value. Unlike the fitting for the intrinsic permeability in Section 4.1.2, the simulated structures are here fewer due to the high computational cost. It can be concluded then, that the coefficients of the formulae for estimation of apparent permeability can be considered less reliable in this context. Nevertheless, using the resulted coefficients, we acquire a good indication of the dependency of the slip factor on ϵ, c_d and AR in the slip regime. The values of the coefficients that gave a satisfactory fit are shown in Table 4.3.

Table 4.3: List of fitting coefficients for apparent permeability formulation Eq. (4.9).

Structure	Flow direction	a_1	a_2	a_3	a_4	a_5	a_6	a_7	a_8
Isotropic	any	2		0.7	-	-			-
Anisotropic	x	8.8	0.11	0.3	0.17	-0.48	0.26	-0.0091	0.113
	y	0.5			0.31	0.48			-0.113

4.3 Conclusions

In summary, the structural properties of porous media significantly affect not only intrinsic permeability, but also the slip factor appearing in apparent permeability, in different ways as analysed. This assertion is based on the numerical dataset produced from flow simulations of 400 geometries, generated using the QSGS method. These numerical results indicate that the slip factor can follow similar behaviour to the one observed by Klinkenberg in his experiments even for unitary TMAC. Additionally, the slip-corrected expression underestimates apparent permeability in the majority of the cases reported. These trends are not observed in the previous *chapter* where only simplified porous media are considered.

The above conclusions suggest that the use of permeability models based on over-simplifications of the complex porous media geometry, such as the consideration of the pores as straight tubes, gives misleading results. To address this issue, I presented a simple semi-analytical formulation to calculate intrinsic permeability (Eq. (4.6)). This formulation was also extended and revised to capture apparent permeability in the slip regime (Eq. (4.9)).

The proposed approach of permeability estimation is fast and efficient, since it does not entail numerical simulations or experimental measurements for the approximation of intrinsic and apparent gas permeability (in the slip regime). For the moment, this approximation is limited to 2D QSGS geometries. The physical features of real 3D porous media cannot be fully represented in such structures. Therefore, the validity of the current results and their extension in real porous media requires further investigation.

This study also highlights the uncertainties and challenges with regards to estimating the permeability of complex porous media through simplified formulae. Since random structures with the same nominal properties can have distinct permeabilities, the concept of a unified formulation is itself contradictory. However, the proposed models successfully capture the impact of the variation of morphological characteristics on permeability, giving indicative estimates and trends. Last but not least, these numerical results could also serve as benchmarking cases to assist modelling of rarefied gas flows in complex geometries.

Chapter 5

Upscaling techniques for shale gas flows

Due to the absence of visible pore connectivity and the substantial computational cost of large scale flow simulations, direct numerical simulation of shale gas flow is only feasible on high resolution images of small samples. Upscaling techniques are employed to extract the effective permeability of large samples up to the reservoir scale. In this *chapter*, some analytical upscaling methods are compared with the numerical solution of Darcy's law in Section 5.1. Later, in Section 5.2, the effective permeability of random porous media with and without fracture is computed numerically and the results are discussed. Finally, in Section 5.3, the use of the Brinkman equation for upscaling fractured porous media is studied, with a special focus on the concept of effective viscosity. The *chapter* concludes with final comments.

5.1 Analytical versus numerical upscaling methods

In this *section*, only two-dimensional isotropic porous media will be treated so flow needs to be considered only in one direction, the horizontal in this case. The boundary conditions applied for the numerical solution of the Darcy equation are fixed pressure at the inlet and outlet and no-flow at the lateral walls (imposing zero permeability).

The arithmetic, geometric and harmonic means provide simple estimates of the effective permeability values of heterogeneous systems. In general, the arithmetic and harmonic average give the upper and lower bound to k_{eff} respectively [133, 134]. Out of the three, the geometric average usually provides the closest k_{eff} approximation for a random isotropic permeability field. However, for large permeability variance/contrast

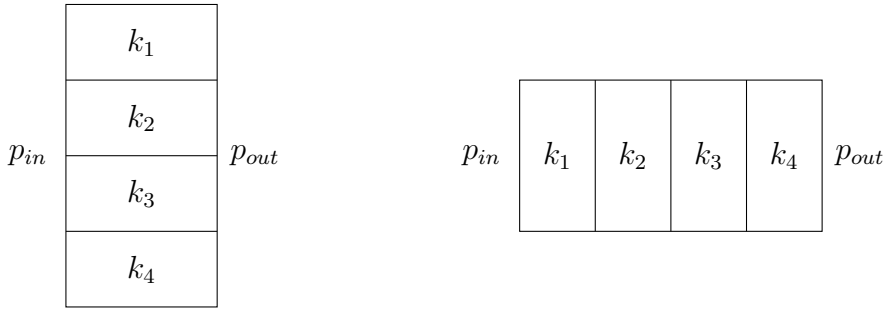

Figure 5.1: Schematic illustration of (left) parallel flow and (right) series flow for $n = 4$ cells. The effective permeability is the arithmetic mean and the harmonic mean respectively.

the use of more sophisticated methods is essential [135].

For flow in the horizontal direction, referred to as parallel flow (to the strata), the upscaled permeability is provided by the arithmetic mean of the permeability values k_i as follows (see Fig. 5.1)

$$k_{eff}^{A} = \frac{1}{n}\sum_{i=1}^{n} k_i, \tag{5.1}$$

considering that the n cells are of equal size as studied here. Flow in the vertical direction is referred to as series flow (perpendicular to the strata) and k_{eff} results from the harmonic mean (see Fig. 5.1)

$$k_{eff}^{H} = n\left(\sum_{i=1}^{n}\frac{1}{k_i}\right)^{-1}. \tag{5.2}$$

Finally, the most commonly used geometric mean which estimates the upscaled permeability of a spatially random permeability field is given by

$$k_{eff}^{G} = \left(\prod_{i=1}^{n} k_i\right)^{1/n}. \tag{5.3}$$

King [135] introduced an elegant analytical upscaling method to account for large (but not excessive) permeability fluctuations in heterogeneous porous media. The renormalization technique is a stepwise averaging procedure extensively used for upscaling petroleum reservoirs. In this technique, a block of permeabilities is replaced by an equivalent resistor network, following the analogy between a fluid flow through a porous medium and a current through an electric circuit. The process is developed upon a 2×2 block so for finer permeability fields it is repeatedly applied as many times as needed, leading to a coarser grid, until a single equivalent permeability is calculated

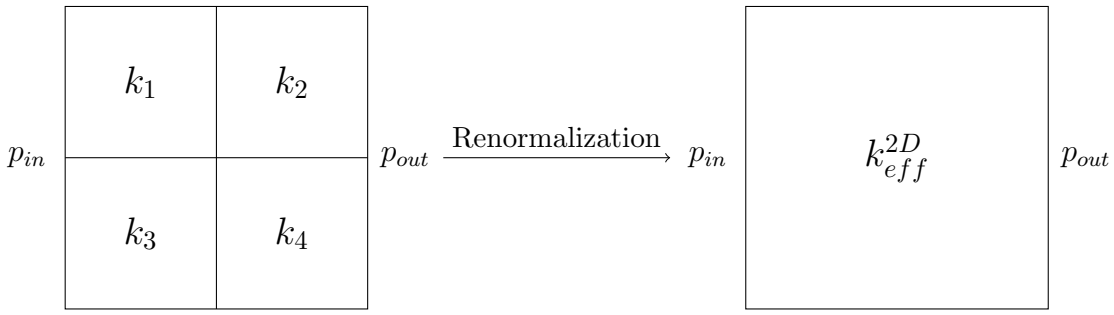

Figure 5.2: Schematic illustration of upscaling using the renormalization method of a two-dimensional 2×2 grid block.

[136].

For a 2×2 block of isotropic $2D$ cells with individual permeabilities k_1, k_2, k_3 and k_4 the effective permeability k_{eff}^{2D} using the renormalization method is given by the following analytical expression (see schematic in Fig. 5.2):

$$\begin{aligned} k_{eff}^{2D}(k_1,k_2,k_3,k_4) =& 4(k_1+k_3)(k_2+k_4)[k_1k_3(k_2+k_4)+k_2k_4(k_1+k_3)] \\ & \times \{(k_1+k_2+k_3+k_4)[k_1k_3(k_2+k_4)+k_2k_4(k_1+k_3)] \\ & + 3(k_1+k_2)(k_3+k_4)(k_1+k_3)(k_2+k_4)\}^{-1}, \end{aligned} \tag{5.4}$$

which is derived assuming that the inlet and outlet boundaries are at uniform pressure and the top and bottom ones are solid walls (permeameter configuration) [135]. It should be noted that this analytical expression is only valid for isotropic cells and that the presence of anisotropy does not lead to a closed form formula, but requires numerical implementation of the method. For 3D isotropic cases, a simple analytical expression based on the renormalization method was later proposed by [137] as follows

$$\begin{aligned} k_{eff}^{3D}(k_1,k_2,k_3,k_4,k_5,k_6,k_7,k_8) =& \frac{1}{4}\left[k_{eff}^{2D}(k_1,k_2,k_3,k_4)\right. \\ & + k_{eff}^{2D}(k_5,k_6,k_7,k_8) \\ & + k_{eff}^{2D}(k_5,k_6,k_1,k_2) \\ & \left. + k_{eff}^{2D}(k_7,k_8,k_3,k_4)\right], \end{aligned} \tag{5.5}$$

where the 8 block permeabilities and the 3D process are visualised in the schematic of Fig. 5.3.

The author of [135] claims that renormalization is accurate for most of cases, taking the Darcy solution as a reference, unless permeabilities are arranged in particular configurations. The sensitivity of the method according to the range of adjacent permeability values and their configuration is demonstrated in the examples of Table 5.1

Figure 5.3: Schematic illustration of upscaling using the renormalization method of a three-dimensional $2 \times 2 \times 2$ grid block. The hidden block has permeability k_8.

and Fig. 5.4. The effective permeabilities derived using the analytical upscaling methods of the geometric mean and renormalization are compared with the numerical result of the Darcy solver, which is taken as reference, for numerous 2×2 and 4×4 permeability blocks. In each case, four different permeability values k_i are used where the following colours indicate increasing value: blue, cyan, orange and red. This illustration facilitates the identification of the permeability contrasts and patterns.

To start with, in Table 5.1, seven different 2×2 permeability fields are examined. In Cases 1 and 2, the sequence of the permeabilities (pattern) is the same, however, the permeability variance is smaller for the former, leading to smaller deviations between the different upscaling methods as expected. The rest of the cases studied use the permeability values of Case 2 in various spatial arrangements. For the Cases 2 and 3 the two largest permeabilities are placed diagonally, so the deviation of the renormalization method is as high as 30% due to the singularity point (most of the flow is forced to go through the intersection of the four blocks, i.e. the center of the domain). For Cases 4 and 5, the two largest values are placed in the two upper and two left blocks respectively. This arrangement leads to closer k_{eff} values between the Darcy and the renormalization methods (10% difference) although the placement of the other two blocks is not advantageous for the flow since the lowest permeability is adjacent to the highest one. For instance, in Case 4 the flow meets less resistance from left to right on the upper part of the domain while the opposite happens for the lower part. Both configurations force part of the flow to move diagonally to avoid the block with the smallest permeability. Finally, Cases 6 and 7 demonstrate the best agreement between the numerically derived k_{eff} and the one obtained from Eq. (5.4). Despite the fact that the location of the highest permeability values is the same as in Cases 4 and 5, i.e. k_1, k_2 and k_1, k_3 respectively, the difference here is 0%. This is due to the arrangement of the other two permeability values which secure less severe permeability contrasts compared to the two previous cases. The preferential flow path for Case 6 is the two

Table 5.1: Upscaling permeability of a 2×2 block of isotropic cells (4! possible combinations without repetition). The permeabilities of the blocks in Case 1 have standard deviation equal to 1.11×10^{-10} while for the rest of the Cases the standard deviation is equal to 1.96×10^{-9}. For both sets of permeabilities the values are illustrated with blue, cyan, orange and red to show qualitative increase.

Case		Method	k_{eff}	Difference
1	2×10^{-10} 3×10^{-10} / 4×10^{-10} 1×10^{-10}	Darcy	2.26×10^{-10}	-
		Geometric	2.21×10^{-10}	-2%
		Renormalization	2.09×10^{-10}	-8%
2	5×10^{-10} 1×10^{-9} / 5×10^{-9} 1×10^{-10}	Darcy	7.12×10^{-10}	-
		Geometric	7.07×10^{-10}	-1%
		Renormalization	4.97×10^{-10}	-30%
3	1×10^{-10} 1×10^{-9} / 5×10^{-9} 5×10^{-10}	Darcy	9.01×10^{-10}	-
		Geometric	7.07×10^{-10}	-21%
		Renormalization	6.29×10^{-10}	-30%
4	1×10^{-9} 5×10^{-9} / 5×10^{-10} 1×10^{-10}	Darcy	10.7×10^{-10}	-
		Geometric	7.07×10^{-10}	-34%
		Renormalization	9.67×10^{-10}	-10%
5	5×10^{-9} 1×10^{-10} / 1×10^{-9} 5×10^{-10}	Darcy	5.05×10^{-10}	-
		Geometric	7.07×10^{-10}	40%
		Renormalization	4.55×10^{-10}	-10%
6	1×10^{-9} 5×10^{-9} / 1×10^{-10} 5×10^{-10}	Darcy	9.17×10^{-10}	-
		Geometric	7.07×10^{-10}	-23%
		Renormalization	9.17×10^{-10}	0%
7	1×10^{-9} 1×10^{-10} / 5×10^{-9} 5×10^{-10}	Darcy	5.45×10^{-10}	-
		Geometric	7.07×10^{-10}	30%
		Renormalization	5.45×10^{-10}	0%

upper blocks while for Case 7 it is the two lower ones.

The sensitivity of the renormalization method is further investigated in more complex configurations like the two 4×4 permeability fields depicted in Fig. 5.4. Each 4×4 fine-mesh grid is converted to a 2×2 coarse-mesh grid before a single permeability is acquired. This intermediate step is necessary when applying the renormalization method using Eq. (5.4) but not for the numerical solution of the Darcy equation. Cases 8 and

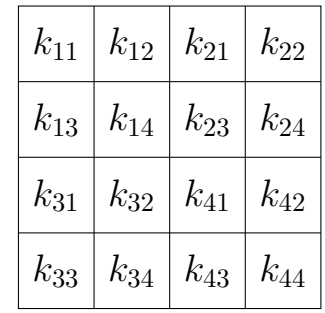

(a) Fine-scale grid

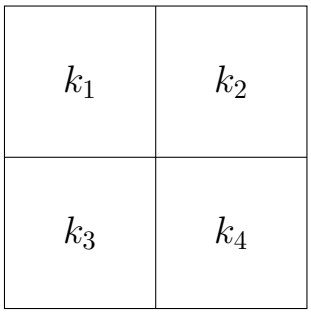

(b) Coarse-scale grid

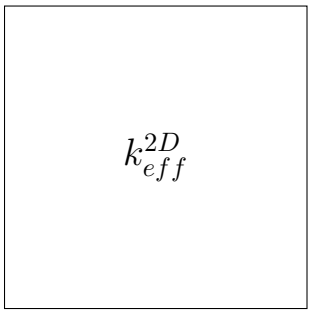

(c) Effective single grid

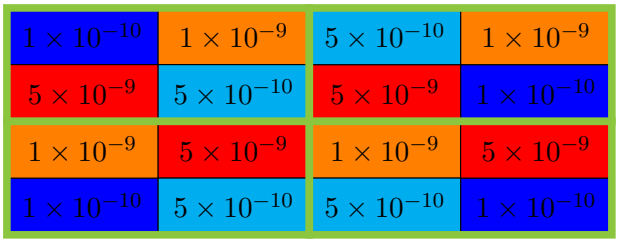

(d) Case 8: Fine-scale grid

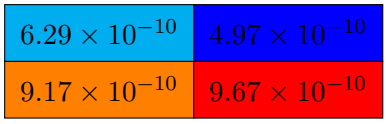

(e) Case 8: Coarse-scale grid

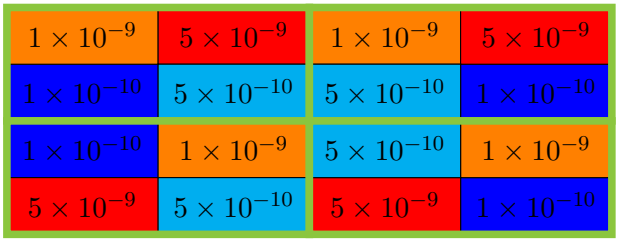

(f) Case 9: Fine-scale grid

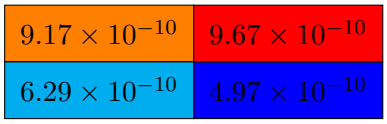

(g) Case 9: Coarse-scale grid

Figure 5.4: Upscaling permeability of a 4×4 block of isotropic cells using renormalization (two successive aggregations are needed). The resulting $k_{eff} = 7.49 \times 10^{-10}$ is the same for both Case 8 and 9. However, the numerical solution of the Darcy equation gives $k_{eff} = 1.08 \times 10^{-9}$ for the former Case and 8.41×10^{-10} for the latter.

9 are carefully constructed to demonstrate a weakness of the renormalization method. Observing the four blocks indicated by the green rectangles in Fig. 5.4(d) and (f), k_1 and k_2 of Fig. 5.4(d) become k_3 and k_4 of Fig. 5.4(f) and vice versa. In other words, the two upper blocks of the former coarse-scale grid become the two lower ones of the latter, see Fig. 5.4(b) and (d). This is expected to result in the same k_{eff} using the renormalization method due to the averaging process performed in a segregated manner. Nevertheless, carefully comparing the fine-scale grids of Cases 8 and 9, we see that at the boundaries of each coarse-scale cell, different permeability contrasts are encountered which affect the preferential paths of the flow. The spatial arrangement of permeabilities at the edges of each of the four blocks of the coarse-scale grid plays no

role for the renormalization method which provides equal values of $k_{eff} = 7.49 \times 10^{-10}$. Furthermore, the geometric mean gives $k_{eff} = 7.07 \times 10^{-10}$. On the other hand, the numerical solution of Darcy's law leads to effective permeabilities of 10.8×10^{-10} and 8.41×10^{-10} for Cases 8 and 9 respectively.

Since the aforementioned popular analytical upscaling techniques are problematic for several convoluted permeability configurations, it is worth investigating further numerical alternatives. Especially in permeability fields with high contrasts between neighbouring cells, such as in shales, it is suggested to upscale permeability employing Darcy's law [135] which is considered the most accurate upscaling technique [54, 134].

5.2 Hierarchical upscaling using the Darcy solver

Permeability upscaling from the pore-scale is herein performed numerically solving Darcy's law as explained in Section 2.2. For this *section*, the boundary conditions at the edges of the computational domain mimic the ones of the experimental permeameter (see Section 2.2.3). To demonstrate and investigate the potential of this method for permeability upscaling for some of the cases of interest, the permeability computed from the direct numerical simulation of the full sample is compared with the effective permeability computed using the following two-step technique.

- First, the full sample is divided in four sub-domains of equal size and the permeability tensor of each one, $\mathbf{k_i}$, is computed solving the Stokes equations twice (once per each of the main directions), as seen in Fig. 5.5.
- The 2×2 permeability field derived is utilised as input for the Darcy solver which gives k_{eff}.

Then, the accuracy of the calculated effective permeability, k_{eff} is evaluated comparing with the permeability of the initial full sample, k. The relative error of the permeability estimation is computed as follows

$$\eta = \frac{|k_{eff} - k|}{k} 100\%. \tag{5.6}$$

An automated process is developed to provide the permeability of each sub-domain. This entails the following steps: meshing, decomposition of the domain, setup of each simulation, solution of each flow direction, return of the sub-domain properties such as dimensions, porosity and full permeability tensor. Later, the effective permeability is obtained by solving the macro-scale problem, i.e. Darcy's equation. The permeabilities

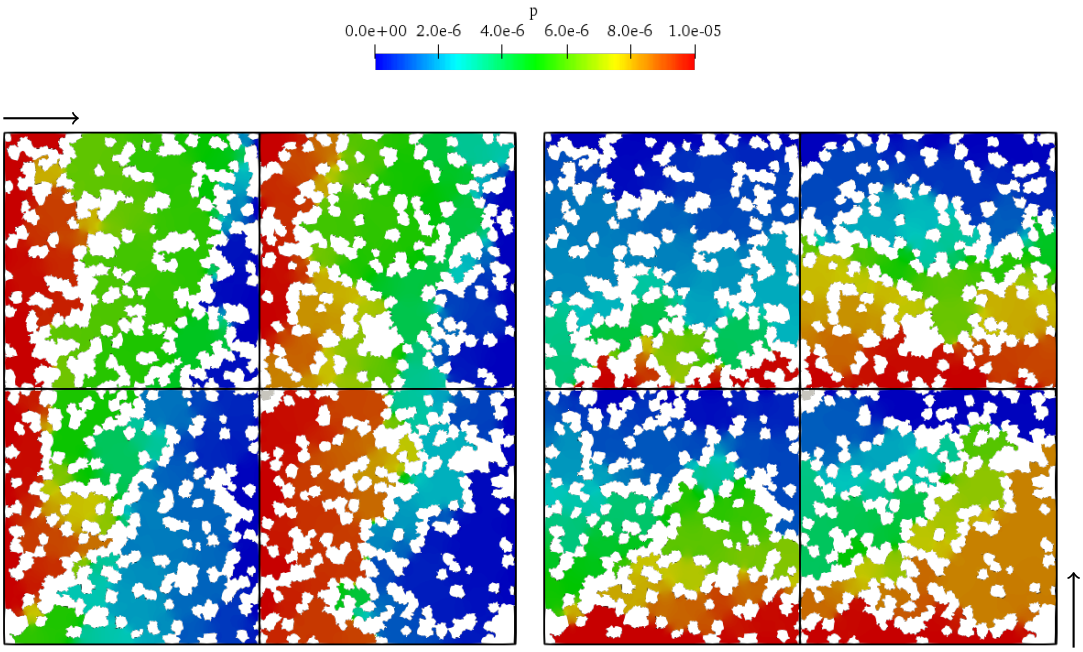

(a) (b)

Figure 5.5: Pressure contours of the sub-domain simulations performed applying $\mathrm{d}p/\mathrm{d}x$ and $\mathrm{d}p/\mathrm{d}y$ (the arrows indicate the flow direction). The intrinsic permeability tensor $\mathbf{k_i}$ of each sub-domain $i = 1, 2, 3, 4$ is obtained. The small grey area in the intersection of the sub-domains indicates the lost volume compared to the initial sample.

computed from the automated process constitute the permeability field of the macro-scale problem.

At this point, it is important to analyse the decomposition process applied. The native mesh decomposition tool of `OpenFOAM` is used, *decomposePar*, initially developed for parallel computation. The tool is set here to provide blocks of equal size. The different strategies that can be implemented are the following:

- Mesh the whole sample and then decompose it to the desired number of sub-domains.
- Decompose the sample to the desired number of sub-domains and then mesh them individually.

The first strategy is chosen since it is more straightforward and efficient. Both approaches result in the creation of unconnected pores at the boundaries of the sub-divisions which lead to lower total porosity of the porous material. In the approach used here the disconnected pore space is meshed and thus should be removed for the numerical solution to be performed. An automatic process is applied to detect and

remove these problematic areas, but on the same time evaluate their size. Note that when using the latter approach, the volume loss cannot be evaluated directly, since the unconnected pore-space is not meshed, but can be calculated from the comparison between the initial porosity and the sum of the porosities of the sub-domains.

A statistically isotropic 2D porous medium generated with $\epsilon = 0.7$ and $c_d = 0.001$ is decomposed in four equal sub-domains. The intrinsic permeability tensor $\mathbf{k_i}$ of each sub-domain $i = 1, 2, 3, 4$ is calculated by solving the Stokes equations for pressure driven flow as explained in Section 2.3. The pressure contour plots of each of the necessary simulations in the two main directions are shown in Fig. 5.5. The sub-domains are numbered as in the renormalization method, see Fig. 5.2. Note that the applied pressure gradient should be the same in the full and sub-domain simulations in order to maintain the mass flow, hence the pressure difference is reduced by half compared to the full domain simulation. The computed $\mathbf{k_i}$ of each sub-domain is then used as input for the Darcy simulation. The resulting effective permeability k_{eff} (diagonal element in the streamwise direction) is compared to the true permeability of the undivided original QSGS geometry k.

The same process is repeated for the same structure having a fracture that runs along its whole length. The fracture is extracted and adapted accordingly from an online database of images of porous micro-structures [138]. It is placed in two different positions, which lead to its allocation to separate sub-domains. In this way, it enhances the permeability k_i of the sub-domain it lays on (potentially, as explained in what follows). The velocity contours and permeability distributions of the aforementioned three configurations are shown in Fig. 5.6. The decomposition method results in a small loss of volume in the order of 0.1% (see grey area in the middle column of Fig. 5.6).

The hierarchical upscaling of the initial QSGS structure leads to a relative error, of 5.43%. The volume loss is negligible (0.1%) and cannot impact the effective permeability calculation significantly. On the other hand, comparing the velocity contours of Fig. 5.6(a) and (b) we observe that some of the main flow paths are eliminated due to the domain division, while some new ones are created. Inevitably, this fact affects the permeability tensor of each sub-domain, $\mathbf{k_i}$ (see Fig. 5.6(c)). The distribution of sub-domain permeabilities, reported in Fig. 5.7, indicates that they differ significantly. For example, the k_{xx} permeabilities are approximately between 6×10^{-6} and 15×10^{-6} with a standard deviation equal to 3.3×10^{-6}. This highlights that the sub-domain size is smaller than the Representative Elementary Volume (REV), i.e. the smallest volume of a porous medium for which the observed properties (such as porosity and permeability) are representative of the whole [139].

Nevertheless, the method does not seem to be sensitive to the sub-domain size, as

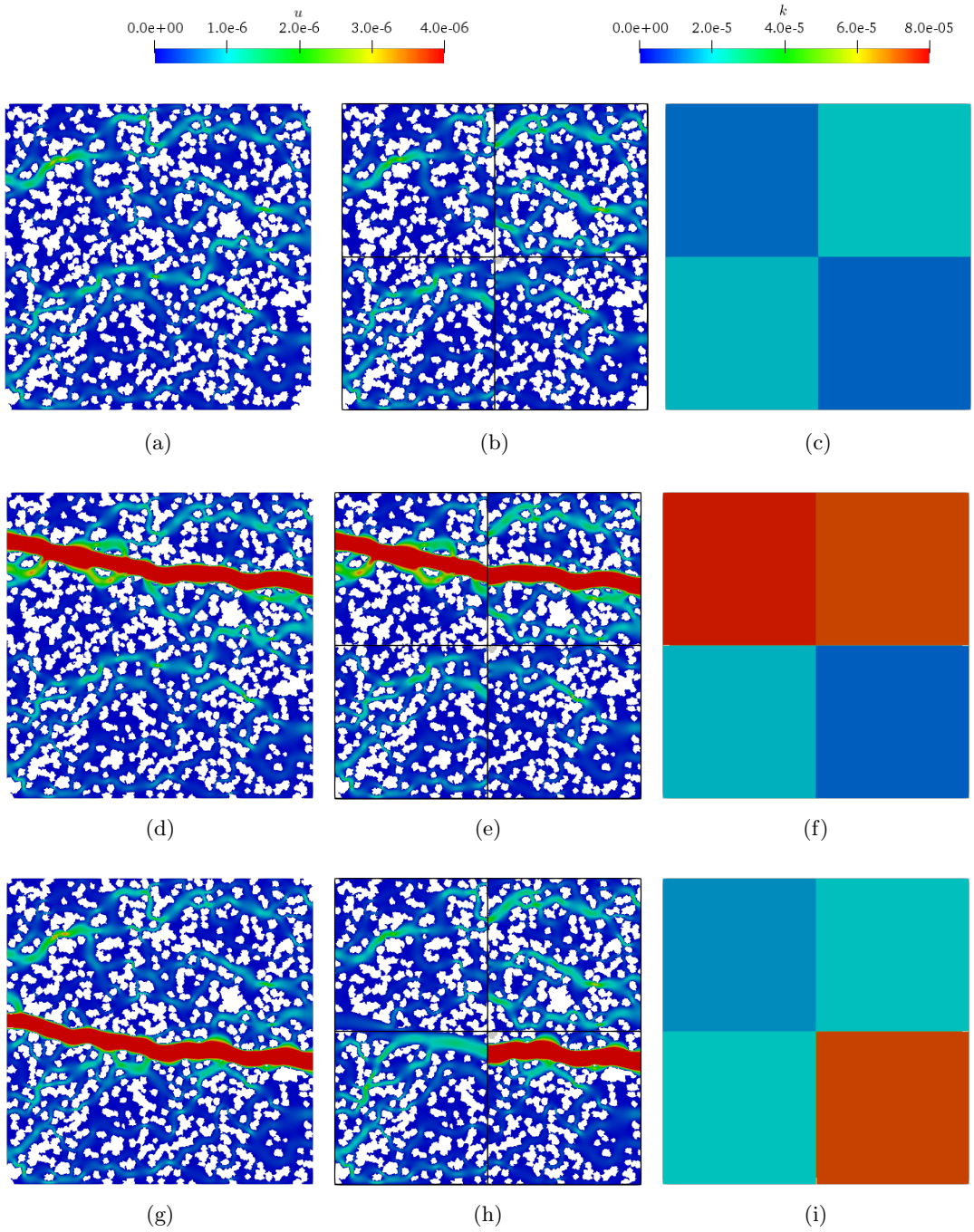

Figure 5.6: Hierarchical upscaling of the isotropic QSGS structure ($\epsilon = 0.7$ and $c_d = 0.001$) with (second and third row) and without a fracture (first row) for pressure driven flow from left to right. Visualisation of the velocity contours of the initial domain (first column), and of the four sub-domains (second column). The small grey area in the intersection of the sub-domains indicates the lost volume compared to the initial sample. Finally, the permeability field is shown, i.e. the magnitude of $\mathbf{k_i}$ for each sub-domain (third column).

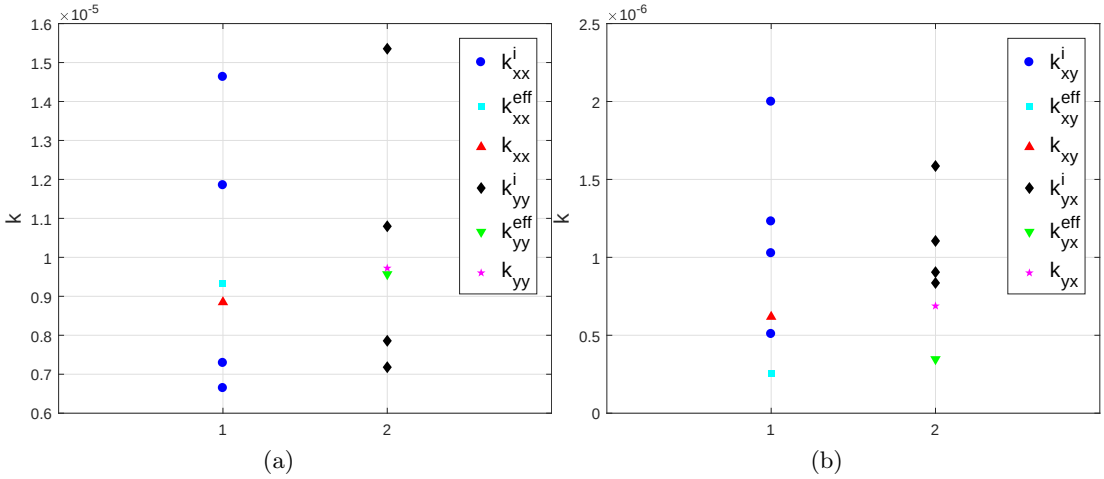

Figure 5.7: Permeability tensor components of the sub-domains which are illustrated in Fig. 5.5. The corresponding components of the full sample and of the effective permeability tensor are also depicted for comparison. The diagonal components are presented in (a) and the off-diagonal ones in (b).When the abscissa is 1 the components belong to the first row of the permeability tensor, while when the abscissa is 2, they belong to the second row.

emphasized by [140], since the resulting $\mathbf{k_{eff}}$ components are a close approximation of their $\mathbf{k}$ counterparts. Therefore, apart from the good accuracy, this method is advantageous since it enables the numerical evaluation of large digital rock images even using a desktop computer, due to the low memory requirements of the sub-domain simulations compared to the one of the initial sample. It should be noted that $\mathbf{k_{eff}}$ is reported here for the purpose of this comparison. In other parts of this thesis, only k_{eff}, which indicates the diagonal element in the horizontal direction, is reported.

The addition of a fracture and most importantly its position with respect to the domain decomposition can significantly affect the calculation of the effective permeability using the hierarchical upscaling method. It is widely known that fractures enhance the overall permeability and constitute the main flow paths in low permeability porous media. As seen in Fig. 5.6(d) and (e) the fracture is assigned to the two upper sub-domains and the velocity contours of the initial porous medium and its blocks are very similar. Thus, as expected, the predicted permeability has a very small relative error, i.e. $\eta = 0.6\%$ owing to the advantageous fracture decomposition. Conversely, in Fig. 5.6(g) and (h) the detrimental effect of a disadvantageous fracture division is shown. The left half of the fracture is assigned to two neighbouring blocks, in a way that its corresponding parts do not run along the streamwise direction; becoming dead-end pores. As a consequence, the computed permeability of these sub-domains is severely

underestimated, as seen in Fig. 5.6(i), leading to $\eta = 56.19\%$.

This analysis provides an understanding into the challenges of incorporating fractures in the upscaling process starting from the pore-scale. First, the sub-domain boundaries should be carefully selected taking into account the morphology of the fractures. Additionally, instead of using a Darcy solver, a hybrid upscaling method is more appropriate in treating porous media with fractures, especially when their size is fairly greater than the average pore size. For smaller factors of heterogeneity and anisotropy the method of upscaling presented in this *section* provides an accurate prediction of the effective permeability as marked in [140]. Even though increasing heterogeneity and anisotropy increases the error of the method, the approximation of k_{eff} is adequately accurate.

5.3 On the effective viscosity of the Brinkman model

As previously mentioned in Section 1.5, the momentum transport between porous and free flow regions in low-Reynolds number flows can be expressed by the Brinkman equation. The controversial matter of the effective viscosity μ_{eff}, which is present in this equation, has been extensively investigated, however, consensus has not been reached yet regarding its form or value.

In this *section*, a few basic alternatives regarding the value of effective viscosity are investigated and the option of a variable permeability model across the transition zone is examined. For this study, the experimental setup of Beavers & Joseph [75] (fully-developed, steady, quasi-one-dimensional flow process) is replicated, herein employing random two-dimensional porous media generated with the QSGS method. The domain consists of a rectangular channel of variable width H which is placed over a porous block of fixed size L, as demonstrated in Fig. 2.3b. The boundary conditions employed in this *section* mimic the ones of the experimental permeameter as explained in Section 2.2.3. In various papers focusing on the interfacial boundary condition and/or the Brinkman model, the issue of the choice of the interfacial location between the porous and the plain regions is highlighted [82, 141]. In this thesis, the nominal interface is chosen to be the surface tangent to the outermost pore perimeter [75, 82], see Fig. 2.3b.

Firstly, I carry out independent calculations to obtain the permeability tensor $\mathbf{k}$ of the selected porous medium as explained in detail in Section 2.3. I later use this $\mathbf{k}$ as input for the Brinkman model (which is modified appropriately), obtaining the effective permeability (coarse-scale) k_{eff}^{C}. In parallel, I perform simulations of the same configuration using the exact geometry of the matrix. In this way, the fine-scale permeability k_{eff}^{F} is obtained through direct simulations and the accuracy of the

Brinkman model is then evaluated. The relative error of the effective permeability estimation is defined as

$$\eta = \frac{|k_{eff}^F - k_{eff}^C|}{|k_{eff}^F|} 100\%. \tag{5.7}$$

The quasi-one-dimensional (even though the full permeability tensor is used as input) Brinkman results are compared to the ones of the direct simulation in an attempt to evaluate various model variations. To achieve this, the volume-averaged streamwise velocity profiles are employed to visualise the differences of the microscopic and macroscopic solutions. In most of the following figures, the depicted profiles are zoomed in to cover mainly the transition zone and the free flow region, since the deviation of the different approaches is mostly observed there. The thickness of the transition zone is typically expected to be equivalent to the size of a few pores, in the order of $\sqrt{k}$ [76, 82, 141].

To begin with, the flow through a statistically isotropic porous medium with $\epsilon = 0.7$ and $c_d = 0.001$ (see Fig. 2.2e), having a fracture of $H = 0.05L$ on top is studied. The results are illustrated in Fig. 5.8. The common values of effective viscosity $\mu_{eff} = \mu$ [60] and $\mu_{eff} = \mu/\epsilon$ [80] are employed, as well as the heuristic value of $\mu_{eff} = 3\mu/\epsilon$ which was found to provide the most accurate interfacial tangential/slip velocity (see Section 1.5). It is worthwhile to note that when using effective viscosity of the form: $\mu_{eff} = c\mu/\epsilon$ (where c is an adjustable parameter), since the porosity of the fracture is unity, the original fluid viscosity is automatically applied in the free flow region, as required. Observing the volume-averaged velocity profile derived from the direct simulation, we confirm that at $y \approx 20$ velocity starts to increase significantly, indicating thus the size of the viscous transition zone, see inset figure of Fig. 5.8a. This point where the viscous term starts to become negligible (as we approach the bulk of the porous medium) is herein referred as y_l, indicating the lower boundary of the transition zone. Employing the original Brinkman model with $\mu_{eff} = \mu$ and comparing it with the Stokes solution, the relative difference between the effective permeabilities is about 14%. The $\mu_{eff} = \mu/\epsilon$ performs slightly better resulting in a discrepancy of 12%.

Using this visualisation for better understanding, we realise that the main source of error is the underestimation of velocity in the transition zone which affects slip velocity (at the interface) and thus the flow through the fracture. Through a trial and error process, the use of the effective viscosity $\mu_{eff} = 3\mu/\epsilon$ in the Brinkman model is found to provide an interfacial tangential (slip) velocity close to the one of the direct simulation. As expected, the error of the Brinkman model is now reduced to 5%. Nevertheless, it is not eliminated due to the remaining discrepancy in the porous region. The results also highlight that increasing μ_{eff} the viscous shear effects penetrate further into the

porous medium, eventually creating an inter-region of size similar to the one derived from the direct simulation, for $\mu_{eff} = 3\mu/\epsilon$.

Increasing the fracture size to $H = 0.1L$ leads to a decrease of all three errors reported previously. This is due to the fact that increasing the gap size, the contribution of the porous medium to the total flow tends to become negligible. The velocity at the interface is enhanced and the viscous effects become more important above the transition zone. Generally speaking, the viscous term of the Brinkman equation (1.23) plays no major role at the main porous region/bulk (except the transition zone). In fact, it is almost zero, thus the use of different values of effective viscosity has an impact only in the transition zone (see Fig. 5.8b, all dashed lines merging at the bottom of the transition zone).

5.3.1 Variable permeability model

The different values of effective viscosity practically allow for the variation of velocity near the interface. However, taking μ_{eff} as an adjustable coefficient conveniently chosen to match the direct simulation results is not of practical interest. Observing the behaviour of a constant μ_{eff} we conclude that although the right interfacial velocity might be predicted, generally, the velocity profile in the inter-region is less accurate. To overcome this shortcoming, the concept of variable effective properties, e.g. permeability, viscosity and porosity, has been suggested in the literature [82, 142, 143]. In this thesis, my study is limited to the position-dependent permeability model. Intuitively, we expect permeability to be higher at the transition zone, since the permeable material exhibits lower resistance to the flow there, compared to its bulk region. It is emphasized that for simplicity, due to the nature of the flow (quasi-one-dimensional), only the horizontal (streamwise) diagonal permeability component k_{xx} is position-dependent in the vertical direction (i.e. the y-direction).

To begin with, $k_{xx}(y_{tr})$ where y_{tr} is in the transition zone, is obtained using the direct simulation data (computed velocity field). For the same porous medium and for channel of thickness $H = 0.05L$ the permeability in the transition zone, $0 \leq y_{tr} \leq 20$, can be fitted into an exponential function, i.e. $a\exp(by_{tr}) + c$. The three constraints that need to be satisfied in order to provide the three constants are:

1. k_{xx} at the interface ($y = 0$) should be equal to the one from the direct simulation,
2. k_{xx} at the lower end of the transition zone, y_l, (where the inertial effects are almost eliminated) should be equal to the one of the bulk of the porous medium,
3. the other constant can be obtained using the permeability of any intermediate location of the transition zone, e.g. its middle point.

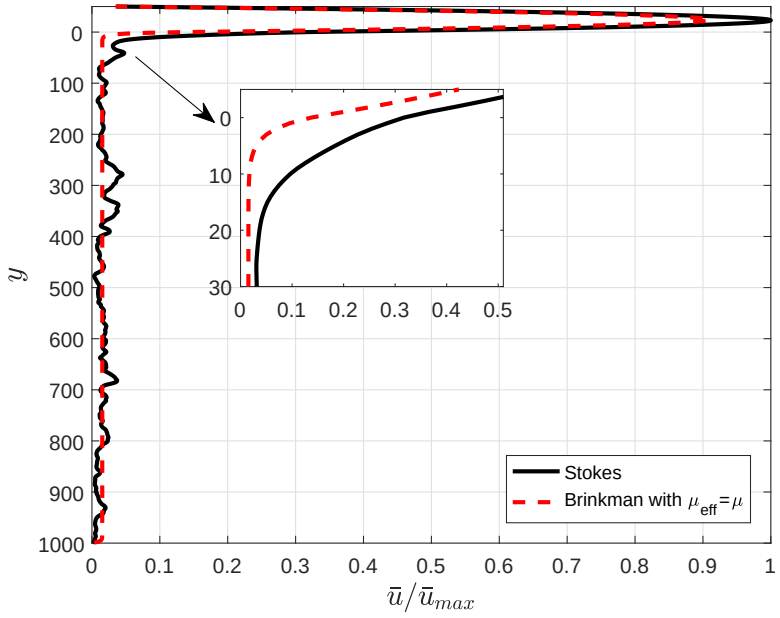

(a)

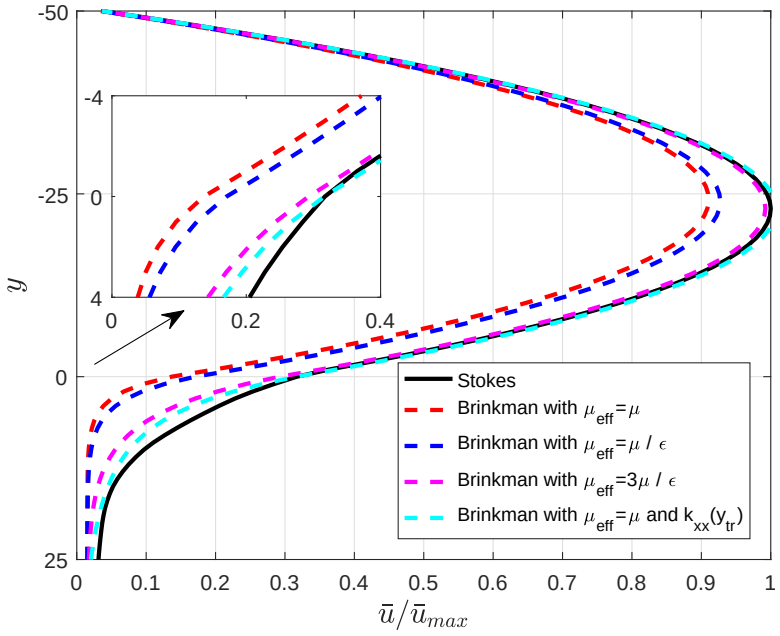

(b)

Figure 5.8: Profiles of the normalised streamwise-averaged velocity for the isotropic porous structure of Fig. 2.2e. A fracture of thickness $H = 0.05L$ is placed on top of the porous medium and their common interface is at $y = 0$. (top) The Stokes and Brinkman results are compared across the whole height of the domain, while the transition zone ($0 \lesssim y_{tr} \lesssim 20$) is better depicted in the zoomed inset figure. (bottom) The impact of the different μ_{eff} values is visualised, along with the results of the Brinkman simulation where a variable permeability (obtained from the corresponding Stokes data) is used along the transition zone.

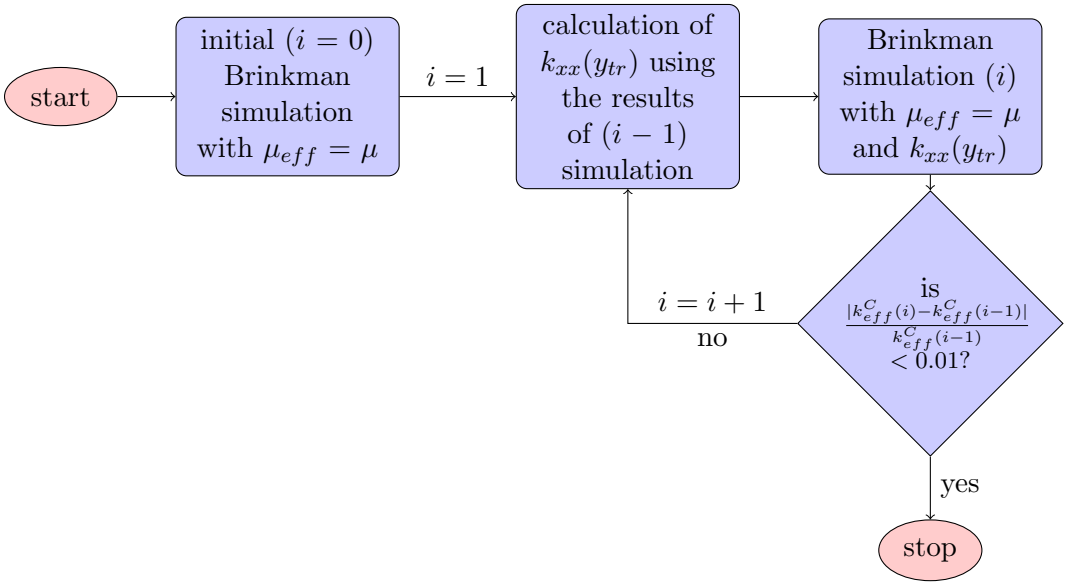

Figure 5.9: Flow chart of the iterative process/algorithm of permeability correction at the vicinity of the fluid-porous interface. The number of iterations is i.

The effective viscosity is taken equal to fluid viscosity, while permeability at the bulk of the porous medium remains unchanged; it is enhanced only at the boundary layer. The results for this reference case indicate a good agreement between the macroscopic and microscopic solutions, giving a negligible (0.4%) error as shown in Fig. 5.8b. Even though the use of this method and the use of the constant $\mu_{eff} = 3\mu/\epsilon$ lead to almost identical values of slip velocity (see $(\bar{u}/\bar{u}_{max})|_{y=0}$), the Brinkman solution with $\mu_{eff} = \mu$ and $k_{xx}(y_{tr})$ results in higher velocities at the transition zone, leading to increased accuracy. However, a drawback to using this approach is that it requires a priori knowledge of the direct simulation solution in order to correct permeability at the inter-region.

Iterative correction of the variable permeability

To circumvent this shortcoming, permeability is herein corrected using an iterative process fed with the solution of the previous Brinkman simulation. The algorithm introduced here can be described as follows (see also flowchart in Fig. 5.9):

1. The numerical solution of the Brinkman equation with $\mu_{eff} = \mu$ is performed.
2. The $k_{xx}(y_{tr})$ of the transition zone is computed, where the transition zone is defined by the nominal interface $y = 0$ and y_l,where $k_{xx}|_{y_l} = 1.01 k_{xx}|_{\text{porous bulk}}$.
3. k_{xx} of the transition zone is replaced by the result of Step 2.

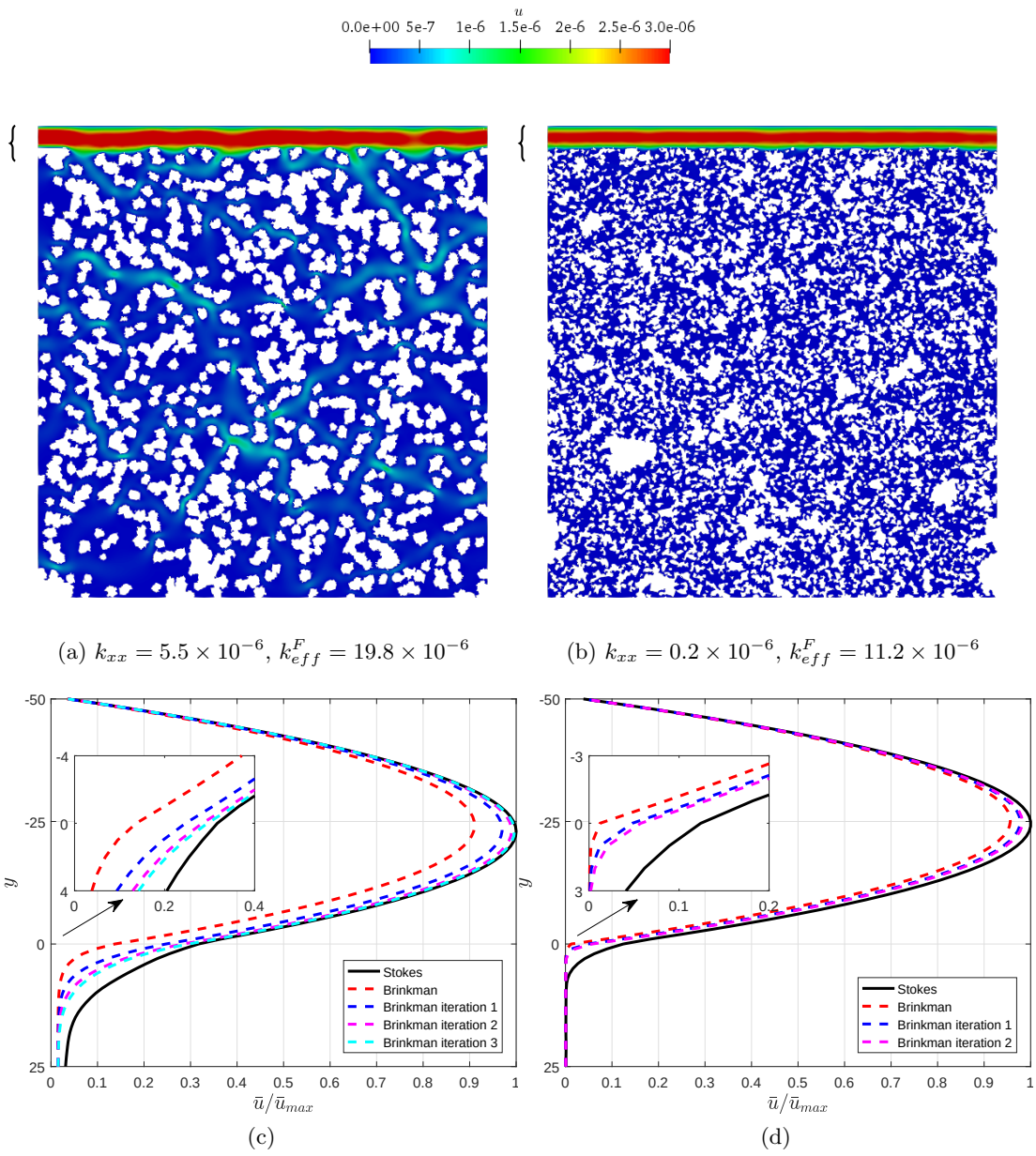

(a) $k_{xx} = 5.5 \times 10^{-6}$, $k^F_{eff} = 19.8 \times 10^{-6}$

(b) $k_{xx} = 0.2 \times 10^{-6}$, $k^F_{eff} = 11.2 \times 10^{-6}$

(c)

(d)

Figure 5.10: Velocity contour plots from the Stokes simulations (first row) and normalised velocity profiles from the Stokes and Brinkman simulations (second row). The normalised velocity profiles focus on upper part of the domain as indicated by the brackets in the first row. The fracture size on top of the porous medium is $H = 0.05L$ (interface is at $y = 0$). The isotropic porous media have $\epsilon = 0.7$, $c_d = 0.001$ (first column) and $\epsilon = 0.7$, $c_d = 0.01$ (second column). The iterative scheme is applied to correct the streamwise diagonal permeability value of the transition zone, $k_{xx}(y_{tr})$, using data from the previous Brinkman run.

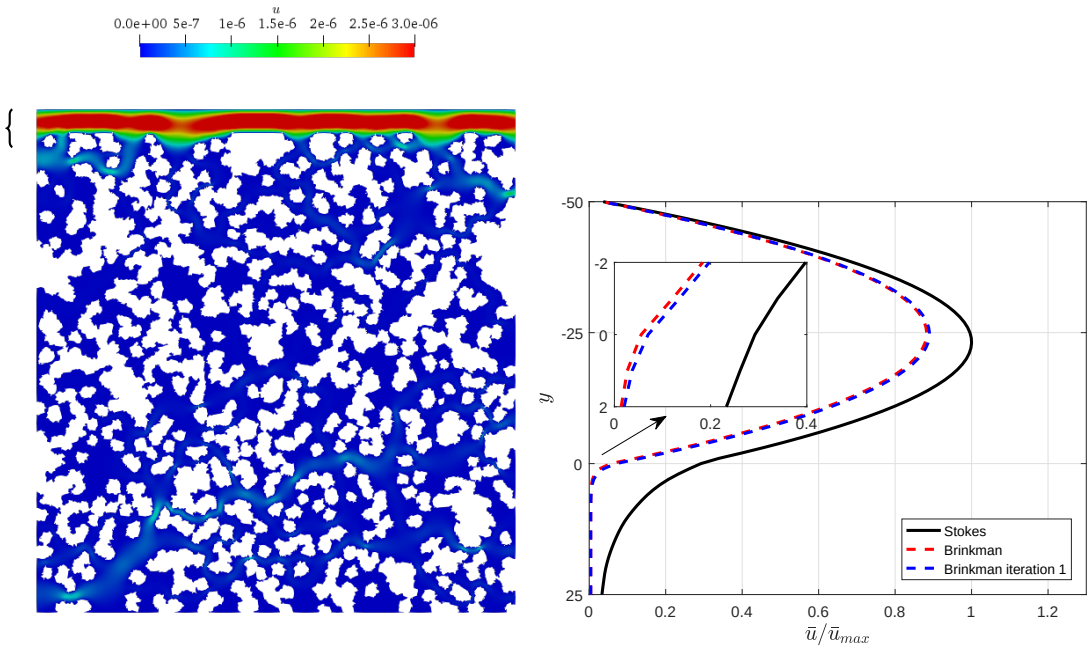

(a) $k_{xx} = 1.8 \times 10^{-6}$, $k^F_{eff} = 15.7 \times 10^{-6}$ (b)

Figure 5.11: Velocity contour plots from the Stokes simulations (left) and normalised velocity profiles from the Stokes and Brinkman simulations (right). The normalised velocity profiles focus on upper part of the domain as indicated by the brackets in the first row. The fracture size on top of the porous medium is $H = 0.05L$ (interface is at $y = 0$). The isotropic porous medium has $\epsilon = 0.6$ and $c_d = 0.001$. The iterative scheme is applied to correct the streamwise diagonal permeability value of the transition zone, $k_{xx}(y_{tr})$, using data from the previous Brinkman run.

4. The Brinkman simulation is again performed having all other parameters unchanged.

5. Steps 2-4 are repeated until the termination criterion is met; in this case, when the mass flow at the channel changes by less than 1% compared to the previous iteration.

This iterative process is herein applied in a few porous media with a fracture size of $H = 0.05L$ as before. To begin with, I focus on two isotropic porous media with $\epsilon = 0.7$, $c_d = 0.001$ and 0.01 respectively; the corresponding results can be found in Fig. 5.10. For the former porous medium, the error for the first Brinkman run is 14.4%. The error for each consecutive iteration is reduced to 8.4%, 6.1% and 5.3%. As in the case of the variable permeability, $k_{xx}(y_{tr})$, that resulted from the direct solution, each Brinkman numerical simulation that has $k_{xx}(y_{tr})$ as input, results in having a larger transition zone than the previous iteration. Thus, the local permeability also grows until convergence

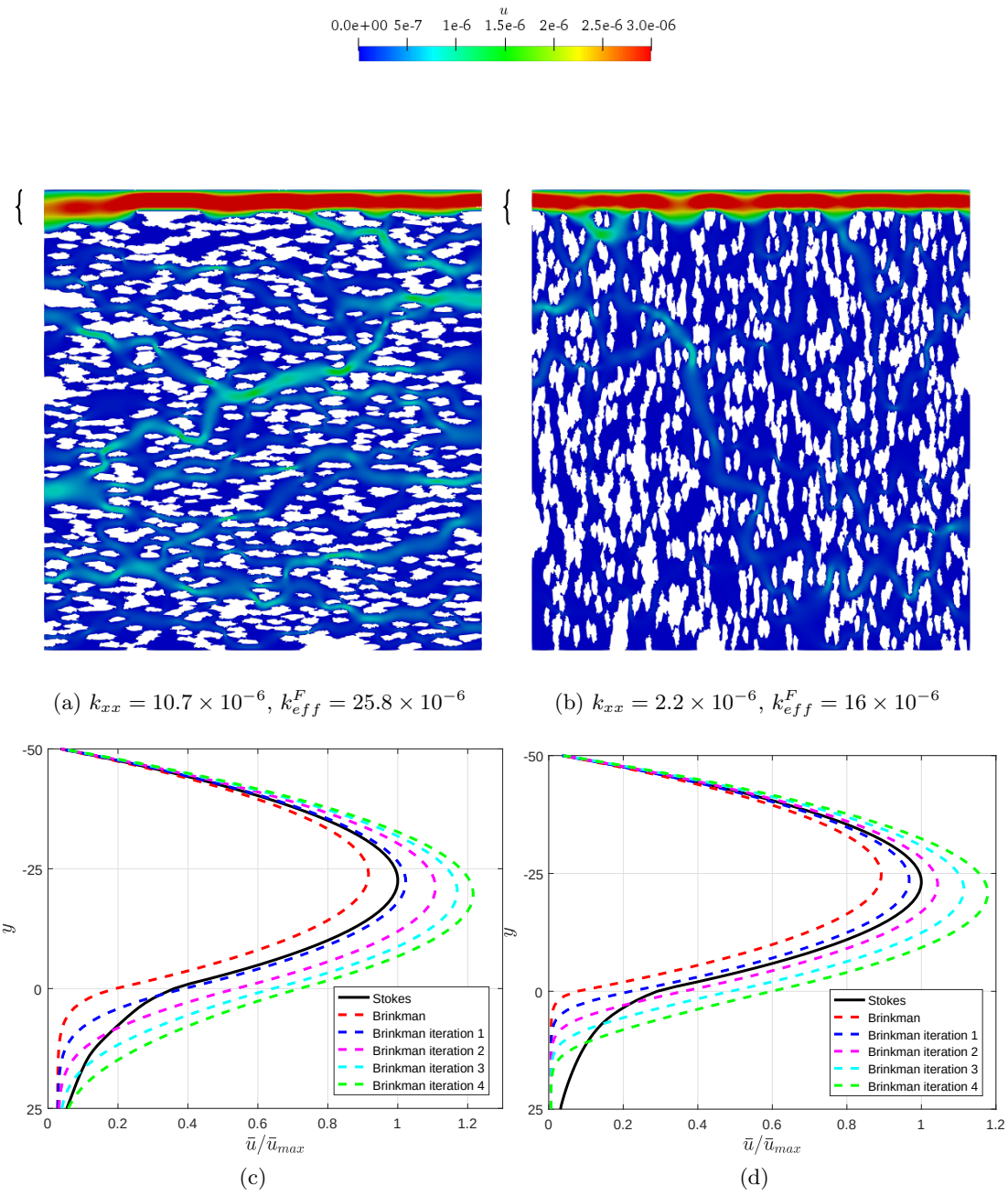

(a) $k_{xx} = 10.7 \times 10^{-6}$, $k^F_{eff} = 25.8 \times 10^{-6}$

(b) $k_{xx} = 2.2 \times 10^{-6}$, $k^F_{eff} = 16 \times 10^{-6}$

(c)

(d)

Figure 5.12: Velocity contour plots from the Stokes simulations (first row) and normalised velocity profiles from the Stokes and Brinkman simulations (second row). The normalised velocity profiles focus on upper part of the domain as indicated by the brackets in the first row. The fracture size on top of the porous medium is $H = 0.05L$ (interface is at $y = 0$). The anisotropic porous medium has $\epsilon = 0.7$, $c_d = 0.001$ and $AR = 100$. The same porous medium is used in both columns, however for the second one it is rotated by 90^o. The iterative scheme is applied to correct the streamwise diagonal permeability value of the transition zone, $k_{xx}(y_{tr})$, using data from the previous Brinkman run.

is achieved. For the latter porous medium, of a smaller particle size, the initial error of the Brinkman simulation is 7.4%. The next runs with corrected permeability at the transition zone lead to an error of 4.5% and 3.8%. A porous medium with a smaller porosity, $\epsilon = 0.6$ and $c_d = 0.001$ is then tested (see Fig. 5.11). In this case, the iterative process is unfruitful since the error of the effective permeability (23%) changes by less that 0.1%. For the above isotropic cases, the iterative process often converges after less than 3 iterations (solutions of the Brinkman equation).

Finally, an anisotropic porous medium with $\epsilon = 0.7$, $c_d = 0.001$ and $AR = 100$ is studied. The porous medium is first simulated applying pressure gradient in the same direction as the largest diagonal permeability, i.e. flow along the bedding plane, where $\tau \approx 1$ ($\eta = 14\%$). Afterwards, it is rotated by 90^o, where the diagonal permeability is the smallest, i.e flow perpendicular to the bedding plane, and $\tau \gg 1$ ($\eta = 18\%$). In both cases, the algorithm unfortunately diverges as shown in Fig. 5.12.

5.4 Conclusions

Some analytical upscaling techniques that are commonly used in reservoir engineering, are herein compared with the numerical solution of the Darcy equation. The analytical methods exhibit inferior sensitivity to changes in the permeability field and to high permeability contrasts, as those encountered in shales. Therefore, numerical upscaling methods are employed in the rest of this study.

Specifically, the accuracy of the effective permeability derived from the Darcy solver is successfully evaluated for some porous media of interest, taking the corresponding direct simulation solution as a reference. However, when fractures are added in the porous medium, the need for a hybrid model that can handle the separation of scales is evident. For this reason, the Brinkman model is particularly investigated.

Regarding the Brinkman equation, I focus on the impact of the transition zone flow velocity on the calculated effective permeability, and thus the accuracy of the model. Choosing alternative values of effective viscosity to conveniently match the expected results can lead to more accurate k_{eff} estimation. However, this method is of no practical interest since the direct simulation results are not always available.

The concept of μ_{eff} can be replaced by the notion that the permeability of the porous medium near the fluid-porous interface is enhanced. This computed local permeability when used as input for the next Brinkman simulation gives promising results. Undoubtedly, this iterative correction of the transition zone permeability offers better agreement of the Brinkman model with the Stokes results, when statistically isotropic porous media are considered. However, one disadvantage of this method is that it

does not always lead to significant improvement of the accuracy, depending on the porous medium properties. Additionally, for the tested anisotropic porous medium, the algorithm diverges, giving larger error than the initial estimation of the Brinkman model.

In the absence of a suitable universal effective viscosity or velocity correction process in the transition zone, for the random porous media of interest, the relationship $\mu_{eff} = \mu$ is retained in the rest of this thesis (as suggested by [70] for complex porous media).

Chapter 6

Upscaling pore-scale shale permeability

The effective permeability of large shale samples provides useful insights for shale gas production. Although the Brinkman formulation is widely used in permeability upscaling of conventional rocks, its application in shale rocks is rare and its accuracy has not been assessed. I remind here that in shale gas flows rarefaction effects are important and that the conventional Navier-Stokes equations are inadequate. This *chapter* aims to address the above problem, by comparing the Brinkman solutions of several two- and three-dimensional random porous media containing fractures with the solutions of the Stokes and Boltzmann equations (for continuum and rarefied gas flows respectively). In Section 6.1, the impact of various morphological characteristics such as porosity, pore size, anisotropy and fracture aperture, on the accuracy of Brinkman model for gas flows in the continuum regime is assessed in 2D structures. Moreover, various 3D porous media generated to mimic the characteristics of real pore-scale shale samples are tested, providing useful insights pertaining to the application of Brinkman approach for permeability upscaling. In Section 6.2, the deviation of the macroscopic model for permeability upscaling in multiscale porous structures (i.e. gas flow is rarefied at the smaller scales) is examined across a wide range of rarefaction. Finally, this *chapter* concludes with some important remarks.

6.1 Upscaling continuum flows

In my numerical computations, I mimic the experimental setup of Beavers & Joseph [75] using 2D and 3D porous media generated with the QSGS algorithm. Several random

porous media are utilised in order to showcase the level of accuracy of the Brinkman approach depending on the properties of permeable materials. A series of simulations are performed, varying the width of the channel, the boundary conditions, and the orientation of the porous medium. I follow the same process as in Section 5.3, nevertheless, in the Brinkman simulations of this *chapter* the effective viscosity is maintained equal to the fluid viscosity. Furthermore, if not specified differently, I remark that the permeameter configuration is employed for all the continuum flow simulations.

6.1.1 Two-dimensional QSGS

Isotropic porous media

To begin with, I investigate statistically isotropic QSGS geometries ($AR = 1$). In this context, I maintain the same channel width in all simulations ($H = 0.05L$). The impact of porosity ϵ, with $c_d = 0.001$, and effective particle size c_d, with $\epsilon = 0.7$, on the accuracy of the Brinkman equation is shown in Table 6.1. We observe that the relative error monotonically decreases while ϵ and c_d increase, even though these two parameters have an opposite effect on the permeability as analysed in [86] and in Section 4.1.1. Nevertheless, the common attribute for both aforementioned parameters is that their enhancement leads to smaller values of the d_{mean}, i.e. the mean diameter of the particles if those are considered to be circular discs.

Recently, Zhang and Prosperetti [144] remarked that a small ratio of the free region width to the radius of the solids could conceal the physical picture. Therefore, noticing the importance of the ratio H to d_{mean} I further examine its influence on the cases of interest. I test the isotropic porous structures of $\epsilon = 0.7$ and $c_d = 0.001, 0.01$, varying the channel thickness. Here I must remark that the permeability of these two random porous media used in this comparison differs by 30 times. In agreement with the previous results, Fig. 6.1 shows that the deviation between the permeability calculated from the solution of Stokes and the Brinkman equations drops when H/d_{mean} increases. The relative error decays to zero in a monotonic fashion and is mostly depending on the value of H/d_{mean}, irrespective of the properties of porous media.

Increasing channel thickness for the same porous medium, practically decreases the amount (proportion) of fluid passing through the pores of the porous block. In other words, only the channel flow is significant and thus the drag term becomes negligible. Therefore, the Brinkman formulation approaches the Stokes equation, which justifies the small relative error in Fig. 6.1. Moreover, as H grows, the effective permeabilities computed using the two porous structures differ less and less and approach the permeability of the flow in the channel only.

Table 6.1: Accuracy assessment of the Brinkman model in isotropic QSGS structures with $H = 0.05L$. First three columns: variation of porosity ϵ while $c_d = 0.001$. Last three columns: variation of c_d while $\epsilon = 0.7$. Note that c_d controls the size of solid islands, where the larger values corresponds to smaller islands.

$c_d = 0.001$			$\epsilon = 0.7$		
ϵ	H/d_{mean}	η	c_d	H/d_{mean}	η
0.6	0.94	23.08%	0.001	1.39	14.16%
0.7	1.39	14.16%	0.005	2.68	9.92%
0.8	2.13	9.12%	0.01	3.44	7.46%

When d_{mean} decreases this leads to a more homogeneous porous medium as stated in our previous publication [86]. It appears that homogeneity favours the Brinkman equation which gives more accurate results increasing the H/d_{mean} ratio, as seen in Fig. 6.1. As H/d_{mean} becomes smaller the relative error reaches its maximum value, which is up to $\sim 23\%$ for the isotropic cases considered. The simulation results of the two aforementioned isotropic porous media with different particle sizes (c_d), thus degree of heterogeneity, for the case of $H = 0.025L$ are illustrated in Fig. 6.2. Streamwise-averaged velocity profiles are presented here, see Fig. 6.2 (c-d), since the flow simulations in this work can be considered quasi-one-dimensional. This is due to the dominance of fractures and due to the small values of the off-diagonal permeability components, compared to the diagonal ones. The velocity contours for the same runs indicate a potential source of error of the Brinkman estimation. We observe from Fig. 6.2 that in the fine-scale models the shape of the channel is not in fact straight, but due to the existence of some pores adjacent to it, its local thickness is often larger. An additional source of uncertainty is the input permeability tensor, whose value is slightly depending on the flow configuration setup [117].

Anisotropic porous media

Moreover, flow simulations using anisotropic QSGS structures are conducted to examine the divergence of permeability from the direct computation. The porous media used herein are generated using the following fixed parameters $\epsilon = 0.7, c_d = 0.001, H = 0.05L$, and for varying values of $AR = 100, 500, 1000$. The deviation shown in Fig. 6.3 from the Stokes solution ranges from approximately 0 to 24% for all the tested anisotropic structures.

To reduce the uncertainty caused by the randomness of the generation algorithm (stochastic) described in Section 2.1, five anisotropic porous structures are created for

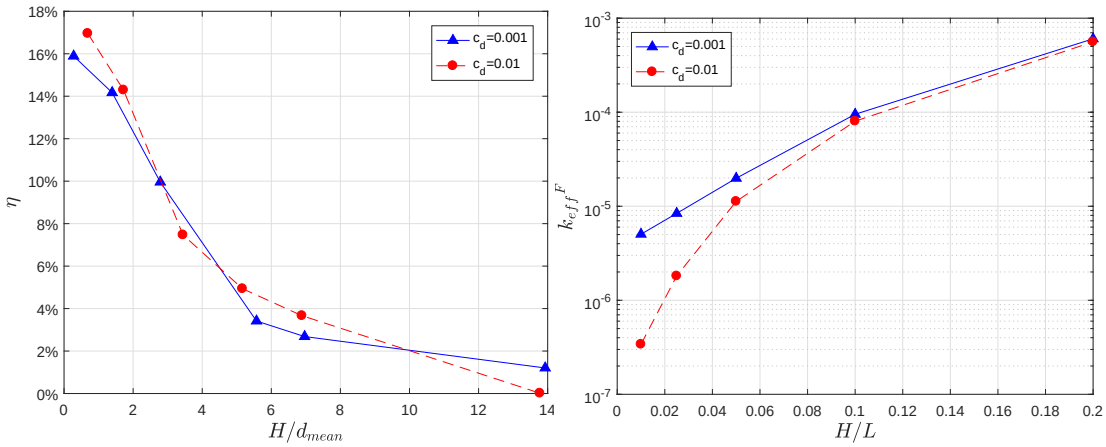

Figure 6.1: Accuracy assessment of the Brinkman model in isotropic QSGS structures when the channel height H varies. The porosity is $\epsilon = 0.7$, and $c_d = 0.001$ and 0.01.

the same set of generating parameters. Despite the fact that the results are quite scattered, the tendency for the relative error of the Brinkman solution is to increase with anisotropy when the flow is parallel to the bedding plane ($k = k_{xx}$) and decrease if otherwise ($k = k_{yy}$). In the former case, due to the orientation of the solid particles (elongated in the horizontal direction), tortuosity τ is close to unity while in the latter, where the same porous medium is rotated by 90°, $\tau \gg 1$. Since the shape of the particles is ellipsoidal in these anisotropic structures, I use the ratio H/L^* (see Eq. (2.19)) in the rest of this study.

Generally speaking, as AR increases, H/L^* is almost fixed when the flow is simulated parallel to bed, in the direction of the elongation of the solid particles ($\tau \approx 1$), since k_{xx} remains in the same order of magnitude [86] (see Section 4.1.1). However, when the flow is in the perpendicular direction ($\tau \gg 1$), H/L^* increases with AR as k_{yy} drops significantly. A clear correlation for the relative error of permeability with respect to the H/L^* cannot be observed for the geometries considered, although it is obvious that it tends to drop for increasing H/L^*. Consequently, both Fig. 6.3(a) and (b) yield the conclusion that when the flow is perpendicular to bed, the error associated with the Brinkman model is reduced with increasing anisotropy. Lastly, the plot of fine-scale effective permeability is an increasing function of the permeability of the porous medium for both isotropic and anisotropic geometries, see Fig. 6.3(c).

The use of an alternative boundary condition at the upper wall is also investigated. Symmetry boundary condition is applied on the reference configuration of $H = 0.05L$ to simulate the case where the fracture is embedded in the middle of the isotropic

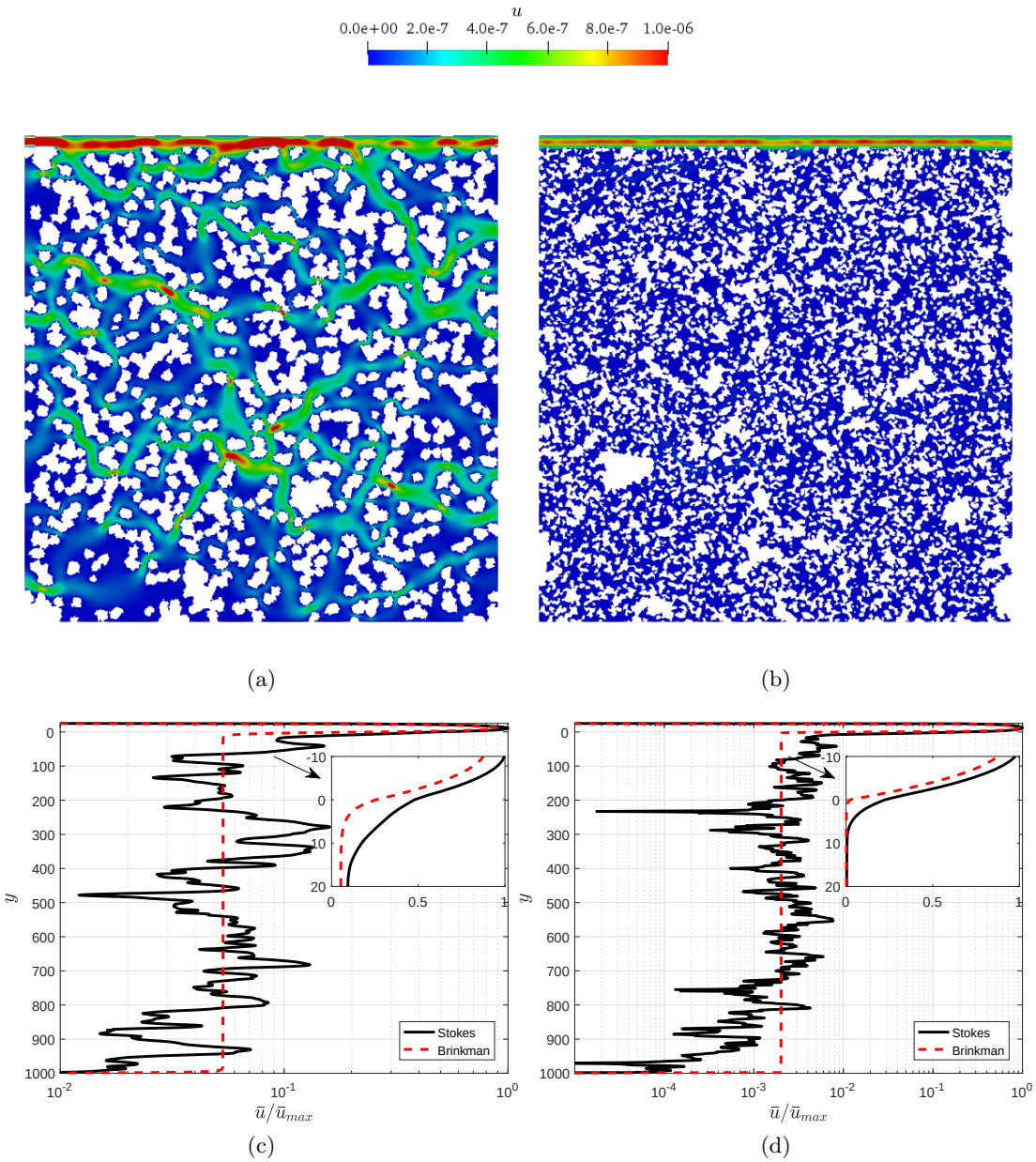

Figure 6.2: Contour plots of the velocity magnitude for the isotropic cases of the same porosity $\epsilon = 0.7$ with $c_d = 0.001$ (a) and 0.01 (b), when $H = 0.025L$. (c) and (d) Profiles of the normalised streamwise-averaged velocity for the porous structures in (a) and (b), respectively. The transition zone (interface is at $y = 0$) is smaller for porous media with smaller c_d since the zone size is related to the effective pore size (as analysed in Section 5.3).

porous medium ($\epsilon = 0.7, c_d = 0.001$). The relative error is then 17% which is slightly higher than the 14% error, which corresponds to the case where the solid wall boundary

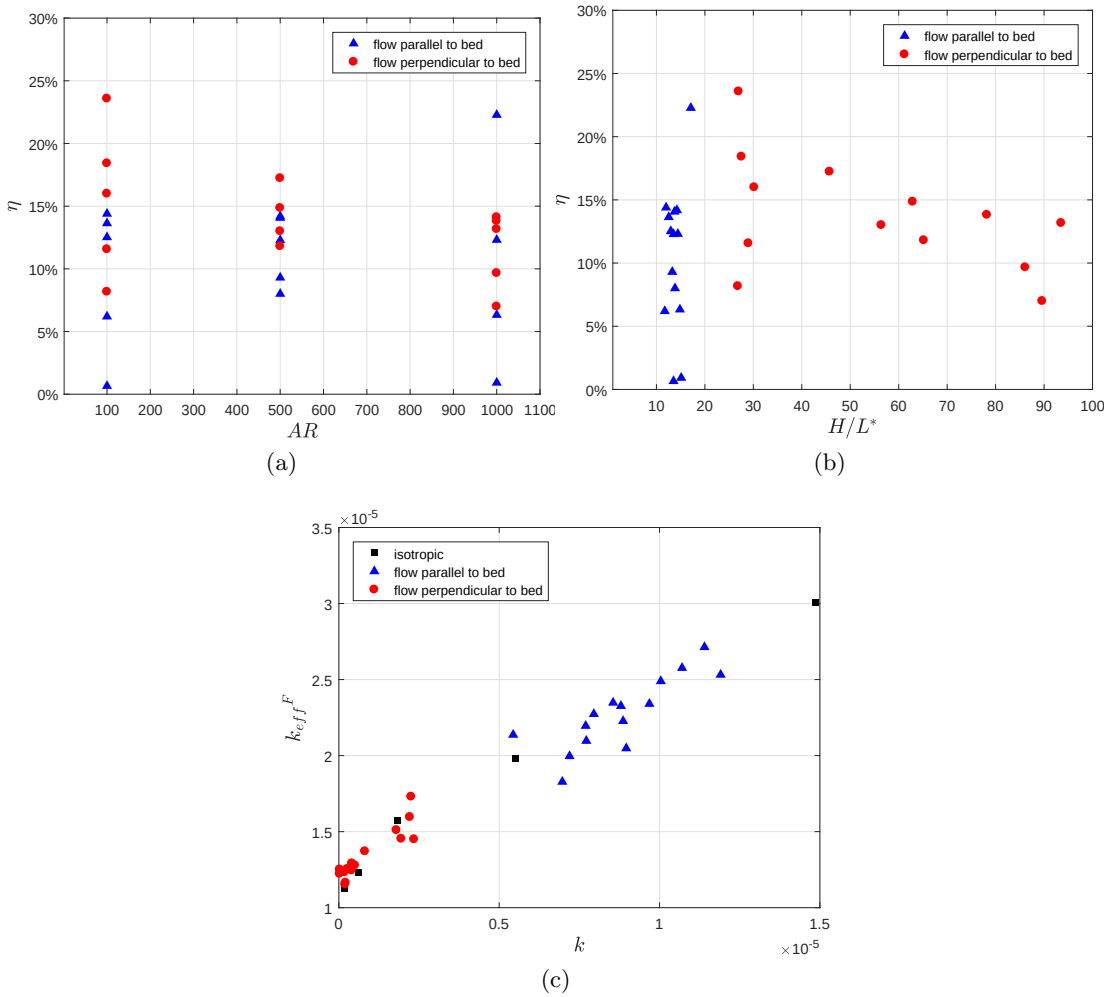

Figure 6.3: (a) and (b) Accuracy assessment of the Brinkman model in anisotropic QSGS structures with $\epsilon = 0.7, c_d = 0.001, H = 0.05L$. (c) The effective permeability of the porous media with an open channel on the top vs. the permeability of the porous media only. Note that $k = k_{xx}$ if the flow is parallel to the bed and $k = k_{yy}$ if otherwise.

condition is employed.

Fragmented fractures in isotropic porous media

Finally, a fragmented fracture is placed in the isotropic structure illustrated in Fig. 6.4. This simulation is performed applying symmetry boundary condition on the lateral walls. For this porous medium of resolution 3000×3000 pixels, $\epsilon = 0.7, c_d = 0.001$ and fracture size $H = 0.4L$, we have $H/L^* = 173$, which is a value often found in shale samples as explained in Section 1.4. The relative error of the effective permeability computed with the Brinkman model is 1%. The significance of this configuration

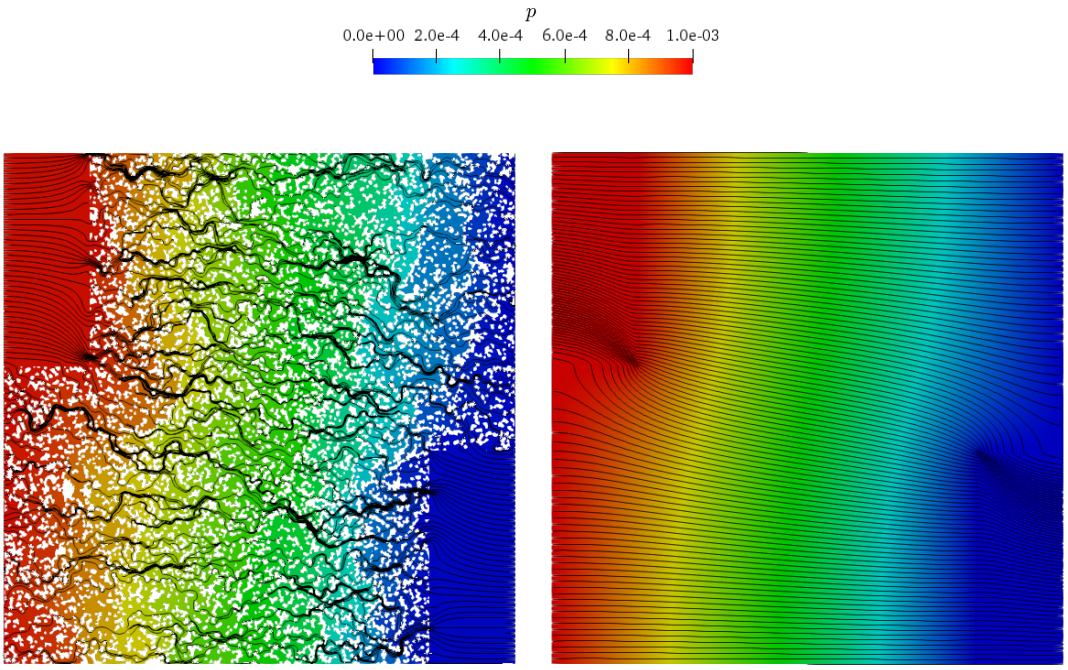

(a) (b)

Figure 6.4: Fine and coarse-scale results of the isotropic case generated using $\epsilon = 0.7, c_d = 0.001$, coupled with a fragmented fracture ($H = 0.4L, H = 173L^*$) along the x-axis. Pressure contour plots with velocity streamlines are illustrated for the Stokes (left) and Brinkman solution (right). The Brinkman model underestimates the effective permeability by 1%.

is that the channel does not go through the whole computational domain, thus the porous medium inevitably determines effective permeability. On the other hand, in the previous examples that contained throughout fractures (with lengths as large as the domain size) the preferential path is clearly the channel, therefore, for large fractures the porous medium contribution to the flow and overall permeability of the porous media becomes negligible.

6.1.2 Three-dimensional QSGS

Recently, Wang et al. [88] quantified pore-scale heterogeneity and anisotropy of several shale samples using a geometry-based method, and generated $3D$ QSGS structures having statistical and morphological characteristics close to real samples. The advantage of using this type of reconstruction instead of high-resolution images lies in the fact that we can study the impact of each factor of interest individually, by keeping the rest constant. In this work, I use similar generating parameters as in [88] in order to

Table 6.2: Generation parameters of 3D QSGS structures and simulation results where $\mathrm{d}p/\mathrm{d}x$ is applied and fracture with $H = 0.02L$ is in y axis. τ here refers to the highest component of tortuosity which in the case of anisotropic structures is τ_z.

Case	c_d^F/c_d^C	ϵ^F	ϵ	ϵ_f	AR	H/L^*	k	A_f	τ	η
1	-	-	0.3	0.26	1	5.59	4.16×10^{-7}	0.98	1.71	21%
2	-	-	0.3	0.26	100	5.53	4.25×10^{-7}	0.73	1.68	14%
3	100	0.2	0.3	0.14	1	14.73	3.27×10^{-8}	0.94	2.52	21%
4	100	0.2	0.3	0.13	100	16.18	2.50×10^{-8}	0.74	2.45	21%
5	500	0.2	0.3	0.13	1	14.44	3.18×10^{-8}	0.77	2.36	21%
6	500	0.2	0.3	0.13	100	14.30	3.22×10^{-8}	0.66	2.38	21%
7	100	0.2	0.25	0.2	1	9.36	1.12×10^{-7}	0.85	2.00	27%
8	100	0.15	0.22	0.12	1	15.83	2.50×10^{-8}	0.17	2.09	32%

construct random porous media to be realistic representations of the shale matrix, and thus acquire more comprehensive conclusions regarding the accuracy of the Brinkman model for upscaling from the pore-scale. The full list of parameters of the 3D geometries considered and the corresponding simulation results are summarised in Table 6.2.

Influence of anisotropy

To start with, I investigate the accuracy of the Brinkman formulation using artificial anisotropic samples with a fracture on top. To this end, I reconstruct two $3D$ QSGS structures; the first structure is statistically isotropic, while the second is isotropic in the directions parallel to the bed (x, y) and anisotropy appears in the perpendicular direction (z). This type of anisotropy, i.e. transverse isotropy, is common in shale, due to the compaction of the rock in the vertical direction [88, 125, 145].

These random porous media are generated using $AR = 1$ and 100 (see Cases 1 and 2 respectively in Table 6.2 and Fig. 6.5 for views of Case 2 geometry). The aspect ratio (AR) herein signifies the ratio of the main directional growth parameters where in the case of transversely isotropic structures this yields $(D_x = D_y)/D_z$. The flow configuration for the $3D$ random porous media is identical to the one described in Section 6.1.1. Fixed pressure is applied on the inlet and outlet boundaries, while the rest are treated as stationary walls. The straight fracture $(H = 0.02L)$ is located on top of the porous domain with its height placed on either of the two transverse directions with respect to the pressure gradient.

As previously mentioned, the structures under consideration are either isotropic, or

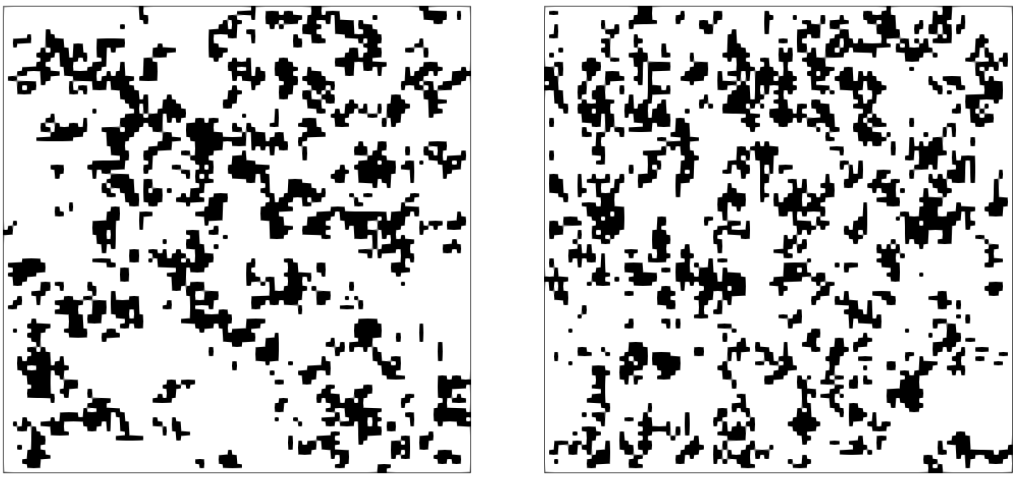

(a) (b)

Figure 6.5: Anisotropic 3D QSGS structure (Case 2) where the bedding plane (z) is shown on the left and a perpendicular plane (x) is on the right. The structure is isotropic in plane z and anisotropic in the other two planes where the pores (shown in black) are elongated.

transversely isotropic. Thus, we expect that for the former case the effective permeability results will be practically identical for pressure gradient applied in any of the three directions. Thereby, the same applies for the placement of the fracture. Indeed, my numerical solutions of the Stokes equation show that for $AR = 1$ the difference between various pressure gradients and fracture positions is below 0.7%. For the latter case, $\mathrm{d}p/\mathrm{d}x$ and $\mathrm{d}p/\mathrm{d}y$ should give similar k_{eff} while $\mathrm{d}p/\mathrm{d}z$ is expected to result in inferior values since $k_{zz} < k_{xx} \approx k_{yy}$ for these type of porous media. The fracture position could herein influence effective permeability. In my simulations, the transversely anisotropic structure $AR = 100$ exhibits a difference in effective permeability in the order of 1% for the two different fracture positions while $\mathrm{d}p/\mathrm{d}x$ is imposed. When the flow direction is driven by pressure gradient in the z direction ($\mathrm{d}p/\mathrm{d}z$), the resulting k_{eff} differs by 2%, even though $k_{zz} \approx 0.7k_{xx}$. This confirms the importance of the fracture flow contribution to effective permeability. Comparing the two structures, having the same flow configurations, the maximum difference observed in k_{eff} is in the order of 5% for $\mathrm{d}p/\mathrm{d}z$, which is expected since the anisotropic structure results in smaller permeability k_{zz}. It is worth mentioning that all the aforementioned percentages tend to decrease with increasing H.

In the rest of this *chapter*, it may be more meaningful to consider only the setup

where a $\mathrm{d}p/\mathrm{d}x$ is applied and the fracture is in the y axis (choosing $\mathrm{d}p/\mathrm{d}y$ and fracture in the x axis would have the same effect). This is due to the fact that is it desirable to choose the fracturing direction parallel to the bedding plane, where the flow is facilitated [33] and which is the most common flow direction in shale [88]. The relative error of the Brinkman model for the aforementioned structures is 21% and 14% for the isotropic and the transversely isotropic cases respectively (see Case 1 and 2 in Table 6.2).

Influence of heterogeneity

To study the effect of heterogeneity, several QSGS structures are created as analysed in Section 2.1 with $c_d^F/c_d^C = 100$ and $c_d^F/c_d^C = 500$, introducing non-uniformity in the pore size distribution. It is found that heterogeneity tends to increase with c_d^F/c_d^C [88]. At the same time, transverse isotropy is superimposed to imitate the real porous structure.

Regarding the anisotropy factor A_f used in Table 6.2 and defined in Eq. (2.18), values close to unity indicate a statistically isotropic medium, while values close to zero refer to high anisotropy. Particular attention must be paid to the heterogeneous cases, where the matrix proves to be anisotropic even though this is not explicitly determined in the generation process ($AR = 1$). This can be (partly) attributed to the low porosity of the medium in combination with the fact that only a few flow paths are available due to the dominance of the larger pores. When anisotropy is induced by heterogeneity it is not necessary that k_{zz} has the lowest value compared to the rest diagonal permeability terms. On the contrary, this is assured for the anisotropic structures where $AR > 1$.

Moreover, it is confirmed that for the same porosity (Cases $4-6$), intrinsic permeability is higher for more heterogeneous structures (Cases $5, 6$ have larger c_d^F/c_d^C) as the pores have better connectivity [88]. This can also be justified by the corresponding reduction of tortuosity for the more heterogeneous structures. The porous media of Cases 4 and 8 have the same intrinsic permeability and similar porosities, however they exhibit different relative error of k_{eff} (21% and 32% respectively). Although they are both constructed based on $c_d^F/c_d^C = 100$, the porosity value assigned to each pore size is different, resulting in Case 8 being more heterogeneous than Case 4. Additionally, Case 8 is more anisotropic as reflected from the decreased anisotropy factor A_f. In agreement with my outcomes for the 2D porous media presented in Section 6.1.1, the Brinkman estimation for the more heterogeneous and anisotropic structure leads to larger error when the flow is parallel to the bedding plane. On the other hand, comparing Cases 3 and 7 we observe that the significant decrease of H/L^* and A_f for the porous medium flow of Case 7 leads to increase of the Brinkman error as previously detected for $2D$ structures. Despite the fact that the porous medium of Case 7 is less heterogeneous the effect of the other two factors here prevails.

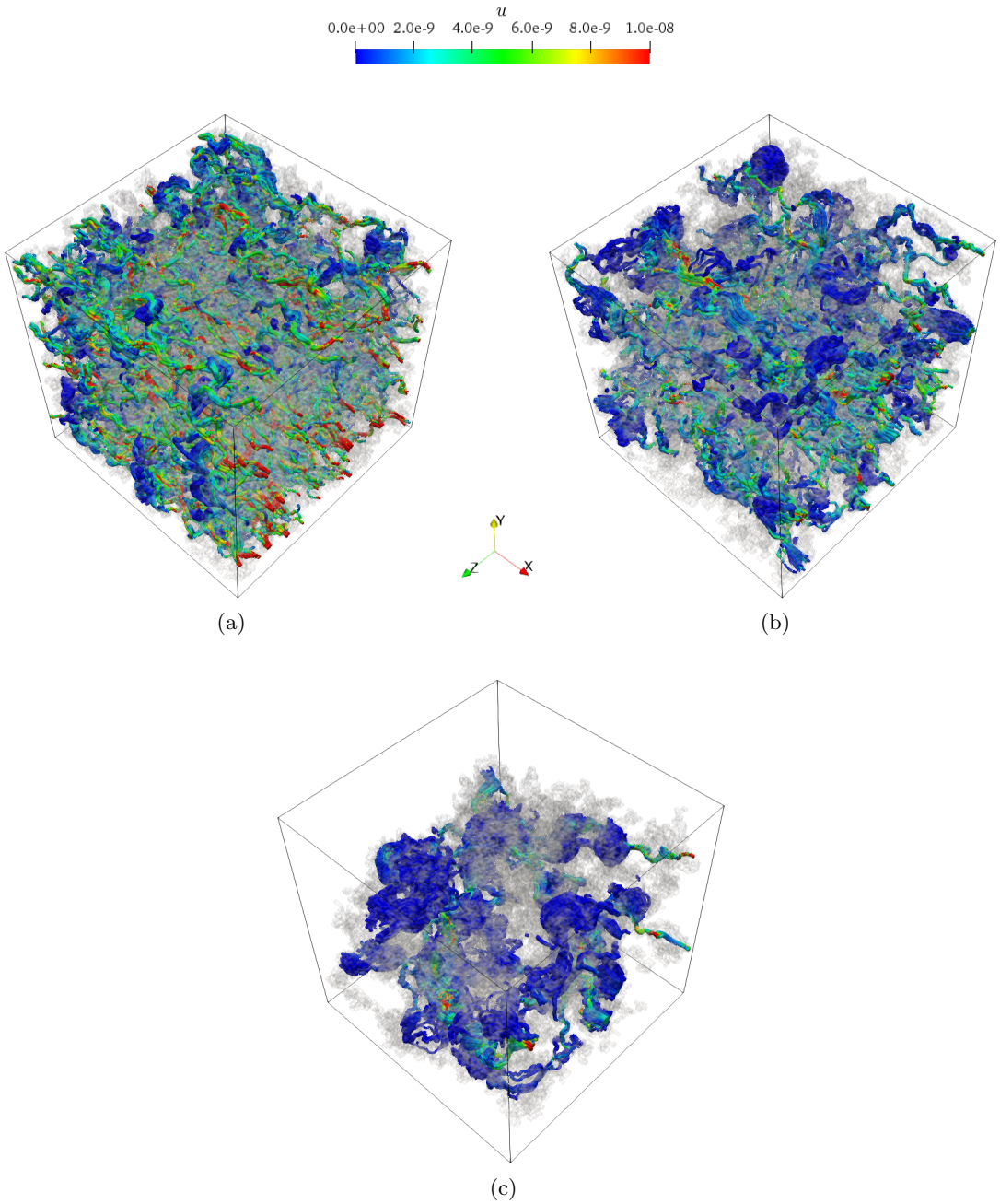

Figure 6.6: The mesh (pore space) of 3D Case 1 (isotropic), Case 7 and Case 8 (heterogeneous) along with velocity streamlines for $\mathrm{d}p/\mathrm{d}x$ shown in (a), (b) and (c) respectively. In the last two subfigures, there are many large pores illustrated with blue colour (due to smaller velocity of the flow there). This is due to the generation process allowing a small portion of the pores to be of greater size ($c_d^C = 0.0001$). The grey areas indicate dead end pores, or pore areas with very small flow velocities.

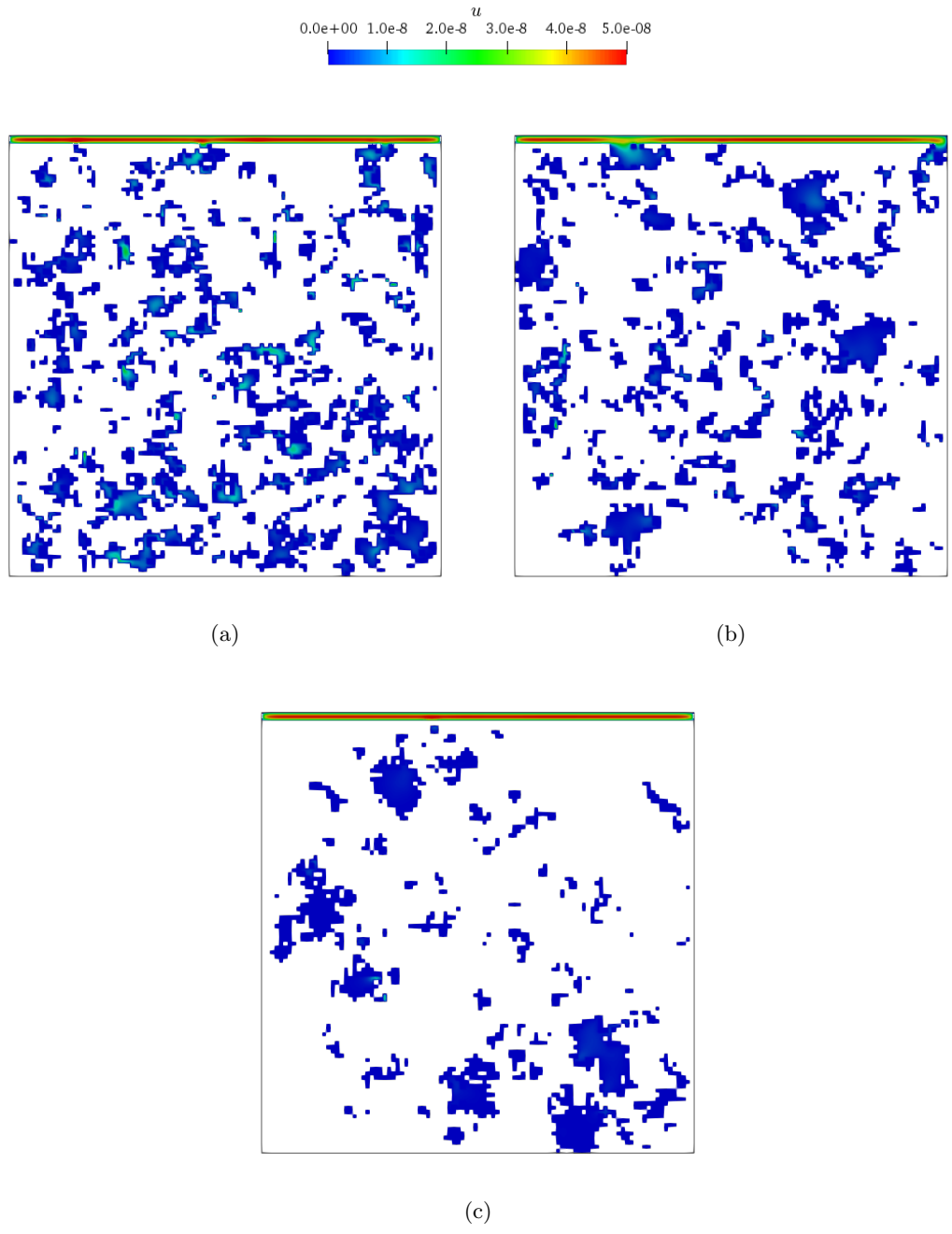

Figure 6.7: Velocity contour plots (x plane) for the isotropic Case 1 and the heterogeneous Cases 7 and 8 illustrated in (a), (b) and (c) respectively. The fracture size is $H = 0.02L$. The flow is driven by a pressure gradient in the x direction.

The mesh along with velocity streamlines of a few of the aforementioned porous structures (Cases $1, 7$ and 8) is depicted in Fig. 6.6. The focus is on the porous blocks only, thus $H = 0$. The heterogeneous cases compared to the isotropic ones have a large

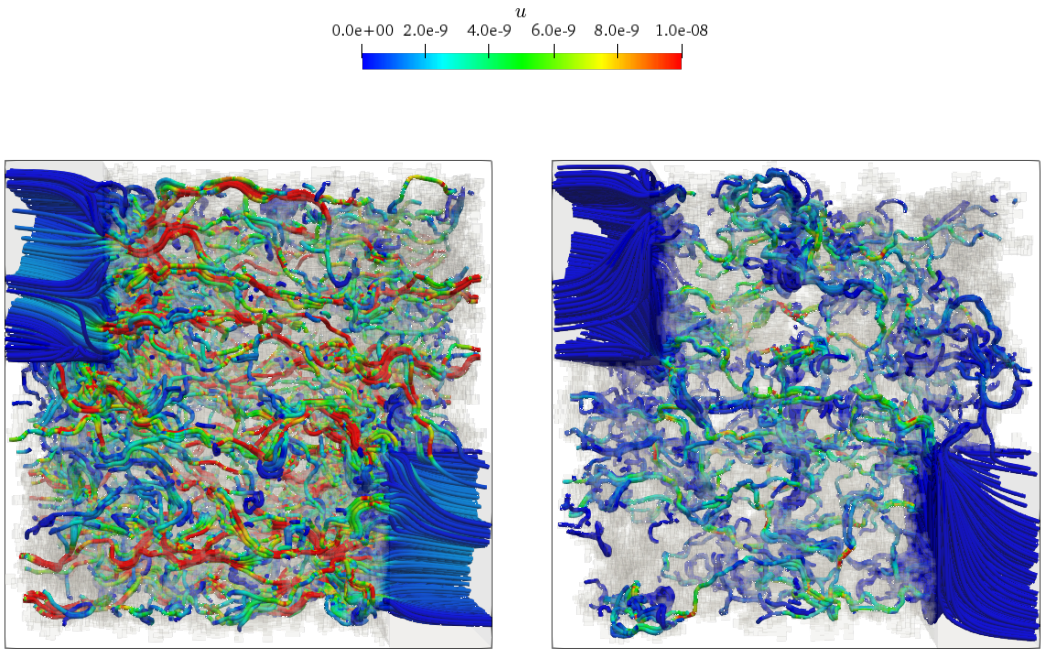

(a) (b)

Figure 6.8: Velocity streamlines of the 3D Case 1 (left) and 6 (right), with a fragmented fracture ($H = 0.4L$) added along the x-axis, where $H = 91L^*$ for Case 1 and $H = 233L^*$ for Case 6. The Brinkman model underestimates the effective permeability by 2% and 21% respectively.

proportion of significantly large pores where the flow has low velocity. This can be further observed in Fig. 6.7 where the velocity contours of same geometries are shown (x plane). Herein, the porous block is connected to a straight fracture of thickness $H = 0.02L$.

As seen in Fig. 6.8, a fragmented fracture ($H = 0.2L$) is placed in the QSGS structures of Case 1 and Case 6, similarly to the 2D configuration illustrated in Fig. 6.4. The fracture aperture to pore size ratio is about $H/L^* = 91$ and $H/L^* = 233$ for the respective geometries, while the corresponding relative error of the Brinkman estimation of effective permeability is 2% and 21%. Even though the straight fracture configuration gives same error for both structures (see Table 6.2), in this configuration the error differs significantly. This is due to the fact that the permeability tensor is obtained using the initial porous medium, which is now partly covered by the fracture. Since the geometry of Case 1 is more homogeneous, its $\mathbf{k}$ is still representative when we introduce the fracture. However, in the more heterogeneous and less permeable geometry of Case 6, the addition of the fracture has a more pronounced impact on the connectivity of

the pores, altering the permeability tensor.

If we consider the structures of Table 6.2 to have a cell size of 20nm, then the whole sample size is $L = 2\mu$m. Thus, the dimensional intrinsic permeabilities of the simulated 3D porous media are in the range of 9.98×10^{-20} to 1.70×10^{-18}m^2, i.e. approximately 101 to 1722nD. This permeability range, between nano and micro-Darcies, is typical for shale rock [1]. Additionally, the relevant effective pore size is only a few nanometres (3 - 9nm) and their porosities are low enough for the above structures to be regarded, to some extend, as close approximations of real shale samples. Consequently, we anticipate that the relative error of the Brinkman model using shale images will be close to the values reported in Table 6.2, i.e. around $20\% - 30\%$.

6.2 Upscaling rarefied flows

Shale gas flow is mostly in the slip and transition regimes, therefore, I examine the performance of the Brinkman model, where intrinsic permeability of porous media is replaced by apparent permeability due to gas rarefaction effects, on the basic configuration illustrated in Fig. 2.3, for increasing Kn. When $Kn > 0$, the fine-scale results are obtained by solving the linearised BGK equation using the discrete velocity method [21, 56, 83, 86], see Section 2.2.2. Due to this, in this *section*, the boundary conditions employed are periodic in the inlet/outlet and symmetry on the lateral walls. On the solid walls, the solution is subject to the no-slip boundary condition when $Kn = 0$, while for larger Knudsen number, the diffuse boundary condition is imposed.

The 2D porous medium used herein is isotropic with $\epsilon = 0.7$ and $c_d = 0.001$. The QSGS resolution is 3000×3000 pixels and for the numerical mesh ten fluid layers are added so that periodicity can be imposed (see Section 2.2.3). The height of the fracture on top is $H \approx 0.02L$ and $H \approx 3.5L^*$, where L^* is defined in Eq. (2.19). The fracture size is chosen to be small in order to facilitate the visualisation in Fig. 6.10, since increasing the fracture size the contribution of the porous medium to effective permeability becomes negligible. Additionally, an important factor for this choice is the computational cost of DVM which is already demanding for this domain size. Simulations are performed for global $Kn = 0,\ 0.0001,\ 0.001$ and 0.01, and the velocity contours are shown in Fig. 6.9. In order to appropriately understand the rarefied flow behaviour I however use the effective Knudsen number of the average pore and the Knudsen number of the fracture, i.e. $Kn^* = \lambda/L^*$ and $Kn^f = \lambda/H$ respectively. I highlight that for $Kn = 0.0001$ the direct simulation was also performed solving the Stokes equations coupled with FVBC. The computed fine-scale permeability deviates by less than 1% compared to the one computed solving the Boltzmann model equations.

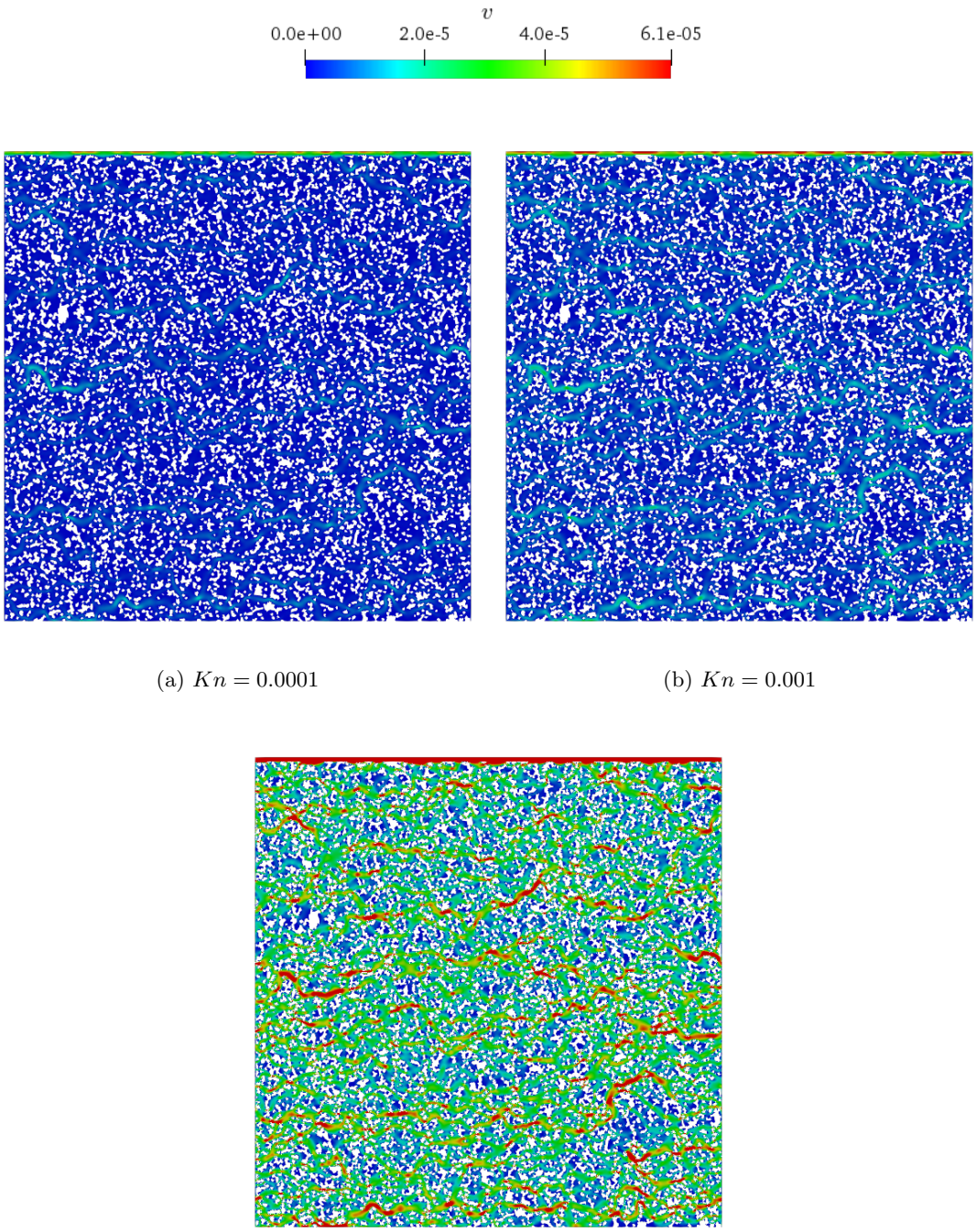

(a) $Kn = 0.0001$ (b) $Kn = 0.001$

(c) $Kn = 0.01$

Figure 6.9: Contour plots of v for three BGK solutions calculated at $Kn = 0.0001, 0.001$ and 0.01. The streamwise flow velocity u is normalised by $u_{ref} = 2\bar{p}L/\mu\sqrt{\pi}$ resulting to v. The isotropic porous medium used has $\epsilon = 0.7$ and $c_d = 0.001$ and the straight fracture has an aperture $H = 0.02L$ and $H = 3.5L^*$. The flow rate for the largest Kn is dramatically increased, indicating significant rarefaction effects.

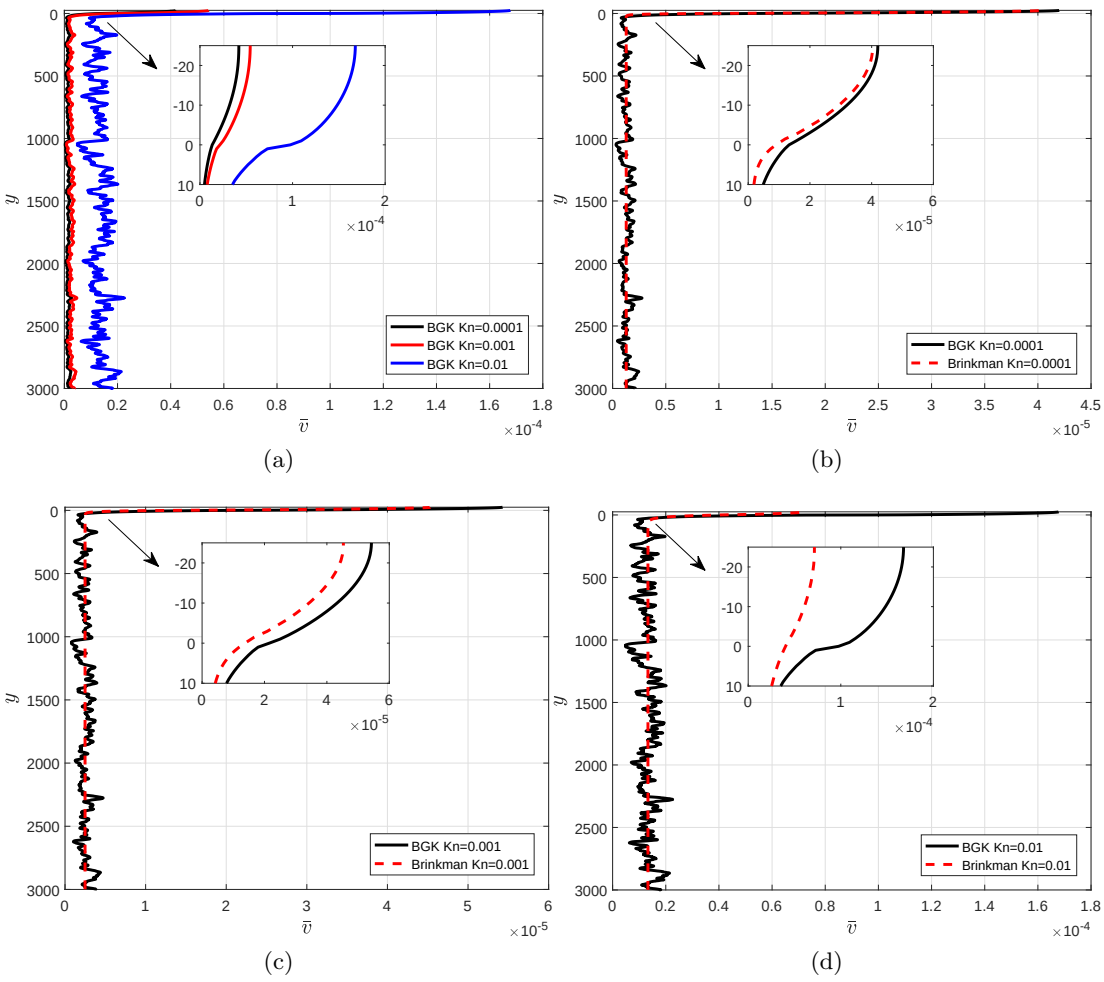

Figure 6.10: Streamwise-averaged profiles of v, which equals u normalised by $u_{ref} = 2\bar{p}L/\mu\sqrt{\pi}$. The interface is at $y = 0$. The relative error of the Brinkman estimation is 4% for $Kn = 0.0001$, 5% for $Kn = 0.001$ and 7% for $Kn = 0.01$. Based on the average pore size, $Kn^* = 209 \times Kn$ while the effective Kn at the fracture is $Kn^f = 60 \times Kn$.

It is worthwhile to note that for $Kn = 0$ the Stokes equations are solved and the respective relative error and graphs are very similar to the ones resulting for $Kn = 0.0001$; hence they are omitted in Figs. 6.9 and 6.10. The full list of results can be found in Table 6.3. Visually inspecting Fig. 6.9 and the comparative Fig. 6.10a we can observe a dramatic increase in v for the case of $Kn = 0.01$ compared to $Kn = 0.001$ and $Kn = 0.0001$. This indicates that the computed effective Kn of the flow ($Kn^* = 2$) truly lies in the transition regime.

The coarse-scale results in Fig. 6.10(b-d) indicate that the flow in the porous medium is adequately represented for all three Knudsen numbers tested. I should

Table 6.3: The apparent permeability and error of the Brinkman model for rarefied gas flows in 2D QSGS porous medium with a fracture on top with $H = 0.02L$. The column titled $\eta_{Kn=0}$ refers to the relative error of the Brinkman estimation when k_{eff}^{C} in Eq. (5.7) is calculated based on the intrinsic permeability of the porous media.

Kn	Kn^*	Kn^f	k_a	η	$\eta_{Kn=0}$
0.01	2	0.6	1.52×10^{-5}	7%	90%
0.001	0.2	0.06	2.84×10^{-6}	5%	50%
0.0001	0.02	0.006	1.45×10^{-6}	4%	9%
0	0	0	1.35×10^{-6}	4%	4%

emphasise here that the permeability tensor used as input for each Brinkman simulation is derived using the BGK results for each corresponding Kn number, following the methodology described in Section 2.3.

As far as the area of the straight fracture is concerned, increasing Kn the deviation between the BGK and Brinkman results increases. This is due to the fact that in the Brinkman model, practically the NSEs are solved at the fracture, which are proven to break down in the transition and free flow regimes as mentioned in Section 2.2. Namely, for $Kn = 0.01$ the flow in the fracture is significantly underestimated, therefore, the relative error of effective permeability increases to 7%. Nevertheless, this error is still small thanks to the precise $\mathbf{k}$ used, which lays a firm foundation for upscaling. This is of central importance, since using $\mathbf{k}$ obtained from the NSEs instead of the BGK model has a notable effect on the coarse-scale effective permeability. For example, it results in underestimation of permeability up to $\eta_{Kn=0} = 90\%$ at $Kn = 0.01$.

Due to the small fracture size, its contribution to the total mass flow is limited hence the error involved in the value of k_{eff}^{C} is not so significant. On the other hand, in the case of a larger fracture for the same global Kn, Kn^f decreases, resulting to the Brinkman model being accurate for a larger range of global Kn. Consequently, in this case the relative error is expected to be even smaller.

6.2.1 Computational time

The solution of the NS and Brinkman equations for the cases analysed in Sections 6.1.2 and 6.2 was performed using ARCHIE-WeSt. Each node of the HPC facility has a dual Intel Xeon Gold CPU 6138 2.0GHz and 80 threads in total, 40 of which are herein occupied. The solution of the Boltzmann model equation is performed on a machine with dual Intel Xeon CPU E5-2680 v4 2.40 GHz. 32 out of the 56 threads were utilised. The number of iterations together with the elapsed time for the aforementioned

Table 6.4: Iteration steps and elapsed time for the numerical solution of the NSEs (Fine-scale model). The same information is reported for the solution of the Brinkman equation (Coarse-scale). The corresponding computational mesh is $200 \times 208 \times 200$ and $50 \times 104 \times 50$. The time is measured by wall clock time. The properties of the fractured porous media corresponding to each case are listed in Table 6.2.

	Fine-scale		Coarse-scale	
Case	Iterations	Time (s)	Iterations	Time (s)
1	243	152	50	2
2	248	143	50	2
3	333	117	50	2
4	134	78	50	2
5	137	41	50	2
6	135	37	50	2
7	136	45	50	2
8	138	45	50	2

simulations of the corresponding fractured porous media are listed in Tables 6.4 and 6.5. The relevant comments of Sections 3.1.1 and 4.2.2 also apply on the fine-scale results of this *chapter*.

Regarding the 3D pore-scale simulations performed in Section 6.1.2, we see in Table 6.4 that the convergence is achieved in a few minutes due to the small number of cells utilised, i.e. $200 \times 208 \times 200$. The time required is roughly related to the porosity (number of fluid cells) of the porous medium. The coarse-scale solution was fast to achieve, in about 2s since the corresponding mesh is even coarser, about 24 times, i.e. $50 \times 104 \times 50$.

Now attention is turned to the 2D rarefied flow simulation of Section 6.2. For $Kn = 0$, where the same computational resources are used for both the fine and coarse-scale models, we see in Table 6.5 that the computational cost is reduced by more than ten times thanks to the coarser mesh requirements (3010×3025 vs 1000×1020 respectively). In particular, as fas as the coarse-scale results are concerned, we can also observe that the computational cost rises with Kn, when the input $\mathbf{k}$ of the model increases. For more information regarding the meshing details the reader is directed to Section 2.2.

Table 6.5: Iteration steps and elapsed time for the numerical solution of the linearised BGK equation using the implicit discrete velocity method when $Kn > 0$ and for the numerical solution of the NSEs when $Kn = 0$ (Fine-scale model). The same information is reported for the solution of the Brinkman equation (Coarse-scale). The time is measured by wall clock time. The fractured porous medium is depicted in Fig. 6.9. The spatial mesh resolution is 3010×3025 for the fine-scale model and 1000×1020 for the coarse-scale. The molecular velocity space (for $Kn > 0$) is discretised with a polar velocity grid of 4 (discrete radius) $\times$ 100 (discrete angles). Note that the computational resources used for the BGK simulations are different than for the remaining runs.

			Fine-scale		Coarse-scale	
Kn	Kn^*	Kn^f	Iterations	Time (s)	Iterations	Time (s)
0.01	2	0.6	16000	75600	22705	1837
0.001	0.2	0.06	1000	45890	18654	1526
0.0001	0.02	0.006	17000	81849	14101	1109
0	0	0	20204	13785	13925	1088

6.3 Conclusions

In this *chapter*, I have thoroughly investigated the error of the effective permeability estimation when the Brinkman model is used to upscale shale permeability from the pore-scale. I performed 2D and 3D flow simulations using random porous media generated with the QSGS method where several morphological properties can be controlled. Extensive analysis has been performed on both continuum and rarefied gas flows which are often encountered in shale. To the best of my knowledge, this is the first time that the accuracy of the Brinkman model using realistic porous media and flow conditions is examined.

For continuum flows, a parametric study of isotropic 2D structures revealed that homogeneity favours the estimation of the Brinkman model, no matter if homogeneity is resulted from high porosity or small particle size. Additionally, anisotropy in 2D geometries, when the flow is perpendicular to bed, leads to reduced error. In other words, for highly tortuous porous media, the increase of the H/L^* factor is associated with more accurate prediction of the effective permeability. However, when the flow is parallel to the bedding plane, this error tends to increase. My simulations using artificial 3D random porous media demonstrated that a reasonable relative error in the estimation of effective permeability occurs when the Brinkman formulation is used. These 3D porous media are carefully constructed to approach the properties of real shale sample images of high resolution. Even though the cases studied are quite complex

and the effect of each parameter cannot be easily uncoupled, the same conclusions as in 2D structures apply. The Brinkman model is less reliable when used for porous media that exhibit high heterogeneity and anisotropy. Most of the flow configurations performed have a straight fracture on top of the porous region as it is common in the literature. However, a fragmented channel is also placed in two different porous media to demonstrate a more realistic example of a shale sample with a microfracture. The Brinkman-derived coarse-scale permeability of both configurations is in good agreement with the fine-scale model.

The suitability of the Brinkman model is also verified on rarefied gas flows, where the permeability of porous media is actually the apparent permeability which is a function of gas pressure. Microscopic 2D simulations spanning a wide range of Knudsen numbers are performed by solving the linearised BGK equation. The apparent permeability tensor is then utilised as input for the macroscopic representation of Brinkman leading to well predicted effective permeability for rarefied gas flows. Neglecting the rarefaction effects is here proven to result in significant underestimation of the macroscopic property.

I must remark that in this work, I adopt $\mu_{eff} = \mu$ when using the Brinkman equation and the accuracy of the results is adequate for the realistic cases simulated. Thus, I recommend to avoid using one of the complex and controversial alternatives suggested in the literature when the aim is to predict flow properties of shale.

In conclusion, according to my numerous 2D and 3D simulation results the effective permeability extracted from the Brinkman formulation compares favourably to its fine-scale counterpart computed solving the Stokes and the Boltzmann model equations. I thus have confidence that the use of Brinkman model is suitable for shale permeability upscaling from the pore-scale.

Chapter 7

Conclusions

7.1 Summary

The work developed in this thesis contributes to a better understanding of shale gas flows at the pore-scale and beyond. Established theoretical and computational studies relevant with pore-scale rarefied flows of ultra-tight porous media and upscaling techniques are thoroughly analysed. These studies constitute the background and basis of the present research. My research has computationally addressed the direct simulation of random porous media flows across a wide range of rarefaction, decoding the behaviour of apparent permeability pertinent to the geometrical complexity and the Knudsen number, and explaining the slip factor trend observed by Klinkenberg. Moreover, a new appropriate permeability formulation was proposed, independent of empirical parameters. Then, the upscaling of pore-scale permeability was meticulously investigated, indicating the suitability of numerical methods. Particularly, I found that the use of the Brinkman model performs well in providing the effective permeability of fractured ultra-tight porous media. Overall, throughout this research, the whole workflow that leads to a good approximation of the effective permeability of shale samples with microfractures was investigated.

Rigorous theoretical and numerical analysis was carried out using gas kinetic theory, mainly solving the BGK and the Navier-Stokes equations. My research proves that the Navier-Stokes equations with the first-order velocity-slip boundary condition can only predict apparent gas permeability of porous media to the first-order accuracy of the Knudsen number. Consequently, the commonly used slip-corrected expression provides a good estimation of the apparent permeability only for near equilibrium gas flows. This is more evident in the case of complex porous media flows and/or when the tangential momentum accommodation coefficient in the diffuse-specular boundary condition is non-unitary, since then the slip factor exhibits a behaviour close to the one

found by Klinkenberg. This conclusion implies that many widely used semi-analytical permeability models taking into account only slip flow and/or based on the straight tube simplification of the porous medium are unsuitable to predict apparent gas permeability of shale gas flows.

To further analyse the dependence of intrinsic and apparent gas permeability (thus slip factor) on structural porous media properties, an extended parametric study was performed using controllably random two-dimensional geometries. These results, imposing the diffuse boundary condition, confirmed the slip factor tendency observed by Klinkenberg on his experimental measurements, where real core samples were used. In these complex porous media, the slip-corrected apparent permeability failed to provide an accurate apparent permeability estimation, often leading to its underestimation. An important contribution of this work is a new semi-analytical permeability formulation, based on the above numerical results, which takes into account the structural characteristics of the permeable material and is valid up to the slip regime. It should be stressed that the proposed expression does not require any input parameters derived from numerical or experimental data. Furthermore, this formulation can serve as a starting point for further modelling of rarefied flows in complex geometries.

Having established the accurate determination of pore-scale apparent permeability, it is of central importance to upscale the computed properties to larger scales, where the direct simulation is no longer possible, and a separation of scales appears. To this end, widely used analytical upscaling techniques were compared with the numerical solution of the Darcy equation and the numerical method was deemed more sensitive and appropriate. Afterwards, the evaluation of numerical upscaling methods was conducted performing direct flow simulations on the explicit geometries of numerous porous media and comparing the computed fine-scale permeability with its coarse-scale counterpart, derived using upscaling. This evaluation includes the numerical solution of not only Darcy, but also Brinkman equation which solves the Stokes equations in the regions identified as void space and Darcy's law in the porous domain. This hybrid model is a promising tool for the effective permeability estimation of shale with microfractures. Aiming to study this model further for the cases of interest, I focus on the controversial issue of the effective viscosity and the capability of the equation to capture the velocity profile near the fluid-porous interface. A few alternative values of effective viscosity are examined, as well as the concept of a variable permeability near the interface. The conclusion of this study was that lacking a suitable universal effective viscosity model or local treatment of the transition zone, the Brinkman approach should be used considering the effective viscosity equal to fluid viscosity.

Taking this outcome into account, I examine the accuracy of the Brinkman model

using numerous fractured random two and three-dimensional porous media. For simplicity, I mimic the experimental configuration of Beavers & Joseph, adding a straight channel on top of the porous domain. A parametric study of isotropic 2D structures revealed that homogeneity, whether its due to high porosity or small particle size, favours the accuracy of the Brinkman model. Additionally, I found that anisotropy in 2D geometries, when the flow is perpendicular to bed, leads to reduction of the error, which is increased if the flow is parallel to bed. To verify the suitability of this model for this application, likewise, I use it on artificial 3D porous media which have properties similar to real shale samples. Similar conclusions are drawn here, indicating that generally the Brinkman-derived coarse-scale permeability is in good agreement with the fine-scale model. Since shale permeability is actually a function of gas pressure, the Brinkman model was also verified for rarefied conditions using apparent permeability as input. Comparison with the fine-scale results, obtained solving the model Boltzmann equations, not only proves that the resulting error is small, but also that neglecting the rarefaction effect would lead to a serious underestimation of the effective permeability of the fractured sample. Overall, the suggested workflow provides accurate estimates of multiscale intrinsic and apparent shale gas permeability.

7.2 Future work

The work developed in this thesis may be extended as follows:

- The extensive parametric study and analysis performed in Chapter 4 could be performed for 3D QSGS porous media too, with or without the explicit enforcement of heterogeneity.
- The semi-analytical permeability formulation proposed in Chapter 4 may be extended to deal with 3D QSGS porous media and/or modified to cover a wider range of Knudsen numbers. Inspiration can be drawn from [146] for the former case.
- The suitability of the Brinkman formulation could be examined accordingly for realistic fracture shapes. One main challenge lies in the fact that the porous domain adjacent to the fracture is no longer rectangular, as in the simulations of Chapters 5 and 6, thus an appropriate treatment is needed so that the accuracy of the permeability used as input is ensured.
- The workflows applied in Chapters 5 and 6 may also be applied in imaged shale samples starting from high-resolution (pore-scale) to low-resolution images, such

as those corresponding to plugs and whole cores. The effective permeability computed solving the Darcy or Brinkman equations can be compared to experimental measurements following the work of [54].

References

[1] N. Chakraborty, Z. Karpyn, S. Liu, and H. Yoon, "Permeability evolution of shale during spontaneous imbibition," *Journal of Natural Gas Science and Engineering*, vol. 38, pp. 590–596, 2017.

[2] B. Guo, L. Ma, and H. A. Tchelepi, "Image-based micro-continuum model for gas flow in organic-rich shale rock," *Advances in Water Resources*, vol. 122, pp. 70–84, 2018.

[3] L. Ma, K. G. Taylor, P. J. Dowey, L. Courtois, A. Gholinia, and P. D. Lee, "Multi-scale 3D characterisation of porosity and organic matter in shales with variable TOC content and thermal maturity: Examples from the Lublin and Baltic Basins, Poland and Lithuania," *International Journal of Coal Geology*, vol. 180, pp. 100–112, 2017.

[4] P. J. M. Monteiro, C. H. Rycroft, and G. I. Barenblatt, "A mathematical model of fluid and gas flow in nanoporous media," *Proceedings of the National Academy of Sciences*, vol. 109, no. 50, pp. 20309–20313, 2012.

[5] C. McGlade, J. Speirs, and S. Sorrell, "Unconventional gas - A review of regional and global resource estimates," *Energy*, vol. 55, pp. 571–584, 2013.

[6] J. Wang, Q. Kang, Y. Wang, R. Pawar, and S. S. Rahman, "Simulation of gas flow in micro-porous media with the regularized lattice Boltzmann method," *Fuel*, vol. 205, pp. 232–246, 2017.

[7] P. Aldhous, "Drilling into the unknown," *New Scientist*, vol. 213, no. 2849, pp. 8–10, 2012.

[8] F. Birol, C. Besson, T. Gould, M. Baroni, L. Cozzi, I. Cronshaw, C. Festa, M. Frank, A. Bromhead, D. Elis, T. Topalgoekceli, and A. Yanagisawa, "Golden rules for a golden age of gas. World Energy Outlook Special Report on Unconventional Gas," 2012.

[9] T. W. Patzek, F. Male, and M. Marder, "From the Cover: Cozzarelli Prize Winner: Gas production in the Barnett Shale obeys a simple scaling theory," *Proceedings of the National Academy of Sciences*, vol. 110, no. 49, pp. 19731–19736, 2013.

[10] A. S. Ziarani and R. Aguilera, "Knudsen's Permeability Correction for Tight Porous Media," *Transport in Porous Media*, vol. 91, no. 1, pp. 239–260, 2012.

[11] H. Yu, J. C. Fan, J. Chen, Y. B. Zhu, and H. A. Wu, "Pressure-dependent transport characteristic of methane gas in slit nanopores," *International Journal of Heat and Mass Transfer*, vol. 123, pp. 657–667, 2018.

[12] H. Yu, J. Chen, Y. B. Zhu, F. C. Wang, and H. A. Wu, "Multiscale transport mechanism of shale gas in micro/nano-pores," *International Journal of Heat and Mass Transfer*, vol. 111, pp. 1172–1180, 2017.

[13] T. Wu, X. Li, J. Zhao, and D. Zhang, "Multiscale pore structure and its effect on gas transport in organic-rich shale," *Water Resources Research*, vol. 53, no. 7, pp. 5438–5450, 2017.

[14] J. K. Holt, "Fast Mass Transport Through Sub-2-Nanometer Carbon Nanotubes," *Science*, vol. 312, no. 5776, pp. 1034–1037, 2006.

[15] M. Gad-el Hak, "The Fluid Mechanics of Microdevices—The Freeman Scholar Lecture," *Journal of Fluids Engineering*, vol. 121, no. 1, p. 5, 1999.

[16] H. Struchtrup, *Macroscopic Transport Equations for Rarefied Gas Flows*. Interaction of Mechanics and Mathematics, Berlin, Heidelberg: Springer Berlin Heidelberg, 2005.

[17] G. A. Bird, *Molecular gas dynamics*. London: Oxford University Press, 1976.

[18] F. Civan, "Effective correlation of apparent gas permeability in tight porous media," *Transport in Porous Media*, vol. 82, no. 2, pp. 375–384, 2010.

[19] S. A. Schaaf and P. L. Chambre, "Flow of Rarefied Gases," in *Fundamentals of Gas Dynamics*, pp. 687–740, Princeton: Princeton University Press, 1961.

[20] G. H. Tang, W. Q. Tao, and Y. L. He, "Gas slippage effect on microscale porous flow using the lattice Boltzmann method," *Physical Review E*, vol. 72, no. 5, p. 056301, 2005.

[21] L. Wu, M. T. Ho, L. Germanou, X.-J. Gu, C. Liu, K. Xu, and Y. Zhang, "On the apparent permeability of porous media in rarefied gas flows," *Journal of Fluid Mechanics*, vol. 822, pp. 398–417, 2017.

[22] G. E. Karniadakis, A. Beskok, and N. Aluru, *Microflows and Nanoflows: Fundamentals and Simulation*. Springer, 2005.

[23] S. Roy, R. Raju, H. F. Chuang, B. A. Cruden, and M. Meyyappan, "Modeling gas flow through microchannels and nanopores," *Journal of Applied Physics*, vol. 93, no. 8, pp. 4870–4879, 2003.

[24] A. Beskok and G. E. Karniadakis, "Report: A model for flows in channels, pipes, and ducts at micro and nano scales," *Microscale Thermophysical Engineering*, vol. 3, no. 1, pp. 43–77, 1999.

[25] S. J. Kazmouz, A. Giusti, and E. Mastorakos, "Numerical simulation of shale gas flow in three-dimensional fractured porous media," *Journal of Unconventional Oil and Gas Resources*, vol. 16, pp. 90–112, 2016.

[26] X. Wang and J. Sheng, "Gas sorption and non-Darcy flow in shale reservoirs," *Petroleum Science*, vol. 14, no. 4, pp. 746–754, 2017.

[27] H. Yu, Y. Zhu, X. Jin, H. Liu, and H. Wu, "Multiscale simulations of shale gas transport in micro/nano-porous shale matrix considering pore structure influence," *Journal of Natural Gas Science and Engineering*, vol. 64, pp. 28–40, 2019.

[28] H. Darabi, A. Ettehad, F. Javadpour, and K. Sepehrnoori, "Gas flow in ultra-tight shale strata," *Journal of Fluid Mechanics*, vol. 710, pp. 641–658, 2012.

[29] F. Javadpour, "Nanopores and Apparent Permeability of Gas Flow in Mudrocks (Shales and Siltstone)," *Journal of Canadian Petroleum Technology*, vol. 48, no. 08, pp. 16–21, 2009.

[30] D. M. Ruthven, *Principles of Adsorption and Adsorption Processes*. John Wiley & Sons, 1984.

[31] H. Singh, F. Javadpour, A. Ettehadtavakkol, and H. Darabi, "Nonempirical Apparent Permeability of Shale," *SPE Reservoir Evaluation & Engineering*, vol. 17, no. 03, pp. 414–424, 2014.

[32] J. Ma, J. P. Sanchez, K. Wu, G. D. Couples, and Z. Jiang, "A pore network model for simulating non-ideal gas flow in micro- and nano-porous materials," *Fuel*, vol. 116, pp. 498–508, 2014.

[33] L. Ma, K. G. Taylor, P. D. Lee, K. J. Dobson, P. J. Dowey, and L. Courtois, "Novel 3D centimetre-to nano-scale quantification of an organic-rich mudstone: The Carboniferous Bowland Shale, Northern England," *Marine and Petroleum Geology*, vol. 72, pp. 193–205, 2016.

[34] L. J. Klinkenberg, "The Permeability Of Porous Media To Liquids And Gases," *American Petroleum Institute*, pp. 200–213, 1941.

[35] A. Ghassemi and A. Pak, "Pore scale study of permeability and tortuosity for flow through particulate media using Lattice Boltzmann method," *International Journal for Numerical and Analytical Methods in Geomechanics*, vol. 35, no. 8, pp. 886–901, 2011.

[36] J. C. Maxwell, "On Stresses in Rarified Gases Arising from Inequalities of Temperature," *Philosophical Transactions of the Royal Society of London*, vol. 170, no. 0, pp. 231–256, 1879.

[37] L. Chen, W. Fang, Q. Kang, J. De'Haven Hyman, H. S. Viswanathan, and W.-Q. Tao, "Generalized lattice Boltzmann model for flow through tight porous media with Klinkenberg's effect," *Physical Review E*, vol. 91, no. 3, p. 033004, 2015.

[38] F. A. Florence, J. Rushing, K. E. Newsham, and T. A. Blasingame, "Improved Permeability Prediction Relations for Low Permeability Sands," in *Rocky Mountain Oil & Gas Technology Symposium*, 2007.

[39] D. Lin, J. Wang, B. Yuan, and Y. Shen, "Review on gas flow and recovery in unconventional porous rocks," *Advances in Geo-Energy Research*, vol. 1, no. 1, pp. 39–53, 2017.

[40] D. Lasseux, F. J. Valdés Parada, and M. L. Porter, "An improved macroscale model for gas slip flow in porous media," *Journal of Fluid Mechanics*, vol. 805, pp. 118–146, 2016.

[41] N. T. Le, C. J. Greenshields, and J. M. Reese, "Evaluation of nonequilibrium boundary conditions for hypersonic rarefied gas flows," in *Progress in Flight Physics*, (Les Ulis, France), pp. 217–230, EDP Sciences, 2012.

[42] R. A. Millikan, "Coefficients of slip in gases and the law of reflection of molecules from the surfaces of solids and liquids," *Physical Review*, 1923.

[43] T. Ewart, P. Perrier, I. Graur, and J. G. Méolans, "Mass flow rate measurements in a microchannel, from hydrodynamic to near free molecular regimes," *Journal of Fluid Mechanics*, vol. 584, pp. 337–356, 2007.

[44] T. Ewart, P. Perrier, I. Graur, and J. G. Méolans, "Tangential momemtum accommodation in microtube," *Microfluidics and Nanofluidics*, vol. 3, no. 6, pp. 689–695, 2007.

[45] H. Yamaguchi, Y. Matsuda, and T. Niimi, "Molecular-dynamics study on characteristics of energy and tangential momentum accommodation coefficients," *Physical Review E*, vol. 96, no. 1, p. 013116, 2017.

[46] L. Zhang, D. Li, D. Lu, and T. Zhang, "A new formulation of apparent permeability for gas transport in shale," *Journal of Natural Gas Science and Engineering*, vol. 23, pp. 221–226, 2015.

[47] X. Cui, A. M. Bustin, and R. M. Bustin, "Measurements of gas permeability and diffusivity of tight reservoir rocks: different approaches and their applications," *Geofluids*, vol. 9, no. 3, pp. 208–223, 2009.

[48] J. Ren, P. Guo, S. Peng, and C. Yang, "Investigation on permeability of shale matrix using the lattice Boltzmann method," *Journal of Natural Gas Science and Engineering*, vol. 29, pp. 169–175, 2016.

[49] R. Nazari Moghaddam and M. Jamiolahmady, "Slip flow in porous media," *Fuel*, vol. 173, pp. 298–310, 2016.

[50] L. Chen, Q. Kang, Z. Dai, H. S. Viswanathan, and W. Tao, "Permeability prediction of shale matrix reconstructed using the elementary building block model," *Fuel*, vol. 160, pp. 346–356, 2015.

[51] P. Carman, "Fluid flow through granular beds," *Transactions of the Institution of Chemical Engineers*, vol. 15, pp. 155–166, 1937.

[52] J. Kozeny, "Über kapillare Leitung des Wassers im Boden [Concerning the capillary transport of water in soil]," *Sitzungsberichte der Akademie der Wissenschaften in Wien*, 1927.

[53] J. G. Heid, J. J. McMahon, R. F. Nielsen, and S. T. Yuster, "Study of the permeability of rocks to homogeneous fluids," *Drilling and Production Practice 1950*, 1950.

[54] A. Dehghan Khalili, J.-Y. Arns, F. Hussain, Y. Cinar, W. Pinczewski, and C. H. Arns, "Permeability Upscaling for Carbonates From the Pore Scale by Use of Multiscale X-Ray-CT Images," *SPE Reservoir Evaluation & Engineering*, vol. 16, no. 04, pp. 353–368, 2013.

[55] J. Zhao, J. Yao, M. Zhang, L. Zhang, Y. Yang, H. Sun, S. An, and A. Li, "Study of Gas Flow Characteristics in Tight Porous Media with a Microscale Lattice Boltzmann Model," *Scientific Reports*, vol. 6, no. 1, p. 32393, 2016.

[56] M. T. Ho, L. Zhu, L. Wu, P. Wang, Z. Guo, J. Ma, and Y. Zhang, "Pore-scale simulations of rarefied gas flows in ultra-tight porous media," *Fuel*, vol. 249, pp. 341–351, 2019.

[57] B. Bai, M. Elgmati, H. Zhang, and M. Wei, "Rock characterization of Fayetteville shale gas plays," *Fuel*, vol. 105, pp. 645–652, 2013.

[58] C. Soulaine, F. Gjetvaj, C. Garing, S. Roman, A. Russian, P. Gouze, and H. A. Tchelepi, "The Impact of Sub-Resolution Porosity of X-ray Microtomography Images on the Permeability," *Transport in Porous Media*, vol. 113, no. 1, pp. 227–243, 2016.

[59] Q. Xiong, T. G. Baychev, and A. P. Jivkov, "Review of pore network modelling of porous media: Experimental characterisations, network constructions and applications to reactive transport," *Journal of Contaminant Hydrology*, vol. 192, pp. 101–117, 2016.

[60] H. C. Brinkman, "A calculation of the viscous force exerted by a flowing fluid on a dense swarm of particles," *Flow, Turbulence and Combustion*, vol. 1, no. 1, p. 27, 1949.

[61] M. Karimi-Fard, L. Durlofsky, and K. Aziz, "An Efficient Discrete-Fracture Model Applicable for General-Purpose Reservoir Simulators," *SPE Journal*, vol. 9, no. 02, pp. 227–236, 2004.

[62] M. Karimi-Fard and A. Firoozabadi, "Numerical Simulation of Water Injection in Fractured Media Using the Discrete-Fracture Model and the Galerkin Method," *SPE Reservoir Evaluation & Engineering*, vol. 6, no. 02, pp. 117–126, 2003.

[63] M. Karimi-Fard, B. Gong, and L. J. Durlofsky, "Generation of coarse-scale continuum flow models from detailed fracture characterizations," *Water Resources Research*, vol. 42, no. 10, 2006.

[64] J. Rouquerol, D. Avnir, C. W. Fairbridge, D. H. Everett, J. M. Haynes, N. Pernicone, J. D. F. Ramsay, K. S. W. Sing, and K. K. Unger, "Recommendations for the characterization of porous solids (Technical Report)," *Pure and Applied Chemistry*, vol. 66, no. 8, pp. 1739–1758, 1994.

[65] M. H. Anders, S. E. Laubach, and C. H. Scholz, "Microfractures: A review," *Journal of Structural Geology*, vol. 69, no. PB, pp. 377–394, 2014.

[66] J. F. Gale, S. E. Laubach, J. E. Olson, P. Eichhuble, and A. Fall, "Natural Fractures in shale: A review and new observations," *AAPG Bulletin*, vol. 98, no. 11, pp. 2165–2216, 2014.

[67] C. Soulaine and H. A. Tchelepi, "Micro-continuum Approach for Pore-Scale Simulation of Subsurface Processes," *Transport in Porous Media*, vol. 113, no. 3, pp. 431–456, 2016.

[68] L. M. Keller and L. Holzer, "Image-Based Upscaling of Permeability in Opalinus Clay," *Journal of Geophysical Research: Solid Earth*, vol. 123, no. 1, pp. 285–295, 2018.

[69] M. Krotkiewski, I. S. Ligaarden, K.-A. Lie, and D. W. Schmid, "On the Importance of the Stokes-Brinkman Equations for Computing Effective Permeability in Karst Reservoirs," *Communications in Computational Physics*, vol. 10, no. 5, pp. 1315–1332, 2011.

[70] P. Popov, G. Qin, L. Bi, Y. Efendiev, R. E. Ewing, and J. Li, "Multiphysics and Multiscale Methods for Modeling Fluid Flow Through Naturally Fractured Carbonate Karst Reservoirs," *SPE Reservoir Evaluation & Engineering*, vol. 12, no. 02, pp. 218–231, 2009.

[71] L. Chen, L. Zhang, Q. Kang, H. S. Viswanathan, J. Yao, and W. Tao, "Nanoscale simulation of shale transport properties using the lattice Boltzmann method: permeability and diffusivity," *Scientific Reports*, vol. 5, no. 1, p. 8089, 2015.

[72] P. Nithiarasu, K. Seetharamu, and T. Sundararajan, "Natural convective heat transfer in a fluid saturated variable porosity medium," *International Journal of Heat and Mass Transfer*, vol. 40, no. 16, pp. 3955–3967, 1997.

[73] P. Forchheimer, "Wasserbewegung durch Boden (Water movement through soil)," *Zeitschrift des Vereines Deutscher Ingenieure*, 1901.

[74] L. Jasinski and M. Dabrowski, "The Effective Transmissivity of a Plane-Walled Fracture With Circular Cylindrical Obstacles," *Journal of Geophysical Research: Solid Earth*, vol. 123, no. 1, pp. 242–263, 2018.

[75] G. S. Beavers and D. D. Joseph, "Boundary conditions at a naturally permeable wall," *Journal of Fluid Mechanics*, vol. 30, no. 1, p. 197, 1967.

[76] B. Goyeau, D. Lhuillier, D. Gobin, and M. Velarde, "Momentum transport at a fluid–porous interface," *International Journal of Heat and Mass Transfer*, vol. 46, no. 21, pp. 4071–4081, 2003.

[77] J. L. Auriault, "On the domain of validity of Brinkman's equation," *Transport in Porous Media*, vol. 79, no. 2, pp. 215–223, 2009.

[78] D. A. Nield and A. Bejan, *Convection in Porous Media*. New York, NY: Springer New York, 2013.

[79] N. Martys, D. P. Bentz, and E. J. Garboczi, "Computer simulation study of the effective viscosity in Brinkman's equation," *Physics of Fluids*, vol. 6, no. 4, pp. 1434–1439, 1994.

[80] J. A. Ochoa-Tapia and S. Whitaker, "Momentum transfer at the boundary between a porous medium and a homogenous fluid-I. Theoretical development," *International Journal Mass Transfer*, vol. 38, no. 14, pp. 2635–2646, 1995.

[81] F. J. Valdes-Parada, J. Alberto Ochoa-Tapia, and J. Alvarez-Ramirez, "On the effective viscosity for the Darcy-Brinkman equation," *Physica A*, vol. 385, no. 1, pp. 69–79, 2007.

[82] M. Sahraoui and M. Kaviany, "Slip and no-slip velocity boundary conditions at interface of porous, plain media," *International Journal of Heat and Mass Transfer*, vol. 35, no. 4, pp. 927–943, 1992.

[83] M. T. Ho, L. Zhu, L. Wu, P. Wang, Z. Guo, Z.-H. Li, and Y. Zhang, "A multi-level parallel solver for rarefied gas flows in porous media," *Computer Physics Communications*, vol. 234, pp. 14–25, 2019.

[84] W. Su, S. Lindsay, H. Liu, and L. Wu, "Comparative study of the discrete velocity and lattice Boltzmann methods for rarefied gas flows through irregular channels," *Physical Review E*, vol. 96, no. 2, p. 023309, 2017.

[85] P. Wang, M. T. Ho, L. Wu, Z. Guo, and Y. Zhang, "A comparative study of discrete velocity methods for low-speed rarefied gas flows," *Computers and Fluids*, vol. 161, pp. 33–46, 2018.

[86] L. Germanou, M. T. Ho, Y. Zhang, and L. Wu, "Intrinsic and apparent gas permeability of heterogeneous and anisotropic ultra-tight porous media," *Journal of Natural Gas Science and Engineering*, vol. 60, pp. 271–283, 2018.

[87] M. Wang, J. Wang, N. Pan, and S. Chen, "Mesoscopic predictions of the effective thermal conductivity for microscale random porous media," *Physical Review E*, vol. 75, no. 3, pp. 1–10, 2007.

[88] Z. Wang, X. Jin, X. Wang, L. Sun, and M. Wang, "Pore-scale geometry effects on gas permeability in shale," *Journal of Natural Gas Science and Engineering*, vol. 34, pp. 948–957, 2016.

[89] "MATLAB webpage." www.mathworks.com.

[90] R. M. Haralick and L. G. Shapiro, *Computer and Robot Vision.* Boston: Addison-Wesley Longman Publishing Co., Inc., 1st ed., 1992.

[91] "OpenFOAM webpage." www.openfoam.com.

[92] S. V. Patankar, *Numerical heat transfer and fluid flow.* Washington: Taylor & Francis, 1980.

[93] N. T. Le, C. White, J. M. Reese, and R. S. Myong, "Langmuir–Maxwell and Langmuir–Smoluchowski boundary conditions for thermal gas flow simulations in hypersonic aerodynamics," *International Journal of Heat and Mass Transfer*, vol. 55, no. 19-20, pp. 5032–5043, 2012.

[94] K. Aoki, Y. Sone, and T. Yamada, "Numerical analysis of gas flows condensing on its plane condensed phase on the basis of kinetic theory," *Physics of Fluids*, vol. 2, no. 10, pp. 1867–1878, 1990.

[95] J. E. Broadwell, "Study of rarefied shear flow by the discrete velocity method," *Journal of Fluid Mechanics*, vol. 19, no. 3, pp. 401–414, 1964.

[96] C. K. Chu, "Kinetic-Theoretic Description of the Formation of a Shock Wave," *Physics of Fluids*, vol. 8, no. 1, p. 12, 1965.

[97] J. Yang and J. Huang, "Rarefied Flow Computations Using Nonlinear Model Boltzmann Equations," *Journal of Computational Physics*, vol. 120, no. 2, pp. 323–339, 1995.

[98] L. Wu, C. White, T. J. Scanlon, J. M. Reese, and Y. Zhang, "Deterministic numerical solutions of the Boltzmann equation using the fast spectral method," *Journal of Computational Physics*, vol. 250, pp. 27–52, 2013.

[99] C. Christou, S. K. Dadzie, N. Thomas, R. Marschall, P. Hartogh, L. Jorda, E. Kührt, I. Wright, and R. Rodrigo, "Gas flow in near surface comet like porous structures: Application to 67P/Churyumov-Gerasimenko," *Planetary and Space Science*, vol. 161, pp. 57–67, 2018.

[100] C. White, T. J. Scanlon, and R. E. Brown, "Permeability of Ablative Materials Under Rarefied Gas Conditions," *Journal of Spacecraft and Rockets*, vol. 53, no. 1, pp. 134–142, 2016.

[101] P. L. Bhatnagar, E. P. Gross, and M. Krook, "A model for collision processes in gases. I. Small amplitude processes in charged and neutral one-component systems," *Physical Review*, vol. 94, no. 3, pp. 511–525, 1954.

[102] L. H. Holway, "New Statistical Models for Kinetic Theory: Methods of Construction," *Physics of Fluids*, vol. 9, no. 9, p. 1658, 1966.

[103] E. M. Shakhov, "Generalization of the Krook kinetic relaxation equation," *Fluid Dynamics*, vol. 3, no. 5, pp. 95–96, 1972.

[104] Y. H. Qian, D. D'Humières, and P. Lallemand, "Lattice BGK Models for Navier-Stokes Equation," *Europhysics Letters (EPL)*, vol. 17, no. 6, pp. 479–484, 1992.

[105] J. Wang, L. Chen, Q. Kang, and S. S. Rahman, "The lattice Boltzmann method for isothermal micro-gaseous flow and its application in shale gas flow: A review," *International Journal of Heat and Mass Transfer*, vol. 95, pp. 94–108, 2016.

[106] S. H. Kim, H. Pitsch, and I. D. Boyd, "Accuracy of higher-order lattice Boltzmann methods for microscale flows with finite Knudsen numbers," *Journal of Computational Physics*, vol. 227, no. 19, pp. 8655–8671, 2008.

[107] J. Meng and Y. Zhang, "Accuracy analysis of high-order lattice Boltzmann models for rarefied gas flows," *Journal of Computational Physics*, vol. 230, no. 3, pp. 835–849, 2011.

[108] J. Meng and Y. Zhang, "Gauss-Hermite quadratures and accuracy of lattice Boltzmann models for nonequilibrium gas flows," *Physical Review E*, vol. 83, no. 3, p. 036704, 2011.

[109] J. Meng, Y. Zhang, N. G. Hadjiconstantinou, G. A. Radtke, and X. Shan, "Lattice ellipsoidal statistical BGK model for thermal non-equilibrium flows," *Journal of Fluid Mechanics*, vol. 718, pp. 347–370, 2013.

[110] I. Graur and F. Sharipov, "Gas flow through an elliptical tube over the whole range of the gas rarefaction," *European Journal of Mechanics, B/Fluids*, 2008.

[111] F. Sharipov and G. Bertoldo, "Rarefied gas flow through a long tube of variable radius," *Journal of Vacuum Science & Technology A*, vol. 23, no. 3, pp. 531–533, 2005.

[112] F. Sharipov and I. A. Graur, "Rarefied gas flow through a zigzag channel," *Vacuum*, vol. 86, no. 11, pp. 1778–1782, 2012.

[113] S. Varoutis, S. Naris, V. Hauer, C. Day, and D. Valougeorgis, "Computational and experimental study of gas flows through long channels of various cross sections in the whole range of the Knudsen number," *Journal of Vacuum Science & Technology A*, vol. 27, no. 1, pp. 89–100, 2009.

[114] C. Baranger, J. Claudel, N. Hérouard, and L. Mieussens, "Locally refined discrete velocity grids for stationary rarefied flow simulations," *Journal of Computational Physics*, vol. 257, pp. 572–593, 2014.

[115] R. Guibert, M. Nazarova, P. Horgue, G. Hamon, P. Creux, and G. Debenest, "Computational Permeability Determination from Pore-Scale Imaging: Sample Size, Mesh and Method Sensitivities," *Transport in Porous Media*, vol. 107, no. 3, pp. 641–656, 2015.

[116] P. Renard, A. Genty, and F. Stauffer, "Laboratory determination of the full permeability tensor," *Journal of Geophysical Research: Solid Earth*, vol. 106, no. B11, pp. 26443–26452, 2001.

[117] R. Guibert, P. Horgue, G. Debenest, and M. Quintard, "A Comparison of Various Methods for the Numerical Evaluation of Porous Media Permeability Tensors from Pore-Scale Geometry," *Mathematical Geosciences*, vol. 48, no. 3, pp. 329–347, 2016.

[118] D. A. Lockerby, J. M. Reese, D. R. Emerson, and R. W. Barber, "Velocity boundary condition at solid walls in rarefied gas calculations," *Physical Review E*, vol. 70, no. 1, p. 017303, 2004.

[119] N. G. Hadjiconstantinou, "Comment on Cercignani's second-order slip coefficient," *Physics of Fluids*, vol. 15, no. 8, pp. 2352–2354, 2003.

[120] L. Gibelli, "A second-order slip model for arbitrary accomodation at the wall," in *3rd Micro and Nano Flows Conference*, (Thessaloniki, Greece, 22-24 August 2011), Brunel University, 2011.

[121] S. K. Loyalka, N. Petrellis, and T. S. Storvick, "Some numerical results for the BGK model: Thermal creep and viscous slip problems with arbitrary accomodation at the surface," *Physics of Fluids*, vol. 18, no. 9, p. 1094, 1975.

[122] A. Duda, Z. Koza, and M. Matyka, "Hydraulic tortuosity in arbitrary porous media flow," *Physical Review E*, vol. 84, no. 3, p. 036319, 2011.

[123] M. Matyka, A. Khalili, and Z. Koza, "Tortuosity-porosity relation in porous media flow," *Physical Review E*, vol. 78, no. 2, p. 026306, 2008.

[124] C. Jin, P. A. Langston, G. E. Pavlovskaya, M. R. Hall, and S. P. Rigby, "Statistics of highly heterogeneous flow fields confined to three-dimensional random porous media," *Physical Review E*, vol. 93, no. 1, 2016.

[125] B. Ghanbarian and F. Javadpour, "Upscaling pore pressure-dependent gas permeability in shales," *Journal of Geophysical Research: Solid Earth*, vol. 122, no. 4, pp. 2541–2552, 2017.

[126] Z. Chai, J. Lu, B. Shi, and Z. Guo, "Gas slippage effect on the permeability of circular cylinders in a square array," *International Journal of Heat and Mass Transfer*, vol. 54, no. 13-14, pp. 3009–3014, 2011.

[127] A. Borner, F. Panerai, and N. N. Mansour, "High temperature permeability of fibrous materials using direct simulation Monte Carlo," *International Journal of Heat and Mass Transfer*, vol. 106, pp. 1318–1326, 2017.

[128] L. Wu, J. M. Reese, and Y. Zhang, "Solving the Boltzmann equation deterministically by the fast spectral method: application to gas microflows," *Journal of Fluid Mechanics*, vol. 746, pp. 53–84, 2014.

[129] C. Pan, L.-S. Luo, and C. T. Miller, "An evaluation of lattice Boltzmann schemes for porous medium flow simulation," *Computers & Fluids*, vol. 35, no. 8-9, pp. 898–909, 2006.

[130] S. Takata and H. Funagane, "Poiseuille and thermal transpiration flows of a highly rarefied gas: over-concentration in the velocity distribution function," *Journal of Fluid Mechanics*, vol. 669, pp. 242–259, 2011.

[131] A. Nabovati and A. Sousa, "Fluid flow simulation in random porous media at pore level using the Lattice Boltzmann Method," *Journal of Engineering Science and Technology*, vol. 2, no. 3, pp. 226–237, 2007.

[132] J. Comiti and M. Renaud, "A new model for determining mean structure parameters of fixed beds from pressure drop measurements: application to beds packed with parallelepipedal particles," *Chemical Engineering Science*, vol. 44, no. 7, pp. 1539–1545, 1989.

[133] S. Peng, J. Yang, X. Xiao, B. Loucks, S. C. Ruppel, and T. Zhang, "An Integrated Method for Upscaling Pore-Network Characterization and Permeability Estimation: Example from the Mississippian Barnett Shale," *Transport in Porous Media*, vol. 109, no. 2, pp. 359–376, 2015.

[134] M. O. Salazar and J. R. Villa Piamo, "Permeability Upscaling Techniques for Reservoir Simulation," in *Latin American & Caribbean Petroleum Engineering Conference*, pp. 1–2, Society of Petroleum Engineers, 2007.

[135] P. King, "The use of renormalization for calculating effective permeability," *Transport in Porous Media*, vol. 4, no. 1, pp. 37–58, 1989.

[136] P. Renard and G. de Marsily, "Calculating equivalent permeability: a review," *Advances in Water Resources*, vol. 20, no. 5-6, pp. 253–278, 1997.

[137] C. P. Green and L. Paterson, "Analytical three-dimensional renormalization for calculating effective permeabilities," *Transport in Porous Media*, vol. 68, no. 2, pp. 237–248, 2007.

[138] "Digital Rocks Portal webpage." www.digitalrocksportal.org.

[139] Z. Koza, M. Matyka, and A. Khalili, "Finite-size anisotropy in statistically uniform porous media," *Physical Review E*, vol. 79, no. 6, pp. 1–7, 2009.

[140] P. Horgue, R. Guibert, H. Gross, P. Creux, and G. Debenest, "Efficiency of a two-step upscaling method for permeability evaluation at Darcy and pore scales," *Computational Geosciences*, vol. 19, no. 6, pp. 1159–1169, 2015.

[141] M. Le Bars and M. G. Worster, "Interfacial conditions between a pure fluid and a porous medium: Implications for binary alloy solidification," *Journal of Fluid Mechanics*, vol. 550, pp. 149–173, 2006.

[142] A. Terzis, I. Zarikos, K. Weishaupt, G. Yang, X. Chu, R. Helmig, and B. Weigand, "Microscopic velocity field measurements inside a regular porous medium adjacent to a low Reynolds number channel flow," *Physics of Fluids*, vol. 31, no. 4, p. 042001, 2019.

[143] F. J. Valdés-Parada, C. G. Aguilar-Madera, J. A. Ochoa-Tapia, and B. Goyeau, "Velocity and stress jump conditions between a porous medium and a fluid," *Advances in Water Resources*, vol. 62, pp. 327–339, 2013.

[144] Q. Zhang and A. Prosperetti, "Pressure-driven flow in a two-dimensional channel with porous walls," *Journal of Fluid Mechanics*, vol. 631, pp. 1–21, 2009.

[145] M. Mokhtari and A. N. Tutuncu, "Characterization of anisotropy in the permeability of organic-rich shales," *Journal of Petroleum Science and Engineering*, vol. 133, pp. 496–506, 2015.

[146] L. Wang and X. Yin, "Apparent permeability of flow through periodic arrays of spheres with first-order slip," *Powder Technology*, vol. 311, pp. 313–327, 2017.

Appendix A

The *darcyFoam* solver utilised in this thesis is based on the existing `OpenFOAM` solver *laplacianFoam*. The two files of the solver are *darcyFoam.C* and *createFields.H* and their contents are given in the following Figs. A.1 and A.2.

```
#include "fvCFD.H"
#include "simpleControl.H"

// * * * * * * * * * * * * * * * * * * * * * * * * * * * * * * * * * * * * * * * * * * * * //

int main(int argc, char *argv[])
{
    #include "setRootCase.H"

    #include "createTime.H"
    #include "createMesh.H"

    simpleControl simple(mesh);

    #include "createFields.H"

    // * * * * * * * * * * * * * * * * * * * * * * * * * * * * * * * * * * * * * * * * * * * * //

    Info<< "\nCalculating pressure distribution\n" << endl;

    while (simple.loop())
    {
        Info<< "Time = " << runTime.timeName() << nl << endl;

        while (simple.correctNonOrthogonal())
        {
            solve
            (
                fvm::laplacian(k/mu, p)
            );
        }

    U = -1/mu*(k & fvc::grad(p));

    runTime.write();

        Info<< "ExecutionTime = " << runTime.elapsedCpuTime() << " s"
            << "  ClockTime = " << runTime.elapsedClockTime() << " s"
            << nl << endl;
    }

    Info<< "End\n" << endl;

    return 0;
}
```

Figure A.1: Contents of file *darcyFoam.C*

```
Info<< "Reading field p\n" << endl;

volScalarField p
(
    IOobject
    (
        "p",
        runTime.timeName(),
        mesh,
        IOobject::MUST_READ,
        IOobject::AUTO_WRITE
    ),
    mesh
);

volVectorField U
(
    IOobject
    (
        "U",-
        runTime.timeName(),
        mesh,
        IOobject::MUST_READ,
        IOobject::AUTO_WRITE
    ),
    mesh,
dimensionedVector("U",dimensionSet(0,1,-1,0,0,0,0),vector::zero)
);


Info<< "Reading field k\n" << endl;

volTensorField k
(
    IOobject
    (
        "k",
        runTime.timeName(),
        mesh,
        IOobject::MUST_READ,
        IOobject::AUTO_WRITE
    ),
mesh
);
 Info<< "Reading transportProperties\n" << endl;

 IOdictionary transportProperties
 (
     IOobject
     (
         "transportProperties",
         runTime.constant(),
         mesh,
         IOobject::MUST_READ_IF_MODIFIED,
         IOobject::NO_WRITE
     )
 );

 Info<< "Reading fluid viscosity mu\n" << endl;

 dimensionedScalar mu
 (
     transportProperties.lookup("mu")
 );
```

Figure A.2: Contents of file *createFields.H*